

**Effects of spatial confinement  
on conduction electrons  
in semiconductor nanostructures**

Druk: Ridderprint offsetdrukkerij, Ridderkerk

ISBN 90-393-3232-0

# **Effects of spatial confinement on conduction electrons in semiconductor nanostructures**

**Effecten van ruimtelijke opsluiting op geleidingselektronen in  
halfgeleider nanostructuren**

(met een samenvatting in het Nederlands)

## **PROEFSCHRIFT**

TER VERKRIJGING VAN DE GRAAD VAN DOCTOR  
AAN DE UNIVERSITEIT UTRECHT OP GEZAG VAN  
DE RECTOR MAGNIFICUS, PROF. DR. W. H. GISPEN,  
INGEVOLGE HET BESLUIT VAN HET COLLEGE VOOR  
PROMOTIES IN HET OPENBAAR TE VERDEDIGEN OP  
VRIJDAG 31 JANUARI 2003 DES MIDDAGS TE 12.45 UUR

DOOR

**Alexander Germeau**

GEBOREN OP 21 SEPTEMBER 1973 TE LEUVEN

PROMOTOREN:

Prof. dr. D. Vanmaekelbergh  
Faculteit Scheikunde  
Universiteit Utrecht

Prof. dr. W. F. van der Weg  
Faculteit Natuur- en Sterrenkunde  
Universiteit Utrecht

CO-PROMOTOR:

Dr. E. E. van Faassen  
Faculteit Natuur- en Sterrenkunde  
Universiteit Utrecht

# Contents

---

<b>1</b>	<b>Semiconductor nanostructures</b>	<b>7</b>
1.1	Scope and outline of this thesis . . . . .	7
1.2	Electrons in bulk semiconductor crystals . . . . .	9
1.3	Effects of spatial confinement in macroporous GaP . . . . .	11
1.4	Quantum size-confinement . . . . .	12
	<b>References</b>	<b>15</b>
<b>2</b>	<b>Dielectric measurements at microwave frequencies</b>	<b>17</b>
2.1	Abstract . . . . .	17
2.2	Introduction . . . . .	17
2.3	Experimental . . . . .	19
2.4	Waveguides . . . . .	21
2.5	Cavity Perturbation Model . . . . .	25
2.6	Transmission Line Model . . . . .	31
2.7	Conclusions . . . . .	35
	<b>References</b>	<b>37</b>
<b>3</b>	<b>Short range electron motion in semiconducting macroporous GaP</b>	<b>39</b>
3.1	Abstract . . . . .	39
3.2	Introduction . . . . .	39
3.3	Experimental . . . . .	44
3.4	Determination of the short range mobility . . . . .	46
3.5	Electron-hole recombination under constant illumination . . . . .	51
3.6	Electron-hole recombination time resolved . . . . .	55
3.7	Conclusions . . . . .	59
	<b>References</b>	<b>61</b>
<b>4</b>	<b>Optical transitions between the conduction levels of ZnO quantum dots studied by IR absorption spectroscopy</b>	<b>63</b>
4.1	Abstract . . . . .	63
4.2	Introduction . . . . .	63
4.3	Single-electron conduction levels in ZnO quantum dots . . . . .	65

4.4	Optical transitions between the conduction levels in ZnO quantum dots . . . . .	71
4.4.1	Electric dipole transitions in a one-electron dot and oscillator strengths . . . . .	71
4.4.2	Transitions in a dot containing more than one electron . . . . .	75
4.5	IR absorption spectra obtained with an assembly of ZnO quantum dots . . . . .	75
4.5.1	Experimental method . . . . .	75
4.5.2	Results . . . . .	78
4.6	Quantitative analysis of the spectra . . . . .	82
4.6.1	A statistical model . . . . .	82
4.6.2	Discussion of the results . . . . .	85
4.7	IR absorption spectroscopy of a colloidal solution of ZnO quantum dots . . . . .	94
4.7.1	Experimental . . . . .	94
4.7.2	Results and discussion . . . . .	94
4.8	Conclusions . . . . .	99
	<b>References</b>	<b>101</b>
	<b>Appendix A: Transmission Line Theory for currents and voltages</b>	<b>103</b>
	<b>Appendix B: Dielectric constant of a porous semiconductor</b>	<b>107</b>
	<b>Appendix C: Polarisation energy of a spherical symmetric charge distribution</b>	<b>113</b>
	<b>Samenvatting</b>	<b>115</b>
	<b>List of publications</b>	<b>121</b>
	<b>Dankwoord</b>	<b>123</b>
	<b>Curriculum vitae</b>	<b>125</b>

# 1 Semiconductor nanostructures

---

## 1.1 Scope and outline of this thesis

Semiconductor nanostructures have received much attention from chemists and physicists in the last decade due to the fact that their electrical and optical properties can be very different from those of bulk semiconductor crystals. The optical and electrical properties of semiconductor nanostructures can be tailored to a large extent by the dimensions of the crystals. The various effects that occur due to spatial confinement of electrons in such structures are of scientific importance. In addition, semiconductor nanostructures are very promising for a number of applications in the opto-electronic industry.

Semiconductor nanostructures will show size-dependent properties different from those of a macroscopic semiconductor if one or more dimensions of the structure is in the same range as the length scale of a physical quantity ( e.g. wavelength of light, wavelength of electrons, electrostatic length scales). For instance, porous semiconductors with random structures and pores will strongly scatter photons with a wavelength similar to the dimensions of the structures and pores. Macroporous n-type GaP is a random network with structures of dimensions in the 150-300 nm range. At present, macroporous GaP is the strongest known scattering medium for visible light [1], [2]. The electrical properties of such a semiconductor network can also be extraordinary. For instance, the electron depletion layer, with a width in the 10-50 nm range, can "permeate" the porous network giving rise to a *three-dimensional* interfacial region. As a result, the electrical or electrochemical capacitance of such a system can be many orders of magnitude larger than that of a flat interface [3], [4]. Furthermore, random semiconductor networks with dimensions in the 100 nm range show very efficient separation of photogenerated electrons and holes, due to the fact that the diffusion length of the minority carrier is close to the size of the structures in the network [5].

Long-range electron transport in random networks of semiconductors has been studied extensively. It was generally found that electron diffusion is extremely slow. For example, the effective "long-range" mobility of the conduction electrons in n-type macroporous GaP can be five orders of magnitude smaller than in a bulk GaP crystal [6]. This low mobility is due to multiple trapping/detrapping

of the conduction electrons in interfacial states. Although interfacial trap states can thus play an important role in the attenuation of long-range transport, it has proven very difficult, however, to quantify the contribution of surface trapping in long-range transport by independent methods. Therefore, it would be of interest to measure the trap-free conduction mobility  $\mu$  of electrons in a *porous semiconductor*.

The first part of this thesis (chapters 2 and 3) presents a study of the short-range mobility of conduction electrons in macroporous n-type GaP. The complex dielectric constant of macroporous GaP in the  $10^{10}$  Hz region is determined by measuring the reflection of microwaves on a cavity loaded with a porous sample. During one oscillation period of the electromagnetic wave the electrons, residing in the central part of the porous structure, travel over a distance of about one nanometer; the electronic transport involves only very small distances and is not affected by the geometrical topology of the sample. An analysis of the results provides the short-range trap-free mobility which differs significantly from the mobility of conduction electrons in a bulk crystal of GaP, and orders of magnitude from the long-range mobility determined by multiple trapping in macroporous GaP. In addition, time-resolved microwave reflection measurements in the ns- $\mu$ s region allow us to measure the extension/shrinking of the depletion barriers in the n-type GaP network due to photogeneration/recombination of conduction electrons. In such a way, we were able to study the kinetics of electron-hole surface recombination in macroporous n-type GaP. The method to determine the complex dielectric constant from microwave conductivity measurements is explained in chapter 2. The microwave experiments on macroporous GaP are presented in chapter 3.

Another interesting size-effect occurs when the dimensions of the semiconductor are further reduced to below ten nanometer, such that they are smaller than the wavelength of conduction electrons in bulk semiconductors. The electron standing waves have to "fit" the size of the semiconductor nanocrystal; this leads to discrete levels for conduction electrons and valence holes. These discrete energy levels and the HOMO-LUMO band gap will strongly depend on the dimensions of the crystal. For spherical nanocrystals, the electrons are expected to move in a spherically symmetric confinement potential, where the eigenstates can be classified as  $S, P, D, \dots$  orbitals according to the quantum number of angular momentum. As such, the usual selection rules for optical transitions in atomic spectroscopy should be observed. It is interesting, however, to consider whether this analogy of "artificial atoms" applies in practice, in particular whether the usual spectroscopic selection rules are violated by symmetry breaking interactions at the surface or with the underlying crystal lattice.



In the second part of this thesis (chapter 4), we present a study of the optical transitions in artificial atoms which consist of one to ten electrons strongly confined in colloidal ZnO nanocrystals with a diameter in the 3 - 6 nm range. We have prepared the artificial atoms by injection of electrons into the conduction levels of ZnO nanocrystals using an electrochemical and a photochemical method. With IR absorption spectroscopy, we have studied the optical transitions in these artificial atoms. We have found that the symmetry of the atomic-like orbitals determine if an electronic transition between two energy levels is allowed. The selection rules are the same as for electronic dipole transitions in ordinary atoms. From an analysis of the IR absorption spectra we obtained the energy separation between the single-particle conduction energy levels as a function of the diameter of the ZnO nanocrystals. These results present a remarkable demonstration of the size-confinement effect.

Below, we introduce some fundamental concepts which form the basis for an understanding of the research results of this thesis presented in chapters 2-4. We start with a description of electrons and holes in bulk semiconductor crystals. The electrical transport properties of semiconductor nanostructures in the size-range of 100 nm are considered next. Finally, a brief introduction to quantum size-confinement is presented.

## 1.2 Electrons in bulk semiconductor crystals

For a free electron, the Hamiltonian contains only the kinetic energy operator. The eigenvectors of this Hamiltonian are wavefunctions  $e^{i\mathbf{k}\cdot\mathbf{r}}$  which represent running waves. The electron in such an eigenstate carries a momentum  $\mathbf{p} = \hbar\mathbf{k}$  and has an energy [7]

$$E = \frac{\hbar^2}{2m}k^2, \quad (1.1)$$

where  $m$  denotes the mass of the electron. For an electron in a crystal we describe the interaction with core ions by a potential  $U(\mathbf{r})$ . Because of the periodicity of the lattice,  $U(\mathbf{r} + \mathbf{R}) = U(\mathbf{r})$  for every vector  $\mathbf{R}$  between two lattice points. An important theorem states that the solutions of the Schrodinger equation for the case involving a periodic potential must have the form

$$\psi_{\mathbf{k}}(\mathbf{r}) = u_{\mathbf{k}}(\mathbf{r})e^{i\mathbf{k}\cdot\mathbf{r}} \quad (1.2)$$

where  $u_{\mathbf{k}}(\mathbf{r})$  has the translation symmetry of the lattice. The valence and conduction electron energy levels in a crystal can often be described by a nearly-free

electron model for which the periodic potential of the ion cores is only a weak perturbation. Fig. 1.1 shows a plot of the energy versus wavevector for an electron in a monatomic linear lattice of lattice constant  $a$ . For a wavevector  $k = \pm\pi/a$ ,

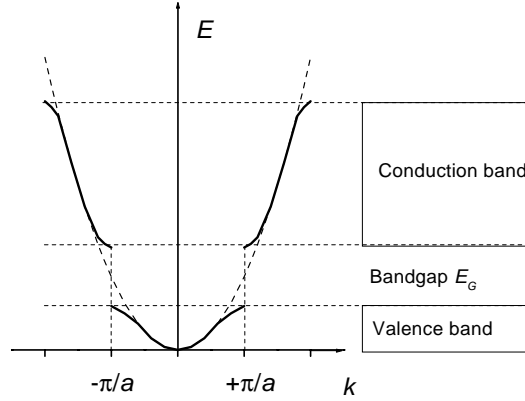


**Figure 1.1:** Schematic plot of the energy  $E$  versus the wavevector  $k$  for an electron in a linear lattice of lattice constant  $a$ . The energy gap  $E_g$  shown is associated with the first Bragg reflection at  $k = \pm\pi/a$ .

the curve splits up in two values by an amount  $E_g$ . The energy levels are arranged in energy bands separated by regions in energy for which no solutions of the Schrodinger equation exist. Such forbidden regions are called bandgaps. The physical reason for the bandgap is Bragg scattering at the ionic lattice for wavefunctions with a wavevector  $k = \pm n\pi/a$  where  $n$  is an integer number. From a linear combination of incoming waves and reflected waves, two standing waves can be constructed. One of this standing waves is more concentrated at the positions of the ionic cores and has a lower energy than the other standing wave, more concentrated between the ionic cores. The difference in energy between both states equals the bandgap  $E_g$ .

In a semiconductor crystal, the Fermi energy  $E_F$  lies in the bandgap. At low temperatures, the valence band is completely filled with electrons and the conduction band is completely empty. At higher temperatures, the lowest levels in the conduction band are filled by thermal activation leaving empty states at the top of the valence band. The electrical transport properties of a semiconductor are completely determined by the electrons at the bottom of the conduction band and the holes at the top of the valence band since only these charge carriers can make

transitions to empty states with a similar energy. At the bottom or top ( $k = k_m$ ) of a band we can make the approximation for small values of  $k$  that

$$E(k) \simeq E(k_m) + \left(\frac{\partial^2 E}{\partial k^2}\right)_{k=k_m} k^2. \quad (1.3)$$

This dispersion relation is identical to the dispersion relation for a free particle with mass  $m^* = \hbar^2 \left(\frac{\partial^2 E}{\partial k^2}\right)_{k=k_m}^{-1}$  (see Eq. 1.1). An electron (hole) with an energy at the bottom (top) of the conduction (valence) band behaves like a free electron with an effective mass  $m^*$ . If an electric field  $E$  is applied in a crystal, the force on the electron is equal to  $-eE$  and the average drift velocity will be [7]

$$v_{drift} = \frac{e\tau E}{m^*}, \quad (1.4)$$

where  $\tau$  is the mean free time between inelastic collisions at impurities, thermal vibrations of the lattice or dislocations. The atoms or dangling bonds at the surface of a crystal can have energy levels in the bandgap. Trapping of free carriers in energy levels at the surface can lead to a free carrier depletion layer, characterized by a potential barrier. Especially surface states with an energy close to the Fermi-level  $E_F$  can act as traps for charge carriers, reducing their mobility.

### 1.3 Effects of spatial confinement in macroporous GaP

In the first part of this thesis we consider a porous n-type GaP semiconductor with structure sizes of about 150 nm. The conduction electron energy levels are described by the bulk energy bands; quantum-size effects can be neglected. Due to a depletion barrier at the surface, the conduction electrons are confined to a volume with a size of about 80 nm. To describe the transport of electrons in this confined volume, we use a hydrodynamic model [8]. This model describes how, by applying a uniform electric field, the conduction electrons drift to the depletion barrier where they screen the applied electric field. Diffusion due to the charge density gradient at the surface acts as a force opposite to the applied field so that the screening charge is spread out over a distance of the order of the Debye screening length  $L$ . This is in firm contrast with the commonly used Mie theory [9] where diffusion is not taken into account and thus the screening charge is located singularly at the surface itself. With this accurate model for electrodynamics in confined geometries we interpret microwave conductivity measurements on porous GaP under constant illumination and laser pulse excitation.

## 1.4 Quantum size-confinement

Confinement of an electron in a crystalline material which is size-restricted in three dimensions demands that its wavefunction vanishes outside the crystallite. Due to this boundary condition the electron energy levels are discrete and the crystallite is called a quantum dot. As an example, for an electron confined in a cube with side  $L$ , the only wavefunctions  $e^{i\mathbf{k}\cdot\mathbf{r}}$  in agreement with the boundary condition are characterized by  $k_i = \frac{n_i\pi}{L}$  ( $i = x, y, z$ ) for  $n_i$  an integer number. These discrete wavevectors  $\mathbf{k}$  correspond to discrete energy levels

$$E = \frac{\hbar^2(k_x^2 + k_y^2 + k_z^2)}{2m}, \quad (1.5)$$

(see Fig. 1.2). For example, the separation between the lowest energy levels for

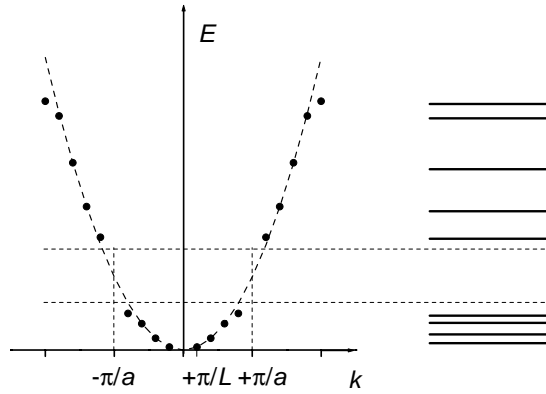


**Figure 1.2:** Schematic plot of the energy  $E$  versus the wavevector  $k$  for an electron in a semiconductor nanocrystal with diameter  $L$ .

a cube with a side  $L = 5$  nm is of the order of 400 meV.

Adding an electron to an otherwise neutral nanocrystal, its charge will interact with the (valence) electrons (electronic polarization) and the ionic lattice (ionic polarization) of the crystal. If the screening of the charge due to this polarization, occurs on a length scale larger than the size of the nanocrystal, the electron polarization energy will also depend on the size of the nanocrystal and the dielectric surroundings of the nanocrystal. Adding more electrons to a nanocrystal, Coulomb and exchange interactions between these electrons also need to be

accounted for. Although these interactions are screened by the dielectric environment, they become more important for smaller nanocrystals because of the increase in the spatial overlap of the wavefunctions due to quantum confinement. As an example, the Coulomb interaction between two S-electrons in a cube with a side  $L = 5$  nm and dielectric constant  $\epsilon = 10$  is of the order of 150 meV. Because all these interactions depend strongly on the size of the nanocrystal, in strongly confined systems as yet unobserved electrical and optical properties should emerge.



## References

---

- [1] F. Schuurmans, D. Vanmaekelbergh, J. Van de Lagemaat, A. Lagendijk, *Science* **284**, 141 (1999).
- [2] F. Schuurmans, M. Megens, D. Vanmaekelbergh, A. Lagendijk, *Phys. Rev. Lett.* **83**, 2183 (1999).
- [3] B. Erne, D. Vanmaekelbergh, J. Kelly, *Proc. Electrochem. Soc.* **95-8**, 34 (1995).
- [4] D. Vanmaekelbergh, A. Koster, F. Marin, *Adv. Mater.* **9**, 575 (1997).
- [5] B. Erne, D. Vanmaekelbergh, J. Kelly, *Adv. Mater.* **7**, 739 (1995).
- [6] A. Roest, P. de Jongh, D. Vanmaekelbergh, *Phys. Rev. B* **62**, 16926 (2000).
- [7] C. Kittel, *Introduction to Solid State Physics*, John Wiley, 1986.
- [8] E. van Faassen, *Phys. Rev. B* **58**, 23 (1998).
- [9] M. Born and E. Wolf, *Principles of Optics*, Pergamon Press, 1975.





## 2 Dielectric measurements at microwave frequencies

---

### 2.1 Abstract

Dielectric measurements at microwave frequencies provide information on electric conduction and polarization mechanisms with a time resolution of nanoseconds. Here we discuss an experimental method for the contactless measurement of the complex dielectric constant of a nonconducting dielectric sample. The dielectric constant is obtained from the reflection spectrum of a resonant microwave cavity loaded with the sample. We describe the simple Cavity Perturbation Model to obtain the change in the complex dielectric constant of the sample from the shift in the resonance frequency and the increase in the width of the reflection spectrum. To measure very small changes in the imaginary part of the dielectric constant, we describe with the general Transmission Line Model how the magnitude of the reflection depends on the dielectric constant of the sample. We test the accuracy of our method on reference samples and discuss the sensitivity for small changes in  $\epsilon'$  and  $\epsilon''$ .

### 2.2 Introduction

The dielectric constant  $\epsilon$  of a material describes the polarization density  $P = (\epsilon - 1)E$ , due to the presence of an electric field  $E$ . In a complex representation of quantities (with a time dependence given by  $e^{-i\omega t}$  where  $\omega$  is the radial frequency), the dielectric constant can become a complex number. The real part of the dielectric constant  $\epsilon'$  is a measure of how much electric energy is stored in a dielectric, the imaginary part of the dielectric constant  $\epsilon''$ , also called the loss factor, is a measure of how dissipating a material is to an external electric field. (These properties are easily understood by considering a capacitor filled with a dielectric with a complex dielectric constant. The capacitance of this capacitor is proportional to the real part  $\epsilon'$ , the conductance of the capacitor is proportional to the imaginary part  $\epsilon''$ .)

Figure 2.1 schematically shows the frequency dependence of a few important dielectric mechanisms, and their typical frequencies [1], [2]. Orientation of molecules with a permanent dipole moment by an electric field typically occurs up

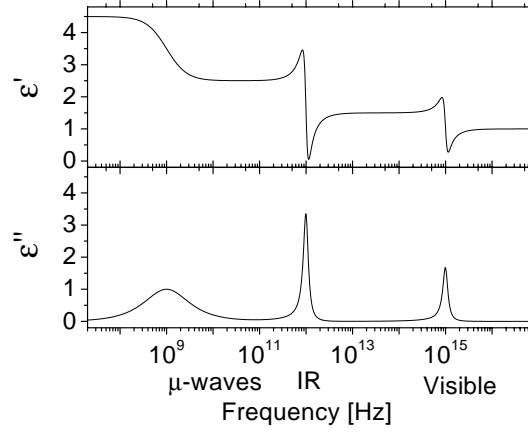


**Figure 2.1:** Schematic drawing of the frequency dependence of a few dielectric mechanisms: in order of increasing relaxation/resonance frequency we show dipole orientation and ionic and electronic polarization. As the frequency increases, the slower mechanisms drop out, leaving the faster ones to contribute to the storage ( $\epsilon'$ ). The loss factor ( $\epsilon''$ ) will correspondingly peak at each critical frequency.

to frequencies of about  $10^{10}$  Hz. At these frequencies, the real part of the dielectric constant  $\epsilon'$  falls off while the loss factor  $\epsilon''$  becomes maximal. Displacement of ions (atoms, molecules) by an electric field contributes to the real part of the dielectric constant  $\epsilon'$  up to IR frequencies (ionic polarization). Transitions between vibrational modes of ions give rise to strong absorption at IR frequencies. Electronic polarization in atoms contribute to the real part  $\epsilon'$  of the dielectric constant up to frequencies that correspond with visible light. At these frequencies, electronic transitions in atoms give rise to strong absorption.

Here we study dielectric measurements at microwave frequencies ( $10^9 - 10^{10}$  Hz corresponding to photon energies of  $10^{-5} - 10^{-4}$  eV). Microwave spectroscopy at these frequencies may reveal for example the energy levels of large rotating molecules (see Fig. 2.1) [3]-[5] or the fine structure in vibrational states of molecules [6]. Beside resonant absorption, dielectric measurements at microwave frequencies can be used to study polarization mechanisms with a resonance frequency larger than microwave frequencies (e.g. electronic polarization) or conductivity measurements, without a contribution from mechanisms slower than microwave frequencies. Moreover, all measurements can be obtained with a time resolution of nanoseconds. Time Resolved Microwave Conductivity (TRMC)

measurements, which need no electrical contacts to the sample, have been used to study photo-induced charge separation in thin semiconducting layers [7] and the decay of photo-electrons in a network of semiconducting nanocrystals [8]. A quantitative interpretation of TRMC results may provide information on the mobility of photo-electrons or photo-holes in large molecules [9]-[11] or on an isolated chain of polymers [12]. The growth mechanism of silicon films [13]-[15], their electrical transport mechanism [16], [17], and recombination of charge carriers at their interfaces [18], [19] have been studied by in-situ TRMC measurements. Transport mechanisms in superconductors have been studied by microwave conductivity measurements of their surface impedance [20]-[21].

We have built a microwave resonant cavity to measure small changes in the complex dielectric constant ( $\geq 10^{-6}$ ) of a small (milligrams) and low loss sample ( $\epsilon'' \leq 10$ ) with a time resolution of 10 ns. In section 2.4 we describe how electric currents and voltages at microwave frequencies, and their corresponding electromagnetic waves propagate through waveguides, that are structures designed to transport electromagnetic energy at high frequencies for example a coax-cable or a hollow metal beam. Next we describe the simple Cavity Perturbation Model to obtain the change in the complex dielectric constant of the sample from the shift in the resonance frequency and the increase in the width of the reflection spectrum. We test the accuracy of this method and discuss the sensitivity for small changes in  $\epsilon'$  and  $\epsilon''$ . The sensitivity in  $\epsilon''$  can become orders of magnitude better from a measurement of the height of the reflection. With the general Transmission Line Model we are able to describe the coupling of the waveguide to the cavity and obtain the reflected microwave power as a function of the dielectric constant of the sample in the cavity. We test the accuracy of this model on reference samples and discuss the sensitivity for changes in the complex dielectric constant.

## 2.3 Experimental

Fig. 2.2 shows a schematic drawing of our dielectric measurement set-up. Microwaves generated by a Gigatronic synthesizer (model 610, 30 mW output power with a frequency  $\nu$  between 6 and 12 GHz and a spectral resolution  $\delta\nu/\nu = 10^{-6}$ ) run through a rectangular X-band waveguide in  $TE_{1,0}$  mode to the cavity (see section 2.4). The cavity consists of an X-band waveguide ended at one side by a metal grid, which reflects all microwave power, and a metal pin at the other side, which partially reflects microwaves. By changing the position and height of the pin, the reflection at the cavity is tuned. Microwave power reflected at the cavity is amplified (Miteq Inc., AMF-2B-8612-30, +40dB) and detected in a microwave diode which delivers an output voltage as a function of the microwave power to a

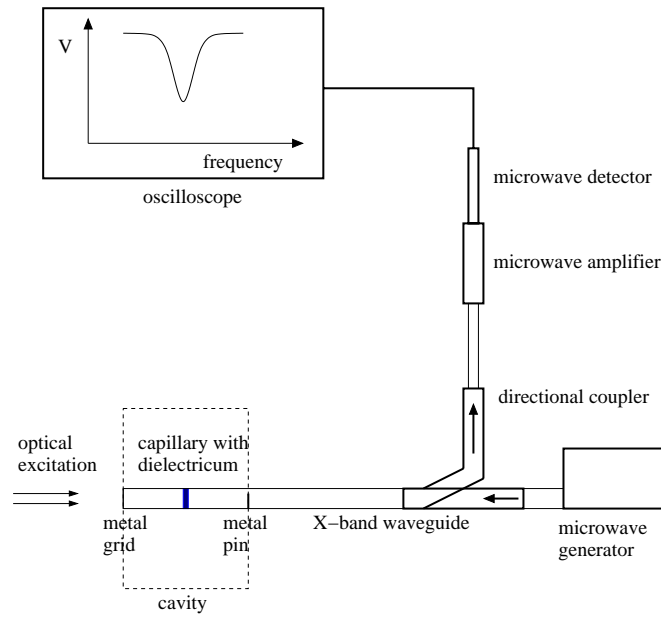


**Figure 2.2:** Schematic drawing of our dielectric measurement set-up. The directional coupler only transmits microwaves in the direction as indicated in the drawing.

digitizing oscilloscope (Lecroy 9450, 350 MHz bandwidth). Optical excitation of a dielectric sample in the cavity can be performed through the metal grid by a laser (pulsed YAG laser with pulse duration of a few nanoseconds and a pulse energy of 92mJ at a wavelength of 355nm) or by a halogen lamp. The time resolution of this set-up is restricted to 100 nanoseconds by the response time of the microwave cavity.

## 2.4 Waveguides

In our dielectric measurement set-up, we use a hollow metal waveguide (see Fig. 2.3) to couple the microwave generator to the resonant cavity and to transport the microwave power reflected at the cavity to the microwave detector. The resonant cavity itself is also built up from this waveguide. In this section we discuss how electromagnetic waves propagate in such a waveguide.

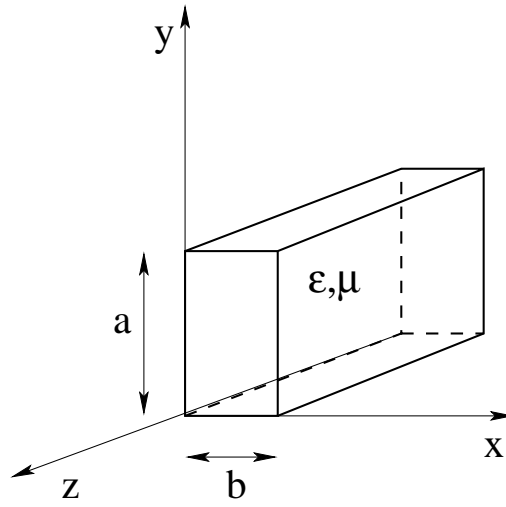


**Figure 2.3:** Schematic drawing of a hollow rectangular (X-band) waveguide.

For monochromatic waves, the electric ( $\mathbf{E}$ ) and magnetic ( $\mathbf{B}$ ) fields inside the waveguide are obtained from the Maxwell equations

$$\begin{aligned} \nabla \times \mathbf{E} &= -i\omega\mathbf{B} & \nabla \cdot \mathbf{B} &= 0 \\ \nabla \times \mathbf{B} &= i\mu\epsilon\omega\mathbf{E} & \nabla \cdot \mathbf{E} &= 0, \end{aligned} \quad (2.1)$$

and the boundary conditions at the walls. For the boundary conditions we assume that the walls consist of perfect conductors. Therefore the component of the electric field  $\mathbf{E}$  parallel to and the component of the magnetic induction  $\mathbf{B}$  perpendicular to the surface vanish at the surface. For a uniform permittivity  $\epsilon$  and permeability  $\mu$ , the electric and magnetic fields in the waveguide satisfy

$$(\nabla^2 + \mu\epsilon\omega^2) \begin{Bmatrix} \mathbf{E} \\ \mathbf{B} \end{Bmatrix} = 0 \quad (2.2)$$

and can be described as waves running in the positive and negative  $z$  directions:

$$\left. \begin{matrix} \mathbf{E}(x, y, z, t) \\ \mathbf{B}(x, y, z, t) \end{matrix} \right\} = \left\{ \begin{matrix} \mathbf{E}(x, y) \exp(\pm ik_z z + i\omega t) \\ \mathbf{B}(x, y) \exp(\pm ik_z z + i\omega t) \end{matrix} \right. . \quad (2.3)$$

Furthermore, the solutions of (2.2) can be divided into two categories: Transverse Magnetic (TM) waves are solutions with no magnetic component in the  $z$  direction i.e.  $B_z = 0$ , Transverse Electric (TE) waves have no electric component in the  $z$  direction i.e.  $E_z = 0$ .

For Transverse Electric waves, the  $z$ -component of the magnetic induction is given by

$$B_z(x, y) = B_o \cos\left(\frac{m\pi x}{a}\right) \cos\left(\frac{n\pi y}{b}\right). \quad (2.4)$$

From (2.2) it follows that

$$k_z^2 + \pi^2\left(\frac{m^2}{a^2} + \frac{n^2}{b^2}\right) = \mu\epsilon\omega^2. \quad (2.5)$$

For a non-absorbing medium inside the waveguide (i.e.  $\epsilon$  and  $\mu$  real) waves are not evanescent only if  $k_z$  is real. This occurs if the radial frequency  $\omega$  is larger than the cut-off frequency  $\omega_c$  given by

$$\omega_c = \frac{1}{\sqrt{\mu\epsilon}} \sqrt{\frac{m^2}{a^2} + \frac{n^2}{b^2}}. \quad (2.6)$$

The lowest cut-off frequency for Transverse Electric waves is obtained for the mode with  $m=1$  and  $n=0$  ( $TE_{1,0}$ ). For Transverse Magnetic Waves, the  $z$  component of the electric field is given by

$$E_z = E_o \sin\left(\frac{m\pi x}{a}\right) \sin\left(\frac{n\pi y}{b}\right) \quad (2.7)$$

and the lowest cut-off frequency is obtained for the mode with  $m=n=1$  ( $TM_{1,1}$ ).

In the X-band waveguide we use for our experiments,  $\epsilon = \mu = 1$ ,  $a = 2.286$  cm and  $b = 1.016$  cm. From (2.6), it follows that the cut-off frequency for the  $TE_{1,0}$  mode equals 6.6 GHz. The next mode has  $m=n=1$  and starts at 14.8 GHz. Fig. 2.4 shows the dispersion relation for electromagnetic waves in the two lowest modes ( $TE_{1,0}$  and  $TM_{1,1}$ ) in a X-band waveguide. Since the microwave generator used in our experiments has a frequency range from 6 to 12 GHz only the  $TE_{1,0}$  mode is excited and the electromagnetic fields in the waveguide are completely described by the complex amplitudes of the left and right running  $TE_{1,0}$  modes

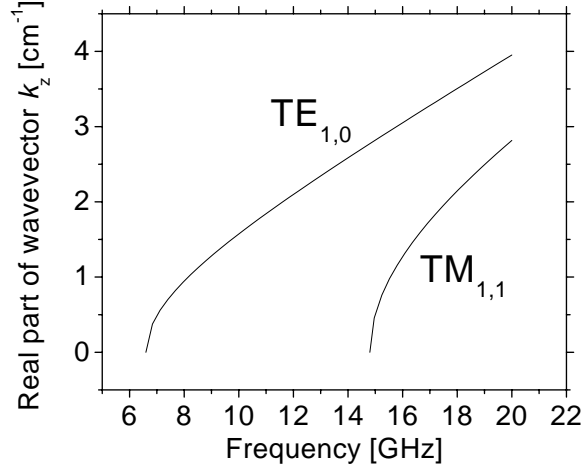


**Figure 2.4:** The dispersion relation for electromagnetic waves in the two lowest modes ( $TE_{1,0}$  and  $TM_{1,1}$ ), in the X-band waveguide (used in our experiments).

$E_o^{\rightarrow}$  and  $E_o^{\leftarrow}$ . The electromagnetic fields in the  $TE_{1,0}$  mode are explicitly given by  $E_x = E_z = H_y = 0$ ,

$$E_y = E_o^{\rightarrow} \sin\left(\frac{\pi x}{a}\right) \exp(\pm i k_z z - i \omega t) \quad (2.8)$$

$$H_z = \frac{\pi i}{\omega a \mu} E_o^{\rightarrow} \cos\left(\frac{\pi x}{a}\right) \exp(\pm i k_z z - i \omega t) \quad (2.9)$$

$$H_x = \pm \frac{1}{Z_o} E_o^{\rightarrow} \sin\left(\frac{\pi x}{a}\right) \exp(\pm i k_z z - i \omega t) \quad (2.10)$$

where  $B = \mu H$ . The characteristic impedance of the waveguide  $Z_o$ , defined by

$$\mathbf{H}_t = \pm \frac{1}{Z_o} \hat{\mathbf{z}} \times \mathbf{E}_t \exp(\pm i k_z z - i \omega t) \quad (2.11)$$

(where the subscript  $t$  denotes the component transverse to the direction of the waveguide), is given by  $Z_o = \frac{\omega \mu}{k_z} = \frac{k_z}{\epsilon \omega}$ .

Non-uniformities or obstacles in the waveguide e.g. a dielectric sample, possibly can excite higher modes of the electromagnetic fields but these modes vanish at a typical distance  $2\pi/k_z$  from the obstacle. Therefore at a certain distance from a small non-uniformity with a linear response, the amplitudes of the incoming and

outgoing waves at one side of an obstacle can be related to the amplitudes of the incoming and outgoing waves at the other side by a complex  $4 \times 4$  matrix.



## 2.5 Cavity Perturbation Model

Loading the cavity with a dielectric sample modifies the reflection at the cavity. We now discuss how to obtain the dielectric constant of the sample from the change in the reflection spectrum with the Cavity Perturbation Model (CPM) [22]. We test the accuracy of this model on reference samples and discuss the sensitivity for changes in  $\epsilon'$  and  $\epsilon''$  from the measurement of the resonance frequency  $\omega_0$  and the spectral width  $\Gamma$ .

In the Cavity Perturbation model one assumes that in the unperturbed cavity, i.e. the cavity without dielectric sample, the electric field is represented as  $\mathbf{E} = \mathbf{E}_0(\mathbf{r}) \exp(i\omega_0 t - \alpha t)$  and the magnetic field as  $\mathbf{H} = \mathbf{H}_0(\mathbf{r}) \exp(i\omega_0 t - \alpha t)$ . Remark that the cavity response equals  $(2\alpha)^{-1}$  where  $\alpha$  is the time constant at which the electric and magnetic field vanish. The spectrum of the electric energy stored in the cavity is proportional to the square modulus of the Fourier transform  $\tilde{\mathbf{E}}(\omega)$  of the electric field  $\mathbf{E}(t)$ . From

$$|\tilde{\mathbf{E}}(\omega)|^2 \approx \frac{1}{(\omega - \omega_0)^2 + \alpha^2}, \quad (2.12)$$

we obtain that  $\omega_0$  equals the resonance frequency (the frequency at which the spectrum is maximal) and that the full width of the spectrum at half maximum  $\Gamma$  equals  $2\alpha$ ; the spectral width of the cavity is inversely proportional to the cavity response time. By the introduction of a small dielectric sample with volume  $V_1$  and dielectric constant  $\epsilon$ , the electric field becomes

$$\mathbf{E} = (\mathbf{E}_0 + \mathbf{E}_1)(\mathbf{r}) \exp(i(\omega_0 + \delta\omega_0)t - (\alpha + \delta\alpha)t) \quad (2.13)$$

and

$$\mathbf{H} = (\mathbf{H}_0 + \mathbf{H}_1)(\mathbf{r}) \exp(i(\omega_0 + \delta\omega_0)t - (\alpha + \delta\alpha)t). \quad (2.14)$$

After some calculation, we obtain from the Maxwell relations (without any approximation)

$$\frac{\delta\omega_0 - i\delta\alpha}{\omega_0} = \frac{\int_{V_1} dV \mathbf{E}_1 \cdot \mathbf{D}_0 - \mathbf{E}_0 \cdot \mathbf{D}_1}{\int_{V_0} dV \mathbf{E}_0 \cdot (\mathbf{D}_0 + \mathbf{D}_1) - \mathbf{H}_0 \cdot (\mathbf{B}_0 + \mathbf{B}_1)}, \quad (2.15)$$

where  $V_0$  is the volume of the cavity. For  $|V_1\epsilon| \ll V_0$  we can make the approximation

$$\frac{\delta\omega_0 - i\delta\alpha}{\omega_0} \simeq \frac{\int_{V_1} dV \mathbf{E}_1 \cdot \mathbf{D}_0 - \mathbf{E}_0 \cdot \mathbf{D}_1}{\int_{V_0} dV \mathbf{E}_0 \cdot \mathbf{D}_0 - \mathbf{H}_0 \cdot \mathbf{B}_0}. \quad (2.16)$$

For a small dielectric post, parallel to the electric field we make the approximation  $E_1 \simeq 0$  to obtain

$$\frac{\delta\omega_o - i\delta\alpha}{\omega_o} \simeq \frac{\int_{V_1} dV (\epsilon_0 - \epsilon_1) \mathbf{E}_0^2}{\int_{V_0} dV \mathbf{E}_0 \cdot \mathbf{D}_0 - \mathbf{H}_0 \cdot \mathbf{B}_0}. \quad (2.17)$$

By placing the dielectric post at a position of maximal electric field

$$\frac{\delta\omega_o - i\delta\alpha}{\omega_o} \simeq -2 \frac{V_1}{V_0} (\epsilon - 1). \quad (2.18)$$

From this result we conclude that by introducing a small dielectric post in the cavity, the real part of the dielectric constant  $\epsilon'$  is obtained from the lowering of the eigenfrequency,

$$\delta\omega_o = -2\omega_o \frac{V_1}{V_0} (\epsilon' - 1). \quad (2.19)$$

This result can easily be understood from the condition for resonance which says that the length of the cavity equals an integer times half the wavelength of the electromagnetic field. The wavelength is related to the frequency via the dispersion relation  $\nu\lambda = c/\sqrt{\mu\epsilon}$ . From this relation we see that introducing a dielectric in the cavity lowers the resonance frequency. The complex part of the dielectric constant  $\epsilon''$  is obtained from the increase of the width of the spectrum  $\delta\Gamma = 2\delta\alpha$ ;

$$\delta\Gamma = 4\omega_o \frac{V_1}{V_0} \epsilon''. \quad (2.20)$$

Fig. 2.5 shows the experimental reflection spectra at an empty cavity (+) and a cavity loaded with a capillary with toluene ( $\times$ ). The reflection spectrum at the cavity with toluene is shifted towards a lower resonance frequency, the width has increased with a few percentages. The solid lines are predictions from the Cavity Perturbation Model with the dielectric constant of toluene taken from literature. The reflection spectrum at the cavity is taken equal to one minus the spectrum of the cavity since the back side of the cavity reflects completely. Because the Cavity Perturbation Model does not describe the coupling of the waveguide to the cavity, this model does not contain information on the height of the dip. For a better comparison we have set the height (magnitude) of the dip equal to the experimental value. Fig. 2.6 shows the experimental reflection spectrum at an empty cavity (+) and a cavity loaded with a capillary with water ( $\times$ ). The solid lines are predictions from the Cavity Perturbation Model with the dielectric constant of water taken from literature. The difference between experiment and Cavity Perturbation

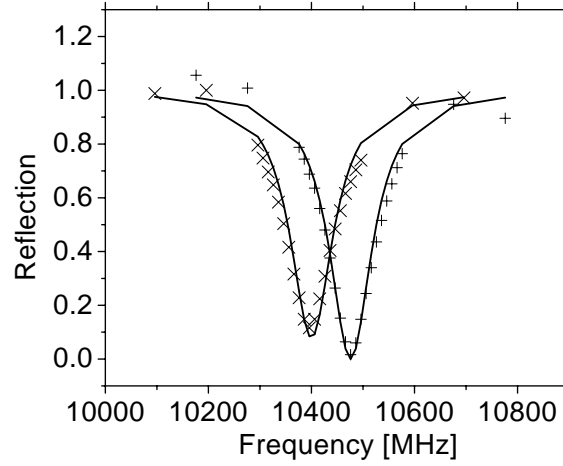


**Figure 2.5:** The experimental reflection spectrum at an empty cavity (+) is shown and the reflection at a cavity with a capillary filled with toluene ( $\times$ ) (filling factor  $2.6 \cdot 10^{-3}$ ). The capillary is placed at a position of maximal electric field. The solid lines are predictions from the Cavity Perturbation Model with the dielectric constant of toluene taken from literature ( $\epsilon = 2.38 + 0i$  [23]). The magnitude (depth) of the dips are not predicted by the Cavity Perturbation Model and are set equal to the experimental values.

Model for the shift in the resonance frequency and the increases in the width is of the order of 10 percent. The asymmetry in the reflection spectrum is due to parasitic reflections in the waveguide.

Table 2.1 shows the experimental values for the dielectric constant at 8.2 GHz, obtained with the Cavity Perturbation Model, and the corresponding values from literature. The indicated errors are measuring errors due to inaccuracy in the volume fraction and the position of the sample relative to the position of maximal electric field. The experimental values are in agreement with the values from literature, within the measuring accuracy. The measuring accuracy in  $\epsilon'$  and  $\epsilon''$  is of the order of ten percent, except for non lossy samples. For non absorbing samples, the spectral width of the cavity is determined by ohmic dissipation in the walls or radiative losses. For these samples, the accuracy in the loss factor  $\epsilon''$  is of the order of 0.1. We thus conclude that the first order approximation in  $V_1\epsilon$  of the Cavity Perturbation Model holds valid up to about ten percent, for a filling factor of the order of  $10^{-3}$  and a dielectric constant as large as that of water.

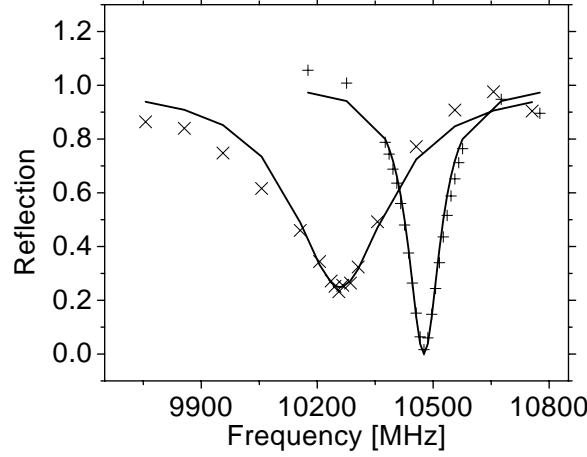


**Figure 2.6:** The experimental reflection spectrum at an empty cavity (+) is shown and the reflection at a cavity with a capillary filled with water ( $\times$ ) (filling factor  $1.1 \cdot 10^{-3}$ ). The capillary is placed at a position where the electric field is 0.45 of the maximal electric field. The solid lines are predictions from the Cavity Perturbation Model with the dielectric constant of water taken from literature ( $\epsilon = 60.6 + 25i$  at a frequency  $\nu = 10$  GHz [24]). The magnitude (depth) of the dips are not predicted by the Cavity Perturbation Model and set equal to the experimental values.

We now discuss how to tune the cavity sensitive for small changes in the dielectric constant of the sample. The coupling of the waveguide to the cavity is determined by the height of the metal pin at the front side of the cavity. Increasing the height of the pin decreases the response time of the cavity. From a Fourier transform of the energy in the cavity we know this corresponds to a decrease of the spectral width  $\Gamma$ . If the magnitude of the reflection decreases, the cavity is called overcoupled [25]. At a certain height of the pin, the reflection becomes minimal (zero at resonance frequency). The cavity is called critically coupled to the waveguide. At a further increase of the height of the pin, the magnitude of the reflection increases; the cavity is called undercoupled. Introducing an absorbing sample in the cavity more dissipation occurs in the cavity, reduces the cavity response time and the spectral width of the cavity increases. If the cavity is overcoupled, the introduction of an absorbing sample decreases the magnitude of the reflection. If the cavity is undercoupled, the introduction of an absorbing sample

	$\epsilon'$		$\epsilon''$	
	Experimental	Literature [24]	Experimental	Literature [24]
Water <sup>1</sup>	$62 \pm 3$	60.6	$24 \pm 2$	25
Quartz	$3.6 \pm 0.6$	3.85	$0 \pm 0.1$	$10^{-4}$
Ethanol <sup>1</sup>	$3.3 \pm 0.7$	2.9	$0.7 \pm 0.5$	0.33
KBr <sup>2</sup>	$4.8 \pm 0.5$	4.9	$0 \pm 0.1$	0.001
Selenium <sup>2</sup>	$8.5 \pm 0.7$	9.7	$0.9 \pm 0.3$	1.4
Toluene <sup>1</sup>	$2.3 \pm 0.1$	2.38[23]	$0.1 \pm 0.1$	0[23]

**Table 2.1:** The experimental values for the dielectric constant at 8.2 GHz, obtained with the Cavity Perturbation Model, are compared with the values from literature. <sup>1</sup> Liquid sample in quartz capillary. <sup>2</sup> Powder sample in quartz capillary. The dielectric constant of the capillary with dielectric is taken linear in the volume fractions of the constituents. All samples have a volume fraction of the order of  $10^{-3}$  to the volume of the cavity.

increases the magnitude of the reflection. This behaviour is shown in Fig. 2.7 for an undercoupled cavity.

Tuning the cavity close to critical coupling, the reflection close to the resonance frequency becomes small, and a large amplification of the reflected microwave power can be applied. In this way, small changes in the reflection, and finally in the dielectric constant  $\epsilon$ , can be measured.

The resolution for changes in the real part of the dielectric constant  $\delta\epsilon'$  is most easily evaluated from Eq. 2.19 that relates the change in  $\epsilon'$  to the change in the resonance frequency  $\nu_0$ , to obtain

$$\delta\epsilon = \frac{1}{f} \frac{\delta\nu}{\nu_0}. \quad (2.21)$$

In this expression  $f$  is the filling factor of the dielectric and  $\delta\nu$  the resolution in the resonance frequency. In our set-up, the (single shot) resolution in the frequency  $\delta\nu_0$  can be obtained as small as 1kHz (at maximum of microwave detector). For a non lossy sample, the filling factor can be taken as high as  $10^{-1}$  to obtain a resolution  $\delta\epsilon'$  of the order of  $10^{-6}$ . For a large lossy sample, the spectral width of the cavity is no longer determined by ohmic losses in the walls or radiative losses and the width becomes proportional to the filling factor. Because the frequency resolution is inversely proportional to the spectral width, the resolution in  $\epsilon'$  is smaller for lossy samples.

The resolution in the loss factor  $\epsilon''$  can be obtained from the increase in the spectral width or from the change in the magnitude of the reflection. In the Cavity

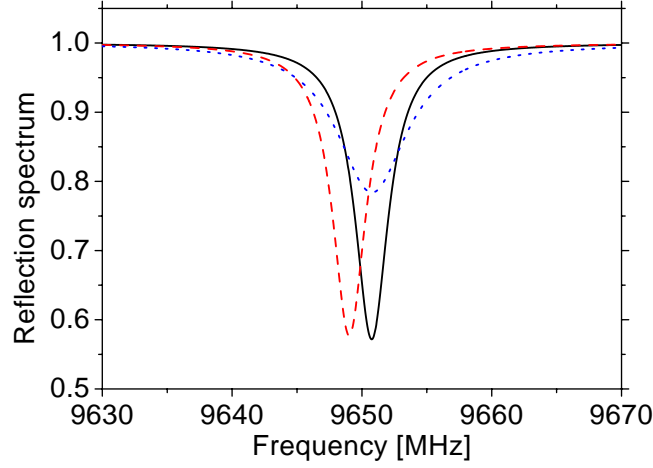


**Figure 2.7:** The reflection spectrum at an undercoupled cavity, loaded with a dielectric sample, calculated with the Transmission Line Model. In the next section we demonstrate this model accurately describes the reflection at a cavity. The solid line corresponds with a dielectric constant  $\epsilon = 4.0$ , the dashed line with  $\epsilon = 4.4$ , and the dotted line with  $\epsilon = 4.0 + 0.04i$ . The filling factor of the sample equals  $10^{-3}$ .

Perturbation Model, the height of the reflection is not described and only the width of the reflection can be predicted. From a measurement of the spectral width  $\Gamma$  one obtains a resolution in the loss factor  $\delta\epsilon''$  of only  $10^{-3}$ . This poor result is because amplification of the reflected microwave power can only be applied to frequencies close to resonance. At these frequencies the change in the reflection due to an increase in the width disappears. We conclude that amplification does not improve the resolution in the spectral width. The maximal electric field strength in the cavity is obtained at critical coupling. At resonance frequency no reflection at the cavity occurs and all microwave power from the generator  $P(\simeq 32 \text{ mW at maximum})$  disappears in the cavity. Because the electric energy in the cavity disappears out of the cavity on a time scale  $\Gamma^{-1} \simeq 10^{-7} \text{ s}$ , we conclude that the instantaneous electric energy in the cavity equals  $P\Gamma^{-1} \simeq 3 \cdot 10^{-9} \text{ J}$ . For a cavity with a length of 5 cm this corresponds to a maximal electric field strength of 78 V/cm.

## 2.6 Transmission Line Model

From a measurement of the change in the width of the reflection we obtain a sensitivity in the loss factor  $\epsilon''$  of about  $10^{-3}$ . The sensitivity in  $\epsilon''$  can become orders of magnitude better from a measurement of the height of the reflection. With the general Transmission Line Model [22] we are able to describe the coupling of the waveguide to the cavity and obtain the reflected microwave power as a function of the dielectric constant of the sample in the cavity. We test the accuracy of the model on reference samples and discuss the sensitivity for changes in the complex dielectric constant.

From section 2.4 we know that the electromagnetic waves in a uniform X-band waveguide (as in our set-up) are completely described by the constant complex amplitudes  $E_o^{\rightarrow}$  and  $E_o^{\leftarrow}$  of the right and left running electric waves. In order to obtain the power reflected at the cavity we calculate the reflection coefficient  $\frac{E^{\leftarrow}(z)}{E^{\rightarrow}(z)}$  as a function of the position  $z$  in the cavity and waveguide (see Fig. 2.8). In appendix A we show that a description of the electromagnetic waves in a waveguide is equivalent to a description in terms of the corresponding voltages and currents in the walls of the waveguide. We thus obtain that the reflection coefficient  $\frac{E^{\leftarrow}(z)}{E^{\rightarrow}(z)}$  is identical to the reflection coefficient  $\frac{V^{\leftarrow}(z)}{V^{\rightarrow}(z)}$  where  $V$  is the voltage between the upper and lower wall of the waveguide. Fig. 2.8 shows an electrical

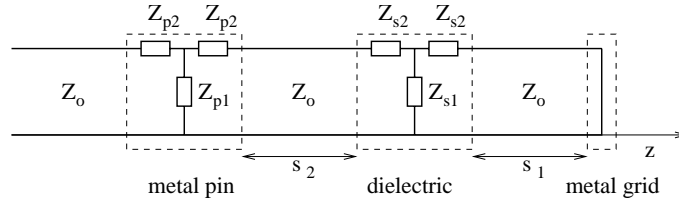


**Figure 2.8:** Electrical equivalent circuit of a microwave cavity consisting of a metal grid, a dielectric sample and a height adjustable metal pin.

equivalent circuit of the cavity used in our set-up. At one side the cavity is ended by a metal grid where the electric field vanishes i.e.  $E_o^{\rightarrow} = -E_o^{\leftarrow}$ . In terms of the voltage between both walls the metal grid corresponds to a short-circuit. From Eq. A.14 we obtain that the reflection coefficient at a distance  $s_1$  of  $z = 0$  is given by

$$\frac{E^{\leftarrow}(z = s_1)}{E^{\rightarrow}(z = s_1)} = \exp(2ik_z^* s_1) \frac{E_o^{\leftarrow}}{E_o^{\rightarrow}}. \quad (2.22)$$

In this expression  $k_z^* = k_z + i\gamma$  where  $\gamma$  is an absorption coefficient that describes

ohmic loss in the metal walls and radiative losses. The value for  $\gamma$  is experimentally obtained by fitting the reflection spectrum of an empty cavity with the model for the reflected power that we derive in this section ( $\gamma = 3.87 \cdot 10^{-2} \text{ m}^{-1}$ ).

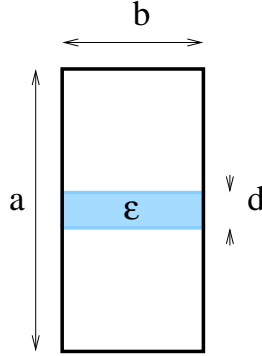


**Figure 2.9:** Cross section of the waveguide with a cylindric dielectric post placed in the middle of the waveguide, parallel to the electric field

Fig. 2.8 shows the general electric equivalent circuit for a cylindric dielectric post placed in the middle of the waveguide and aligned parallel to the electric field (see Fig. 2.9). For  $d/a < 0.1$  we can with an accuracy of a few percent reduce the circuit to a simple shunt impedance  $Z_{s1}$  ( $Z_{s2} = 0$ ) with

$$\frac{Z_o}{Z_{s1}} = \frac{-2iV\omega^2}{ab c^2 \pi k_z} (\epsilon^* - 1) \quad (2.23)$$

where  $\epsilon^*$  is the complex dielectric constant and  $V$  the volume of the dielectric [22]. The reflection coefficient  $(\frac{E^{\leftarrow}(z)}{E^{\rightarrow}(z)})_{out}$  at one side of a shunt impedance  $Z_1$  is obtained from the reflection coefficient  $(\frac{E^{\leftarrow}(z)}{E^{\rightarrow}(z)})_{in}$  at the other side of the impedance via [25]

$$\left(\frac{E^{\leftarrow}}{E^{\rightarrow}}\right)_{out} = \frac{E_{in}^{\leftarrow} + \frac{Z_0}{2Z_1}(E_{in}^{\leftarrow} + E_{in}^{\rightarrow})}{E_{in}^{\rightarrow} - \frac{Z_0}{2Z_1}(E_{in}^{\leftarrow} + E_{in}^{\rightarrow})}. \quad (2.24)$$

The electric equivalent circuit of the height adjustable metal pin can be approximated by a completely imaginary shunt impedance  $Z_{p1}$  ( $Z_{p2} = 0$ ). Thus we obtain an expression for the microwave power reflected at the cavity as a function of the dielectric constant of the sample. The value of  $Z_{p1}$  and the total length of the cavity  $s_1 + s_2$  are determined from the reflection spectrum of an empty cavity. The



volume of the dielectric  $V$  is measured by its weight or by an other independent method. The distance  $s_1$  is determined by placing the dielectric at a position of maximal electric field. This can easily be performed experimentally since for a given dielectric, the resonance frequency is minimal if the sample is at a position of maximal electric field.

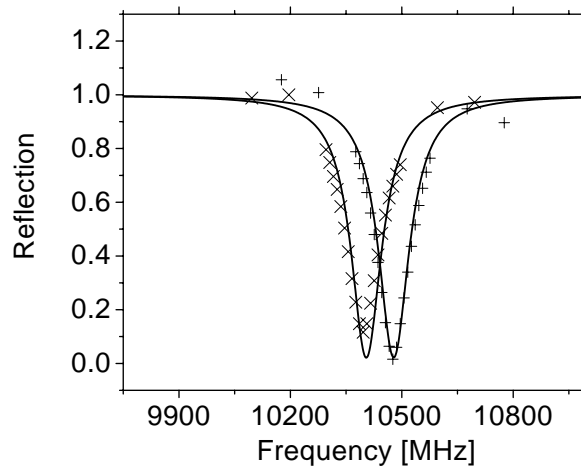


**Figure 2.10:** The reflection spectra of an empty, undercoupled cavity (+) and a cavity with a capillary filled with toluene (x) are shown. The capillary with toluene (filling factor  $2.6 \cdot 10^{-3}$ ) is placed at a position of maximal electric field. The solid lines are predictions from the Transmission Line Model with the dielectric constant of toluene taken from literature ( $\epsilon = 2.38 + 0i$  [24]).

Fig. 2.10 shows the reflection spectra of an empty, undercoupled cavity (+) and a cavity loaded with a capillary with toluene (x). The solid lines are the predictions from the Transmission Line Model with the dielectric constant of toluene taken from literature ( $\epsilon = 2.38 + 0i$  [23]). Fig. 2.11 shows the reflection spectra of an empty, undercoupled cavity (+), and a cavity loaded with a capillary with water (x) ( $\epsilon = 60.6 + 25i$  [24]). The difference in the magnitude of the reflection between the experiment and the Transmission line Model is due to the inaccurate description of our model.

Table 2.2 compares the dielectric constant of a few reference liquids, obtained with the Transmission Line Model, with literature values. To test the accuracy of our Transmission Line Model in the height of the reflection, the values for  $\epsilon''$  are obtained from the shift in the height of the reflection, and not from the

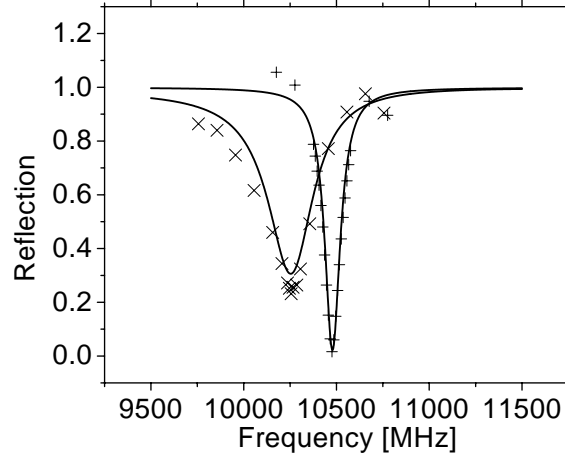


**Figure 2.11:** The reflection spectra of an empty, undercoupled cavity (+) and a cavity with a capillary filled with water (×) are shown. The capillary with water (filling factor  $1.1 \cdot 10^{-3}$ ) is placed at a position where the electric field is 0.45 of the maximal electric field strength. The solid lines are predictions from the Transmission Line Model with the dielectric constant of water taken from literature ( $\epsilon = 60.6 + 25i$  [24]).

	$\epsilon'$		$\epsilon''$	
	Experimental	Literature[24]	Experimental	Literature[24]
Toluene	$2.16 \pm 0.1$	2.38[23]	$0.1 \pm 0.1$	0[23]
Ethanol	$3.5 \pm 0.5$	2.6	$0.9 \pm 0.4$	0.3
Methanol	$12.2 \pm 3$	11.7	$7.3 \pm 0.8$	8.7

**Table 2.2:** The experimental values for the dielectric constant of a few liquids at 8.7 GHz, obtained with the Transmission Line Model, are compared with the values from literature. The imaginary part of the dielectric constant is obtained from the shift in the magnitude of the reflection (and not from the increase in the spectral width). The indicated errors are measuring errors for example due to inaccuracy in the volume fraction and the position of the sample relative to the position of maximal electric field. The dielectric constant of the capillary with dielectric is taken linear in the volume fractions of the constituents. All samples have a volume fraction of the order of  $10^{-3}$  to the volume of the cavity.

increase in the spectral width. The experimental values for  $\epsilon'$  are in agreement with the values from literature within the measuring accuracy. The difference in  $\epsilon''$  between the experiment and literature is larger than the measuring accuracy. The value for  $\epsilon''$  obtained from a measurement of the change in the height of the reflection, can be predicted by our model only with an accuracy of a factor two. Although the description of the magnitude of the reflection as a function of  $\epsilon''$  is not very accurate in our model, it is the best quantity to measure small changes in  $\epsilon''$  because of the good resolution in the reflection at resonance frequency with critical coupling. From the measurement of the reflected microwave power at two frequencies close to resonance frequency at critical coupling, we are able to calculate changes in  $\epsilon'$  and  $\epsilon''$  as small as  $10^{-6}$ .

An important feature of our method is that no contacts to the sample are needed. Disadvantages of our method are the time resolution of about 100 ns, and the limited frequency range of 8 to 12 GHz. Furthermore to describe the reflection at the cavity we need to make approximations. These approximations hold valid only for small samples and a small dielectric constant of the sample. Therefore only low conducting dielectrics can be studied. Applying electric contacts to the sample is difficult [27] just as in situ measurements. Another difficulty of our method is that heating expands the cavity and therefore lowers the resonance frequency (the sensitivity in the length of the cavity is of the order of a micrometer) while thermal expansion of the metal pin drives the cavity to undercoupling. For example, illumination of a sample with a halogen lamp through the metal grid causes heating of the cavity and which changes the reflection at a time scale of seconds. Heating by air or by ohmic dissipation of microwaves in the walls is much slower and can be neglected.

## 2.7 Conclusions

Reflection measurements at a resonant microwave cavity loaded with a small, non-conductive dielectric sample are well suited for the contactless measurement of the complex dielectric constant. The real part is accurately obtained from the shift in the resonance frequency, the complex part from the increase in the width of the spectrum, as described in the Cavity Perturbation Model. The sensitivity of this method is of the order of  $10^{-6}$  for changes in  $\epsilon'$  and  $10^{-3}$  for changes in  $\epsilon''$ . The sensitivity for changes in  $\epsilon''$  can be improved to  $10^{-6}$  from a measurement of the magnitude of the reflection, which can be described with the Transmission Line Model.



## References

---

- [1] N. Hill, W. Vaughan, A. Price and M. Davies, *Dielectric properties and molecular behaviour*, Van Nostrand Reinhold Company, 1969.
- [2] C. Bottcher and P. Bordewijk, *Theory of electric polarization*, Elsevier Scientific Publishing Company, 1978.
- [3] J. Hearn, B. Howard, Mol. Phys. **100**, 2679 (2002).
- [4] S. Chakrabarti, A. jaman, J. Mol. Struct. **612**, 103 (2002).
- [5] N. Heineking, J. Grabow, and I. Merke, J. Mol. Struct. **612**, 231 (2002).
- [6] S. Levchenko, A. Krylov, J. Phys. Chem. A **106**, 5169 (2002).
- [7] J. Kroeze, T. Savenije and J. Warman, J. Photoch. Photobio. A **148**, 49 (2002).
- [8] J. Salafsky, W. Lubberhuizen, E. van Faassen, and R. Schropp, J. Phys. Chem. B **102**, 766 (2002).
- [9] B. Wegewijs, L. Siebbeles, N. Boden, R. Bushby, B. Movaghar, O. Lozman, Q. Liu, A. Pecchia, and L. Mason, Phys. Rev. B **65**, 245112 (2002).
- [10] T. Savenije and J. Warman, Macromolecules **33**, 60 (2000).
- [11] M. de Haas, M. Kunst, J. Warman, J. Verberne, J. Phys. Chem. **87**, 4089 (1983).
- [12] R. Hoofman, M. deHaas, L. Siebbeles, and J. Warman, Nature **392**, 54 (1998).
- [13] S. Kasouit, S. Kumar, R. Vanderhaghen, P. Cabarrocas, I. French, J. Non-cryst. Solids **299**, 113 (2002).
- [14] S. Kasouit, S. Kumar, R. Vanderhaghen, P. Cabarrocas, I. French, J. Non-cryst. Solids **299**, 365 (2002).
- [15] F. Liu, M. Zhu, Y. Feng, Y. Han, J. Liu, S. Kasouit, and R. Vanderhaghen, J. Non-cryst. Solids **299**, 385 (2002).
- [16] O. Hahneiser, M. Kunst, J. Appl. Phys. **85**, 7741 (1999).
- [17] C. Swiatkowski, M. Kunst, Appl. Phys. A **61**, 623 (1995).
- [18] J. Elmiger, R. Schieck, M. Kunst, J. Vac. Sci. technol. A **15**, 2418 (1997).
- [19] H. Neitzert, M. Kunst, J. Vac. Sci. Technol. A **13**, 2753 (1995).
- [20] W. Atkinson, P. Hirschfeld, Phys. Rev. Lett. **88**, 187003 (2002).
- [21] C. Kusko, Z. Zhai, N. Hakim, et al., Phys. Rev. B **65**, 132501 (2002).
- [22] R. Waldron, *Theory of guided electromagnetic waves*, Van Nostrand Reinhold Company, 1969.

- [23] D. Lide, *Handbook of Chemistry and Physics* 72nd edition, CRC Press, 1992.
- [24] R. von Hippel, *Dielectric materials and applications*, The M.I.T. press, 1954.
- [25] M. Sucher and J. Fox, *Handbook of microwave measurements Volume II*, J. Wiley, 1963.
- [26] N. Marcuvitz, *Waveguide Handbook 10*, Mc Graw-Hill, 1951.
- [27] F. de Weerd, Masters Thesis, Utrecht University, 1998.

## 3 Short range electron motion in semi-conducting macroporous GaP

---

### 3.1 Abstract

Studies of long-range electron transport in porous semiconductors have shown that the effective mobility is strongly reduced with respect to that of single crystalline bulk semiconductors. This strong attenuation of electron transport has been attributed to multiple trapping/detrapping in states located at the internal surface of the porous solid. Here, we report microwave reflectivity measurements on a dark and illuminated macroporous GaP network which allow us to probe the trap-free mobility of electrons present inside the core of the network. We obtain the imaginary and real component of the dielectric constant, and the changes of these variables as a function of the incident light intensity. We show that the changes in the real and imaginary parts of the dielectric constant as a function of the light intensity are correlated and can be interpreted on the basis of a hydrodynamic model. We find that the short-range electron mobility is  $3 \text{ cm}^2/\text{Vs}$ . We compare this value with the mobility obtained from Hall-measurements on single crystals and the effective mobility characterizing long-range transport through a porous GaP network. The transient changes in the dielectric constant upon excitation with a laser pulse and with constant illumination reflect the dynamics of electron-hole photogeneration and bulk and surface recombination in the porous GaP network.

### 3.2 Introduction

Porous semiconductors, which consist of electrically connected (nanometer-sized) crystals or of a single-crystalline network, have attracted much interest in the last decade [1]. These materials show some interesting optical and photo-electric properties. For example, because of multiple scattering of light in the porous matrix, absorption of light can be stronger than in the corresponding bulk semiconductor [2]. Trapping of charge carriers in surface states considerably increase the lifetime of photoexcited carriers. Porous electrodes immersed in an electrolyte that plays the role of hole scavenger have shown photocurrent quantum efficiencies equal to one [3]. Therefore these systems show promising properties for application in batteries, (photoelectrochemical) solar cells [4,5], electrochromic

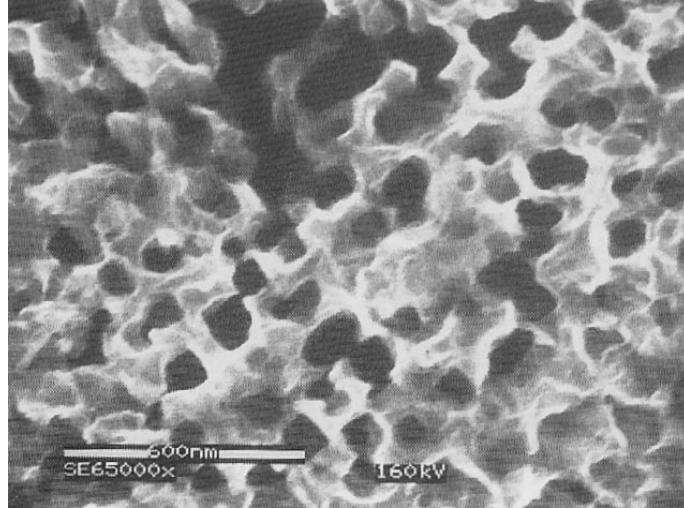


**Figure 3.1:** SEM micrograph of anodic etched porous GaP. Dark areas indicate the absence of GaP material.

windows [6,7], light emitting diodes [8], and photonic devices. In addition, porous semiconductors offer a set of challenging fundamental questions dealing with the short and long-range transport of electrons and holes, and their recombination dynamics. Electron transport in porous semiconductors, such as  $\text{TiO}_2$ ,  $\text{ZnO}$  and  $\text{GaP}$ , has been studied by a number of methods that measure the response of a photoelectrochemical device to a small-amplitude modulation of the absorbed light intensity<sup>7–14</sup>. Measurements on classic metal/semiconductor/metal systems have also been performed [9]. In the case of macroporous  $\text{GaP}$  and microporous  $\text{TiO}_2$  electrodes, it has been shown that the transport-characteristics are non-dispersive (Gaussian or normal); this means that all the photogenerated electrons behave in a similar way and can be described by mean transport parameters [10]. One can thus use an effective mobility (often called drift mobility) to quantify the long-range electron motion [11,12,13,14]. Nonetheless, long-range electron transport in porous semiconductors is strongly attenuated: the measured effective mobilities are two to five orders of magnitude smaller than those reported for the non-porous single crystalline counterparts (obtained from Hall conductivity measurements). This has been attributed to multiple trapping/detrapping in localized energy levels located at the huge internal surface of the porous matrix. It has proven very difficult, however, to quantify the contribution of surface trapping in long-range transport by independent methods. In this respect, it would be of interest to mea-



sure the trap-free conduction mobility  $\mu$  of electrons in a *porous semiconductor*.

In this paper we investigate the short-range motion of electrons in macroporous GaP by measurement of the interaction with microwaves. The motivation for this work is twofold. The main interest of this work can be appreciated by examining Figs. 3.1 and 3.2. Fig. 3.1 shows a SEM micrograph of the porous GaP that we have used. Fig. 3.2 a) sketches the energetics in the structural units under the given conditions; macroporous GaP can be mimicked by spheres (radius 75 nm), which consist of a *semiconducting* core (radius denoted as  $R_c$ , electron density  $n = 3 \times 10^{17} \text{cm}^{-3}$ ), surrounded by a region depleted of electrons. The depleted shell is due to the trapping of free electrons in surface states of energy in the band gap. The precise dimensions of both regions and their variations under illumination will be considered below. Fig. 3.2 b) shows the penetration of the microwave electric field  $E$  in the structural units of this matrix, calculated with a hydrodynamic model discussed below. The field penetration according to the Mie model is also shown for comparison. It can be seen that the microwave field penetrates the *semiconducting* cores to a depth equal to the Debye screening length  $L$ , which is here about 6 nm (see further). The distance that an electron can migrate during one period of the microwave  $2\pi/\omega$  is equal or less than  $\mu E 2\pi/\omega$ , which is about 1 nm. Thus, the microwaves probe the electrons residing at the interface between the semiconducting core and the depleted region. These electrons are sufficiently remote from the surface; measurement of the short-range electron motion by microwave reflection should, therefore, provide the "bulk" mobility of the electrons in the porous matrix, free from the effects of surface trapping. This work is thus complementary to methods that measure the long-range transport parameters which are determined by surface trapping/detrapping.

A second motivation for this work is related to the interpretation of the results obtained with illuminated nanostructured semiconductors, probed with the (Time Resolved) Microwave Conductivity method. The pioneering works of Deri et al. [15] and Grabtchak et al. [16] on polycrystalline semiconductors (AgCl, and CdSe) showed that the microwave absorption and the shift of the cavity resonance frequency provide the changes in the imaginary ( $\Delta\epsilon''$ ) and real component ( $\Delta\epsilon'$ ) of the dielectric constant due to photo-excitation of the nanostructured semiconductor. Interpretation of  $\Delta\epsilon'$  and  $\Delta\epsilon''$  is, however, less straightforward. Deri and Grabtchak attributed  $\Delta\epsilon''$  to microwave absorption by photogenerated *free* carriers, while  $\Delta\epsilon'$  was believed to correspond to *trapped* carriers. The observations that the decay of  $\Delta\epsilon'$  and  $\Delta\epsilon''$  transients show the same time constants and that  $\Delta\epsilon'$  and  $\Delta\epsilon''$  depend in the same way on the intensity of photogeneration were attributed to fast equilibration between trapped and free charge carriers. This correlation between  $\epsilon'$  and  $\epsilon''$  can be explained [17] from the dielectric properties of

a dilute electron gas confined to a small region of space, like a small dielectric particle. This hydrodynamical model shows that photogeneration of excess free carriers in such a system leads to an increase of both  $\Delta\epsilon''$  and  $\Delta\epsilon'$ ; it thus provides a natural explanation for the previously reported correlation between  $\Delta\epsilon''$  and  $\Delta\epsilon'$ . In appendix B this hydrodynamic model is extended and adapted to the case of semiconducting spheres surrounded by a dielectric shell. The experimental results that we present can be understood quantitatively by this model. In section III it will be shown that  $\Delta\epsilon''$  and  $\Delta\epsilon'$  correspond to the expansion of the semiconducting regions in the porous matrix (see Fig. 3.2) due to the photogeneration of excess free electrons and we discuss how we obtain from these quantities a value for the mobility  $\mu$  inside the semiconducting part and the radius of the semiconducting part  $R_c$ . In section IV, interpretation of  $\Delta\epsilon'$  and  $\Delta\epsilon''$  measured under steady-state conditions as a function of the incident light intensity, and of the transient  $\Delta\epsilon'$  and  $\Delta\epsilon''$  upon turning on and off photo-excitation provide novel information on the electron-hole recombination dynamics in porous semiconductors. In section IV we show how the change in  $\epsilon$  upon excitation with a laser pulse provides information on the electron-hole recombination on a time scale of 100 nanoseconds to a second.

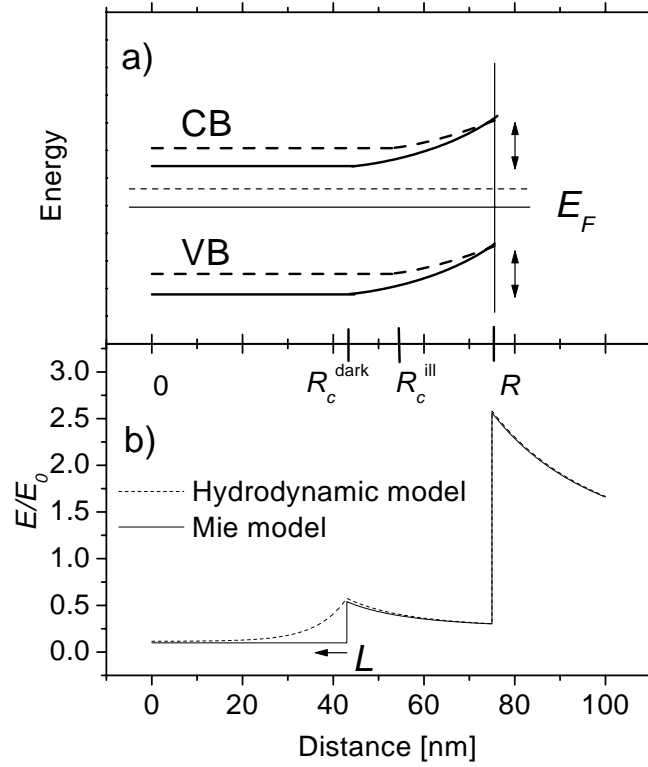


**Figure 3.2:** a) Schematic drawing of the edges of the conduction band (CB) and valence band (VB) with respect to the Fermi level  $E_F$  for macroporous GaP in the dark (solid line) and under illumination (dashed line) (the bandgap is 2.3eV). The band-bending ( $\simeq 0.3$  eV) is indicated with an arrow. A GaP sphere is used as a model; the sphere has an outer radius  $R$  of 75 nm and consists of a semiconducting core with radius  $R_c$  surrounded by a depletion layer. b) The amplitude of the microwave-induced electric field in the nano-particle relative to the amplitude of the applied microwave electric field  $E_0$  is shown as a function of the distance in the direction of the applied field. In the hydrodynamic model the screening of the electric field in the conducting part occurs on a length scale of the Debye screening length  $L(=6.3\text{nm})$ . In the Mie model the electric field changes discontinuously at the interface of the conducting and depleted regions. Outside the particle, the electric field falls off due to the induced dipole.

### 3.3 Experimental

Single crystalline n-type GaP is made porous by anodic etching in a sulphuric acid solution. Afterwards, the porosity of the anodically etched GaP is further increased from 25% to 50% by photo-anodic etching in a  $H_2O : H_2SO_4 : H_2O_2$  electrolyte using 1.96 eV sub-band gap light [18].

Scanning Electron Microscopy analysis (Fig. 3.1) reveals that we obtain a randomly porous matrix [19,20]. The GaP structures in this network have a typical length scale of about 150 nm. X-ray diffraction measurements show that the semiconducting part in the porous structure is single crystalline [19]. For the microwave measurements 5 milligrams of porous material is scraped off the porous GaP electrode and compressed in a quartz capillary. The filling factor  $f$  of GaP in the capillary is 0.4. The dielectric constant of porous GaP is obtained from the measurement of the microwave reflection spectrum at a cavity loaded with the capillary (see chapter II). The microwave cavity consists of an X-band waveguide terminated at one side by a metal grid through which optical access is possible. The other end consists of a height-adjustable metal pin which only partially reflects the microwaves. The microwave power reflected at this cavity is amplified, downconverted in a detector and displayed on an oscilloscope. By changing the height of the metal pin, we can reduce the reflection at the resonance frequency. In this way a large amplification can be achieved and the reflection spectrum can be measured very accurately. The reflection spectrum is only slightly perturbed by loading the cavity with a dielectric with a volume much smaller than the volume of the cavity and with a complex dielectric constant with a modulus close to 1. The decrease of the resonance frequency is then proportional to the real part of the dielectric constant  $\epsilon'$ , the increase of the width of the spectrum is proportional to the complex part of the dielectric constant  $\epsilon''$  [21]. A quantitative description of the change of the reflected spectrum as a function of the dielectric constant is calculated with the Transmission Line Model [22].

Porous GaP was illuminated in the cavity with a halogen lamp equipped with a filter transparent between 400 and 600 nm. Changes in  $\epsilon'$  and  $\epsilon''$  were measured as a function of the incident light intensity (see Fig. 3.3). In addition the transient changes of  $\epsilon'$  and  $\epsilon''$  upon turning the light on and off were recorded (see Fig. 3.8). For excitation with a laser pulse we used a 50 Hz Quanta Ray Nd-YAG laser. The frequency tripled (355 nm) output pumped an optical parametrical oscillator (OPO, Spectra Physics), generating pulses of 10 ns duration with an energy of 7mJ/pulse over an area of 1 cm<sup>2</sup>. Heating of the sample by the illumination causes an estimated increase of the temperature of less than 10<sup>-2</sup> K, which corresponds to changes in the dielectric constant two orders of magnitude smaller than the values

we obtained. All measurements are performed at room temperature in contact with air.

### 3.4 Determination of the short range mobility

The dielectric constant of porous GaP in the dark obtained from the microwave measurements (at a frequency of 8 GHz) is  $\epsilon' + i\epsilon'' = 2.57 \pm 0.15 + i0.07 \pm 0.05$ . In a linear approximation, the dielectric constant of a mixture of air with a crystal with volume fraction  $f$  is given by  $\epsilon = (1 - f) + f \cdot \epsilon_{crystal}$ . In this expression  $\epsilon_{crystal}$  is the effective dielectric constant of crystalline GaP which is the sum of the contributions from the bound electrons  $\epsilon_b (=8.5)$ [23] and the free electrons, described by a Drude term  $i\sigma/\omega$ . The conductivity of the free electrons at a radial frequency  $\omega$  is denoted by  $\sigma$ . For our doped crystalline GaP  $\epsilon_{crystal} = 8.5 + i1122.0$ . With the independently determined value for  $f (= 0.4)$  we then obtain  $\epsilon = 4.0 + i448.8$ . This approximation thus overestimates the imaginary part of porous GaP by several orders of magnitude. In appendix B a more realistic model is developed which takes into account surface polarization at the GaP spheres.

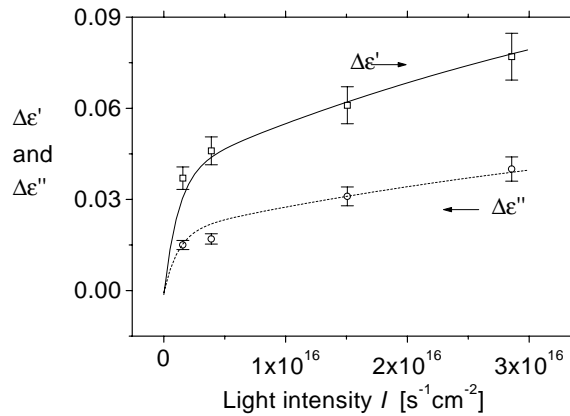


**Figure 3.3:** The change in the complex dielectric constant of porous GaP  $\Delta\epsilon$  as a function of the incident photon flux  $I$ . The experimental values for  $\Delta\epsilon'$  and  $\Delta\epsilon''$  are depicted as (□) and (○), respectively. These values are fitted with the hydrodynamic model by choosing the mobility  $\mu = 3 \text{ cm}^2/\text{Vs}$  and the radius of the semiconducting part in the dark  $R_c(\text{dark})=45 \text{ nm}$ . The procedure is discussed in the text.

Fig. 3.3 shows the changes in the dielectric constant of porous GaP under illumination as a function of the incident light intensity. Because the optical absorption length of photoanodically etched porous GaP ( $\alpha^{-1} \simeq 2 \cdot 10^{-6} \text{ m}$  [2]) is

much smaller than the diameter of the sample ( $6 \cdot 10^{-4}$  m), only a small strip of the sample is illuminated. From the change in the dielectric constant of the whole sample  $\Delta\epsilon_S$ , as a function of the incident light intensity, and the absorption length, we can calculate the change in the local dielectric constant  $\Delta\epsilon$ , as a function of the local light intensity. From a numeric computation we obtain that the change in the local dielectric constant at the front side of the sample  $\Delta\epsilon$  is about  $11 \pm 1$  times the change in the dielectric constant of the whole sample  $\Delta\epsilon_S$ . The change in the real part of the dielectric constant  $\Delta\epsilon'$  is of the same order and has the same sign as the imaginary part  $\Delta\epsilon''$ . The ratio  $\Delta\epsilon'(I)/\Delta\epsilon''(I)$  is constant for all light intensities used in our experiments and has a value  $\Delta\epsilon'/\Delta\epsilon'' = 2.0 \pm 0.1$ . We remark that the same ratio is found in time resolved measurements (see Fig. 3.8). The experimental accuracy in  $\Delta\epsilon'/\Delta\epsilon''$  is good because one needs to measure only small perturbations in  $\epsilon$  and only the *ratio* of the real and imaginary part is involved.

Note that in the linear approximation of the dielectric constant  $\epsilon$ , with a conductivity given by  $\sigma = \frac{ne^2\tau}{m(1-i\omega\tau)}$  ( $e$  is the elementary charge,  $m$  the effective mass of the charge carrier,  $\tau$  the momentum relaxation time and  $n$  the density), an increase in the charge carrier density corresponds to a ratio  $\Delta\epsilon'/\Delta\epsilon'' = -\omega\tau$ . In our experiments this would correspond to a negative (!) ratio  $\Delta\epsilon'/\Delta\epsilon'' = -10^{-5}$  which is five orders of magnitude smaller than the experimental value!

In appendix B we calculate the dielectric constant  $\epsilon$  of a collection of semiconducting spheres of GaP (radius  $R_c$ ) surrounded by a shell of (dielectric) GaP, depleted of free electrons. This calculation is an extension of the hydrodynamic model that has been previously presented [17]. This model shows that the increase of  $\Delta\epsilon'(I)$  and  $\Delta\epsilon''(I)$  is due to the increase in the radius  $R_c$  of the semiconducting spheres in the GaP matrix with increasing light intensity  $I$ . A fit of  $\Delta\epsilon'(I)$ ,  $\Delta\epsilon''(I)$  by this model is presented by the solid lines in Fig. 3.3 (details are given below).

In Fig. 3.4 we have plotted the ratio  $\Delta\epsilon'/\Delta\epsilon''$ , calculated with the hydrodynamic model, as a function of the mobility  $\mu$ , for different values of the radius  $R_c(\text{dark})$  of the nondepleted core in the dark. The change in the dielectric constant is calculated as  $\Delta\epsilon(I) = \epsilon(R_c(I)) - \epsilon(R_c(\text{dark}))$  assuming  $R_c(I) - R_c(\text{dark}) = 5$  nm, a realistic change as can be seen below. From Fig. 3.4 we conclude that with an experimental value  $\Delta\epsilon'/\Delta\epsilon'' = 2.0 \pm 0.5$  the mobility  $\mu$  must lie between 1 and 5  $\text{cm}^2/\text{Vs}$  for all reasonable values for  $R_c(\text{dark})$  ( $0 \leq R_c(\text{dark}) \leq R$ ). No information about the radius  $R_c(\text{dark})$  is obtained from this plot.

In Fig. 3.5 we show the real part of the dielectric constant of porous GaP in the dark, calculated with the hydrodynamic model, as a function of the mobility  $\mu$  for different values of the radius  $R_c$ . From the fit of  $\Delta\epsilon'/\Delta\epsilon''$  we know that the mo-

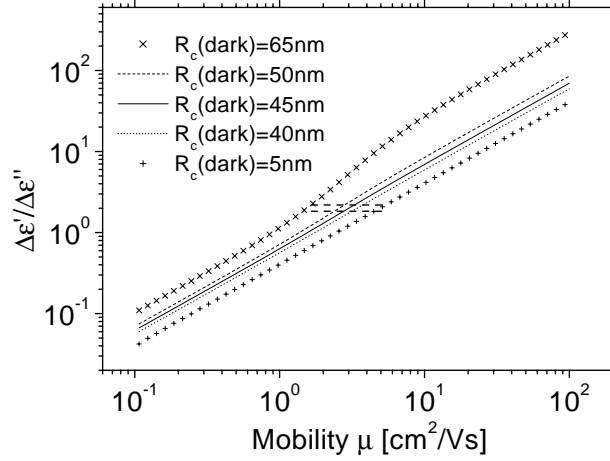


**Figure 3.4:** The ratio  $\Delta\epsilon'(I)/\Delta\epsilon''(I)$ , calculated with the hydrodynamic model, is shown as a function of the mobility  $\mu$  of free electrons in the semiconducting core, for different values of the radius of the semiconducting core  $R_c$ . The change in the dielectric constant is calculated as  $\Delta\epsilon(I) = \epsilon(R_c(I)) - \epsilon(R_c(\text{dark}))$  with  $R_c(I) - R_c = 5$  nm. With an experimental value  $\Delta\epsilon'/\Delta\epsilon'' = 2.0 \pm 0.5$  we conclude that the mobility lies between 1 and 5  $\text{cm}^2/\text{Vs}$ . (Only the lines that pass through the rectangle are compatible with the experimental value  $\Delta\epsilon'/\Delta\epsilon'' = 2.0 \pm 0.5$ .)

bility  $\mu$  is between 1 and 5  $\text{cm}^2/\text{Vs}$ . With an experimental value  $\epsilon' = 2.57 \pm 0.15$  and a mobility  $\mu$  between 1 and 5  $\text{cm}^2/\text{Vs}$ , we conclude that the radius  $R_c(\text{dark})$  must be between 40 and 75 nm. In Fig. 3.6 we show the imaginary part of the dielectric constant of porous GaP in the dark, obtained with the hydrodynamic model, as a function of the mobility  $\mu$  for different values of the radius  $R_c$ . With an experimental value  $\epsilon'' = 0.07 \pm 0.05$  and a mobility  $\mu$  between 1 and 5  $\text{cm}^2/\text{Vs}$ , we conclude that the radius  $R_c$  must be between 50 and 5 nm.

In summary we have shown that a combination of the results obtained from the fitting of  $\Delta\epsilon'/\Delta\epsilon''$  and from the values of  $\epsilon'$  and  $\epsilon''$  in the dark provides the mobility inside the nondepleted core of macroporous GaP  $\mu = 3 \pm 1 \text{ cm}^2/\text{Vs}$  and the radius of the semiconducting part in the dark  $R_c(\text{dark}) = 45 \pm 5$  nm.

The value for the mobility  $\mu$  inside the GaP particle is about a factor 40 smaller than that in bulk GaP obtained with Hall measurements [24,25];  $\mu = 130 \text{ cm}^2/\text{Vs}$ . At present, the reason for this difference is not clear. Because of screening, the



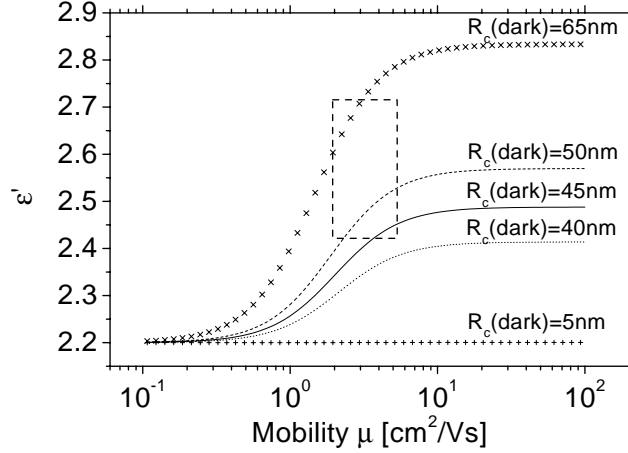


**Figure 3.5:** The real part of the dielectric constant of porous GaP in the dark, calculated with the hydrodynamic model, is shown as a function of the mobility  $\mu$  for different values of the radius  $R_c(\text{dark})$ . With an experimental value  $\epsilon' = 2.57 \pm 0.15$  and a mobility  $\mu$  between 1 and 5  $\text{cm}^2/\text{Vs}$ , we conclude that the radius  $R_c$  must be between 40 nm and 75 nm. (Only the lines that pass through the rectangle are compatible with the experimental value  $\epsilon' = 2.57 \pm 0.15$  and  $\Delta\epsilon'/\Delta\epsilon'' = 2.0 \pm 0.5$ .)

polarizability of the semiconducting sphere is determined essentially by the properties of the non-depleted region at a distance of the screening length from the depletion layer. Up to now we have assumed that the free electron density equals  $n_0$  inside the non-depleted layer and zero inside the depletion layer. A more accurate description of the electron density at the depleted/non-depleted interface may influence the electron mobility that is obtained from the polarizability.

Long-range transport through completely depleted macroporous GaP has been studied by light intensity modulated photocurrent spectroscopy [12]. The effective mobility ranged between  $10^{-2}$  (at high light intensity) and  $10^{-5} \text{cm}^2/\text{Vs}$  (at low light intensity) and is thus two-five orders of magnitude smaller than the short-range mobility obtained by microwave reflectivity measurements with structural identical macroporous GaP. In addition, the short-range mobility that we obtain is independent of the incident light intensity and thus of the position of the electron Fermi-level in macroporous GaP. These contrasting results highlight the differences between long-range electron transport (with transport paths of 10-200  $\mu\text{m}$

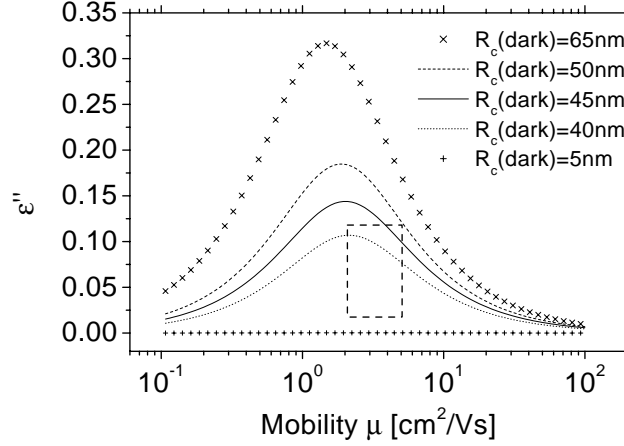


**Figure 3.6:** The imaginary part of the dielectric constant of porous GaP in the dark, calculated with the hydrodynamic model, is shown as a function of the mobility  $\mu$  for different values of the radius  $R_c$ . With an experimental value  $\epsilon'' = 0.07 \pm 0.05$  and a mobility  $\mu$  between 1 and 5  $\text{cm}^2/\text{Vs}$ , we conclude that the radius  $R_c$  must be between 50 and 0 nm. (Only the lines that pass through the rectangle are compatible with the experimental value  $\epsilon'' = 0.07 \pm 0.05$  and  $\Delta\epsilon'/\Delta\epsilon'' = 2.0 \pm 0.5$ .)

through the porous network) attenuated by multiple trapping/detrapping and short-range motion (transport path 1 nm) in the interior of the network far from surface localized traps.

Deri and Spoonhower [15] studied the photoinduced changes  $\Delta\epsilon'$ ,  $\Delta\epsilon''$  upon illumination of a AgCl powder. They found that  $\Delta\epsilon'$  and  $\Delta\epsilon''$  were correlated, as in the case reported here. Very likely, the origin of  $\Delta\epsilon'$ ,  $\Delta\epsilon''$  is similar to that for GaP i.e. an expansion of the semiconducting region inside the AgCl nanocrystals upon illumination.

### 3.5 Electron-hole recombination under constant illumination

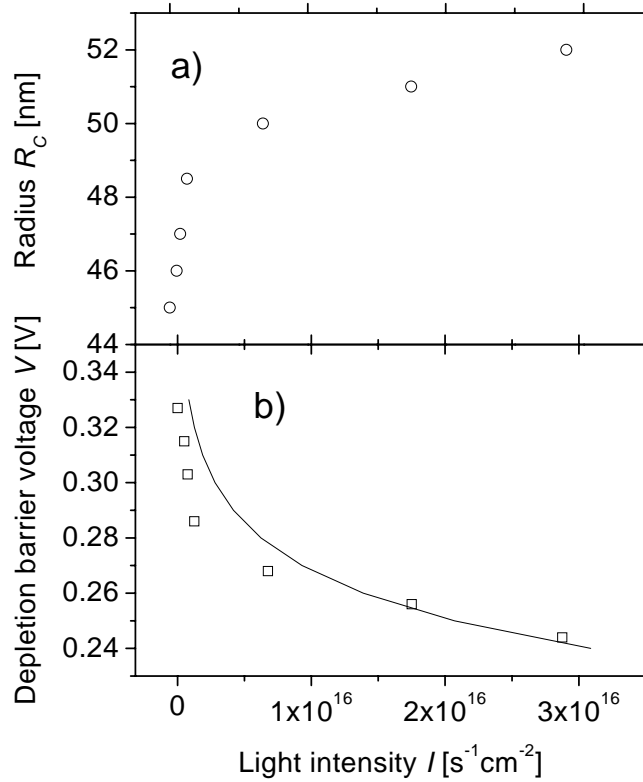


**Figure 3.7:** a) The radius  $R_c$  of the semiconducting core ( $\circ$ ) in the macroporous GaP matrix obtained from Fig. 3.3 and b) the potential difference across the depletion layer ( $\square$ ) surrounding the core, calculated with Eq. 3.1 is shown as a function of the incident light intensity. The experimental values for the potential are fitted with Eq. 3.3.

With the values for  $\mu$  and  $R_c(\text{dark})$  we can fit the changes in the complex dielectric constant under illumination by increasing the radius  $R_c$  (see Fig. 3.3). In Fig. 3.7 we have plotted the radius of the semiconducting part  $R_c$  as a function

of the light intensity as obtained from the fit in Fig. 3.3. The electrostatic potential difference over the depletion layer  $V$  (which is four orders of magnitude larger than the microwave induced potential difference over the depletion layer) can be related to the width of the depletion layer  $R - R_c$  via [27]

$$V = \frac{en}{3\epsilon\epsilon_0} \left( \frac{1}{2}R^2 - \frac{3}{2}R_c^2 + \frac{R_c^3}{R} \right), \quad (3.1)$$

where  $\epsilon$  is the static dielectric constant of undoped GaP. The potential difference over the depletion layer is also shown in Fig. 3.7.

Fig. 3.8 shows the transients  $\Delta\epsilon'$  and  $\Delta\epsilon''$  upon turning on and off the illumination. It is clear that  $\Delta\epsilon'$  and  $\Delta\epsilon''$  are correlated i.e. show the same time dependence. This further supports our explanation on the basis of the hydrodynamic model. We remark that correlated  $\Delta\epsilon'$  and  $\Delta\epsilon''$  transients have also been reported for polycrystalline CdS electrodes [16]. The  $\epsilon$  transient is multiexponential, on a very slow time scale of seconds to minutes. This reflects that the photogenerated electrons have to overcome the energy barrier of the depletion layer before recombination at the surface is possible. The first milliseconds after switching on the illumination, the change in the potential is linear in time. In the inset, we have plotted the initial rate of change of the depletion layer  $dV/dt$  as a function of the light intensity  $I$ . The initial decay  $dV/dt$  is linear in  $I$ .

The increase in the radius of the semiconducting sphere  $R_c$  upon illumination is due to the photogeneration of excess free electrons. We explain the transients and the increase of  $R_c$  with  $I$  by a model that accounts for photogeneration in the bulk GaP and recombination at the surface and in the bulk.

Illumination with light with a photon energy  $h\nu$  larger than the band gap (2.3 eV for GaP) generates electron-hole pairs. Since the absorption length  $\alpha^{-1}$  for light with this photon energy ( $\alpha^{-1} = 2 \times 10^{-5}$  m) is much larger than the particle radius  $R$ , the creation of electron-hole pairs can be considered as uniform in a GaP sphere and the total rate of electron-hole pair generation in the particle equals  $\frac{4}{3}\pi R^3 \alpha I$  where  $I$  is the incident photon flux. Since the diffusion length for holes  $L_p = 80$  nm [28] is larger than the radius of the particle, every hole reaches the surface; this occurs on a time scale  $t_d$  which is given by the equation

$$R = \left( \frac{k_B T}{e} \mu_h t_d \right)^{1/2} \quad (3.2)$$

where  $\mu_h$  is the hole-mobility. For our GaP particles this diffusion time  $t_d$  is  $10^{-11}$  s and thus much smaller than the time resolution of our measuring method. A fraction  $f_s$  of the holes becomes trapped in a surface state, the rest recombines in the bulk. Independent measurements on GaP single crystal electrodes

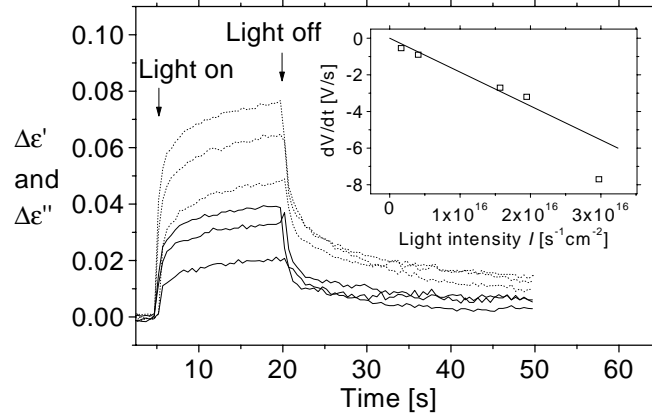


**Figure 3.8:** The transients in the real part (dotted line) and imaginary part (solid line) of the dielectric constant of porous GaP upon switching on and off the illumination for different light intensities ( $I = 1.25, 3.8$  and  $12.5 \times 10^{15} \text{ s}^{-1} \text{ cm}^{-2}$ ). Insert: Rate of decay of the potential difference across the depletion layer  $dV/dt$ , measured a few ms after turning on the light, as a function of the incident light intensity.

(photoluminescence, electroluminescence and photocapacitance) have shown that electrons and holes recombine in the bulk solid as well as the surface[29]. The change in the number of free electrons in a semiconducting particle per unit time under illumination thus becomes

$$\frac{dN}{dt} = -4\pi R^2 n \exp \frac{-eV}{kT} \beta_n S + \frac{4}{3} \pi R^3 \alpha I f_s + \frac{4}{3} \pi R^3 g_{th} f_s. \quad (3.3)$$

The first term describes the trapping rate of free electrons in surface states. This rate is proportional to the number of free electrons at the surface  $n \exp \frac{-eV}{kT}$ , to the capture rate for free electrons in surface states  $\beta_n$  and the number of unoccupied surface states per unit surface area  $S$ . The second term describes the photogeneration of free electrons and the third term describes the thermal generation rate of free electrons.

The steady state condition for Eq. 3.3 yields an expression for the depletion layer barrier  $V$  as a function of the light intensity  $I$ . The only unknown parameter in this expression is  $\beta_n S / f_s$ . Fitting the results presented in Fig. 3.7 with the expression for  $V(I)$  (obtained from Eq. 3.3) we obtain  $\beta_n S / f_s = 2 \pm 1 \text{ cm}^2 \text{ s}^{-1}$ .

We now consider the time dependence of the potential difference over the depletion layer. Immediately after the illumination is switched on, the first and third terms on the righthand side of Eq. 3.3 still counterbalance each other; the rate of change  $\frac{dN}{dt}$  of the number of free electrons in a GaP particle is completely determined by the photogeneration term (second term). For small variations in  $N$  we can develop the depletion layer voltage  $V$  around its value in the dark to obtain

$$\frac{\Delta V}{\Delta t}|_{V \simeq V_{dark}} = \frac{\Delta V}{\Delta R_c} \frac{\Delta R_c}{\Delta N} \frac{\Delta N}{\Delta t} = \frac{\Delta V}{\Delta R_c} \frac{\Delta R_c}{\Delta N} \frac{4}{3} \pi R^3 \alpha I f_s; \quad (3.4)$$

Thus the initial change in the depletion layer barrier per unit time is linear in the intensity of the illumination.

By fitting Eq. 3.4 to the experimental results (see insert of Fig. 3.8)) we obtain  $f_s = 0.5 \pm 0.1$ . Combining this result with the value for  $\beta_n S / f_s$  we obtain  $\beta_n S = 1 \pm 0.5$  cm/s. In order to estimate the capture rate constant  $\beta_n$ , we assume a reasonable density of surface states  $S = 10^{12} \text{cm}^{-2}$ . For this value of  $S$  we obtain an electron capture constant  $\beta_n = 10^{-12} \text{cm}^3/\text{s}$ . This value of the capture rate constant corresponds to a capture cross section  $\beta_n / (\text{thermal velocity}) \simeq 10^{-20} \text{cm}^2$  which is orders of magnitude smaller than the geometrical cross section of an atomic like center ( $10^{-15} \text{cm}^2$ ). Similar results for the electron-capture cross section have been reported for InP crystals, while GaAs crystals show even lower values for the electron capture cross section[30].

### 3.6 Electron-hole recombination time resolved

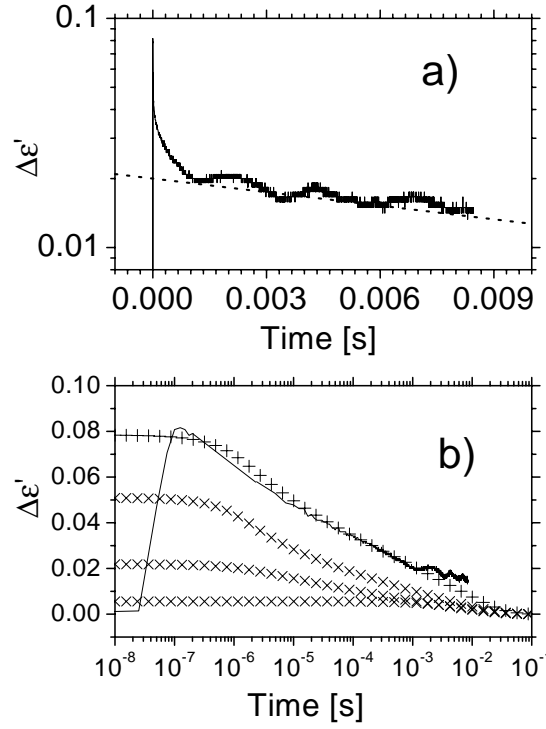


**Figure 3.9:** The change in the real part  $\epsilon'$  of the dielectric constant of porous GaP upon illumination with a laser pulse (wavelength  $\lambda = 500$  nm, pulse energy 7 mJ), as measured with the Time Resolved Microwave Conductivity method. The decay is presented on a) a logarithmic to linear and b) a linear to logarithmic scale to show the non-exponential decay over a wide range of time scales. The dotted line in a) corresponds to a mono-exponential decay with a time constant  $\tau = 0.02$  s. The rise time of the signal ( $\simeq 20$  ns) is determined by the cavity response time. Figure b) also shows a fit calculated with the hydrodynamic model (for the parameters, see text). The radius of the conductive part  $R_c(t)$  as a function of time is obtained from our recombination model with  $\beta_n S = 0.6$  cm/s, and  $R_c(\text{dark}) = 35$  nm. The fit (+) is a linear combination of contributions (x) with  $R_c(t = 0) = 75$  nm (9% of GaP volume),  $R_c(t = 0) = 65$  nm (5%), and  $R_c(t = 0) = 40$  nm (14%).

Here we consider the electron-hole recombination in macroporous GaP upon illumination with a laser pulse. Fig. 3.9 shows the change in the real part  $\epsilon'$  of the dielectric constant of porous GaP upon illumination with a laser pulse, as measured with the Time Resolved Microwave Conductivity method (see chapter 2). The decay is presented on a) a logarithmic to linear and b) a linear to logarithmic scale to show the non-exponential decay over a wide range of time scales.

The electron-hole recombination at the surface and in the bulk is described with the model presented in the previous section. Upon illumination with a laser pulse, trapping of holes at the surface, which reduces the depletion layer, occurs on a time scale of  $10^{-11}$  s (see previous section) and is not detected by our method. Trapping of electrons at the surface, which increases the depletion layer, is more slowly since the electrons have to overcome the depletion barrier. The radius of the conductive core  $R_c$  as a function of time is calculated with Eq. 3.3. The adjustable parameters in this expression are  $\beta_n S$ , the capture rate for free electrons in surface states,  $R_c(t=0)$ , the maximal radius of the conductive core, immediately after the laser pulse hit the semiconducting sphere and  $R_c(\text{dark})$  the radius of the conductive core in the dark (i.e.  $R_c(t = +\infty)$ ). Figure 3.10 shows the

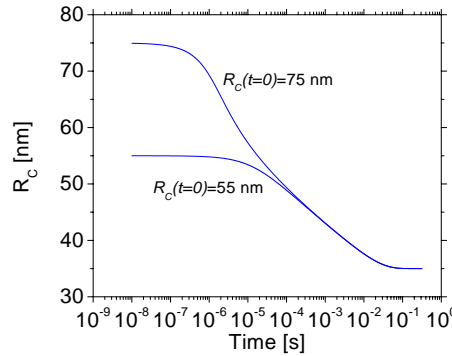


**Figure 3.10:** The transients of the radius of the conductive core  $R_c$  calculated with our recombination model, are shown for different values of  $R_c(t = 0)$  ( $\beta_n S = 0.6$  cm/s and  $R_c(\text{dark}) = 35$  nm).

decay of the radius  $R_c(t)$  as a function of time, calculated with our recombination model for different values of  $R_c(t = 0)$ . This figure shows that the radius of the conductive core at  $t = 0$  strongly affects the time delay after which the decay in the radius  $R_c$  effectively starts. Figure 3.11 shows the decay of the real part of the dielectric constant of macroporous GaP  $\epsilon'$ , calculated with the hydrodynamic



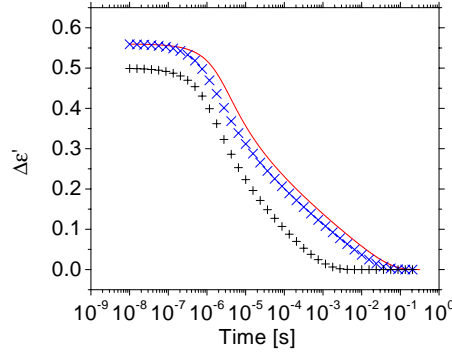


**Figure 3.11:** The change in the real part of the dielectric constant of macroporous GaP  $\epsilon'$  calculated with the hydrodynamic model (for parameters, see text). The radius of the conductive part  $R_c$  as a function of time is calculated with our recombination model for  $\beta_n S = 0.6$  cm/s,  $R_c(\text{dark}) = 35$  nm and  $R_c(t = 0) = 75$  nm ( $\times$ ). To test the sensitivity of our model in  $\beta_n S$  and  $R_c(\text{dark})$ , we also plot the results for  $\beta_n S = 0.3$  cm/s (solid line) and  $R_c(\text{dark}) = 45$  nm (+).

model and our recombination model. From this figure it is clear that an increase in  $R_c(\text{dark})$  as well as an increase in the electron capture rate  $\beta_n S$  reduces the time to reach equilibrium. A fit of the time dependence and the *magnitude* of the real part  $\epsilon'$  of macroporous GaP under illumination with a laser pulse (see Fig. 3.9) is obtained with the same value for the electron mobility  $\mu (= 3 \text{ cm}^2/\text{Vs})$  as obtained from the measurements under constant illumination (see previous section). The values for  $\beta_n S = 0.6 \pm 0.3$  cm/s and  $R_c(\text{dark}) = 35 \pm 5$  nm we find here, are in agreement with the values obtained from experiments under constant illumination ( $\beta_n S = 1 \pm 0.5$  cm/s and  $R_c(\text{dark}) = 45 \pm 5$  nm).

The fit values for  $R_c(t = 0)$  (see Fig. 3.9) show that  $9 \pm 4\%$  of the volume of the GaP sample reaches flat band (i.e. depletion voltage  $V = 0$ ) immediately after the pulse hit the sample. The condition for a semiconducting sphere surrounded by a depletion layer to reach flat band under excitation by a laser pulse is that the number of photogenerated holes that are trapped at the surface equals the number of electrons trapped at the surface in the dark at  $t = +\infty$  (= the number of electron-donors in the depletion layer in the dark at  $t = +\infty$ ). The number of electron-donors in the depletion layer in the dark per unit volume is given by  $(1 - (R_c(\text{dark})/R)^3) \cdot f \cdot n (= 6.10^{16} \text{ cm}^{-3})$  where  $n$  equals the doping density and  $f$  the volume fraction of crystalline GaP in the sample. For a laser intensity of

$10^{16}$  photons per pulse per  $\text{cm}^2$ , and an absorption length  $\alpha^{-1} = 2 \cdot 10^{-6} \text{m}$  [2], we obtain that flat-band is obtained upto  $14 \mu\text{m}$  into the sample. For a sample diameter of  $600 \mu\text{m}$ , this corresponds to a depleted volume of about 4 % of the volume, in agreement with the value obtained from the fit of  $\Delta\epsilon'$ .

In summary, we have shown that the electron-hole pairs photogenerated in a porous GaP network recombine in the bulk as well as at the internal surface. Upon illumination, the surface barrier for the electrons is reduced as the width of the depleted region shrinks. After switching off the illumination the depleted region is gradually restored and the surface barrier for electron recombination rises accordingly. The increase in the surface barrier for the photogenerated electrons forms the main reason for the increasingly slower electron-hole recombination rate after turning off photoexcitation.

### 3.7 Conclusions

The complex dielectric constant of macroporous GaP  $\epsilon$  and the transients of its change  $\Delta\epsilon$  under constant illumination and by excitation with a laser pulse, obtained from Time Resolved Microwave Conductivity measurements, can be quantitatively understood from a model that describes the porous network as a collection of non-depleted spheres surrounded by a depleted region. The polarizability of these spheres is described with the hydrodynamic model. Electron-hole pairs photogenerated in the porous network recombine in the bulk as well as at the internal surface. Trapping of holes at the surface, which occurs on a time scale faster than our method ( $10^{-8}$  s), reduces the depleted region upon illumination. After illumination, the depletion layer restores by electron surface recombination across the depletion barrier. The increase in the depletion barrier for the photogenerated electrons forms the main reason for the increasingly slower electron-hole recombination at the surface. The electron mobility inside the non-depleted core, which is accurately obtained from the fitting of the ratio  $\Delta\epsilon'/\Delta\epsilon''$ , is smaller than the mobility in bulk GaP, and orders of magnitude larger than the long-range mobility in macroporous GaP.



## References

---

- [1] J. J. Kelly and D. Vanmaekelbergh, *Electrochim. Acta* **43**, 2773 (1998).
- [2] F. Schuurmans, D. Vanmaekelbergh, J. van de Lagemaat, A. Lagendijk, *Science* **284**, 5411 (1999).
- [3] B. Erne, D. Vanmaekelbergh, and J. Kelly, *J. Electrochim. Soc.* **143**, 305 (1996).
- [4] B. O'Regan and M. Gratzel, *Nature* **353**, 737 (1991).
- [5] U. Bach, D. Lupo, P. Comte, J. Moser, F. Weissortel, J. Salbeck, H. Spreitzer, M. Gratzel, *Nature* **395**, 583 (1998).
- [6] M. Gratzel, *Nature* **409**, 575 (2001).
- [7] D. Cummins, G. Boschloo, M. Ryan, D. Corr, S. Nagaraja Rao, D. Fitzmaurice, *J. Phys. Chem. B* **104**, 11449 (2000).
- [8] H. Weller, *Adv. Mater.* **5**, 88 (1993).
- [9] R. Konenkamp, *Phys. Rev. B* **61**, 11057 (2000).
- [10] H. Scher, M. F. Shlesinger, and J. T. Bendler, *Physics Today* **44**, 26 (1991).
- [11] L. Dloczik, O. Ileperuma, I. Lauermann, L. Peter, E. Ponomarev, G. Redmond, N. Shaw, I. Uhlendorf, *J. Phys. Chem. B* **101**, 10281 (1997).
- [12] A. L. Roest, P. E. de Jongh, and D. Vanmaekelbergh, *Phys. Rev. B: Condens. Matter Mater. Phys.* **62**, 16926 (2000).
- [13] D. Vanmaekelbergh and P. E. de Jongh, *Phys. Rev. B* **61**, 4699 (2000).
- [14] J. van de Lagemaat and A. J. Frank, *J. Phys. Chem. B* **104**, 4292 (2000).
- [15] R. J. Deri and J. P. Spoonhower, *Phys. Rev. B* **25**, 2821 (1982).
- [16] S. Y. Grabtchak and M. Cocivera, *Phys. Rev. B* **50**, 18219 (1994).
- [17] E. van Faassen, *Phys. Rev. B* **58**, 15729 (1998).
- [18] D. Vanmaekelbergh, B. Ern , C. Cheung and R. Tjerkstra, *Electrochim. Acta*, **40**, 689-698 (1995).
- [19] F. Schuurmans, D. Vanmaekelbergh, J. van de Lagemaat, A. Lagendijk, *Science* **284**, 5411 (1999).
- [20] B. Ern , D. Vanmaekelbergh, J. Kelly, *J. Electrochem. Soc.* **143**, 305 (1996).
- [21] M. Sucher and J. Fox, *Handbook of Microwave Measurements*, Polytechnic Press, 1963.
- [22] N. Marcuvitz, *Waveguide Handbook 10*, Mc Graw-Hill, 1951.
- [23] S.J. Fonash, *Solar Cell Device Physics*, Academic Press, 1981.
- [24] M. Sotoodeh, A. Khalid and A. Rezazadeh, *J.Appl.Phys.* **87**, 2890 (2000).
- [25] Y. Kao and O. Eknayan, *J.Appl.Phys.* **54**, 2468 (1983).

- [26] K. Chopra, *Thin Film Phenomena*, Mc Graw-Hill (1969).
- [27] J. Jackson, *Classical Electrodynamics*, J. Wiley, 1998.
- [28] B. Erne, D. Vanmaekelbergh and J. Kelly, *Adv. Mater.* **7**, 739 (1995).
- [29] D. Vanmaekelbergh, R. ter Heide and W. Kruijt, *Ber. Bunsenges. Phys. Chem.* **93**, 1103 (1989).
- [30] R. Bube and F. Cardon, *J. Appl. Phys.* **35**, 2712 (1964).

## 4 Optical transitions between the conduction levels of ZnO quantum dots studied by IR absorption spectroscopy

---

### 4.1 Abstract

In this chapter, we report on the optical transitions in few-electron artificial atoms strongly confined in ZnO nanocrystals with diameter between 3 and 6 nm. The artificial atoms are prepared by two methods. The first method uses an assembly of weakly coupled ZnO nanocrystals in which electrons are injected electrochemically; the average electron number is obtained from the injected charge and the number of quantum dots in the assembly. In the second method a colloidal solution of ZnO nanocrystals is used; few-electron artificial atoms are obtained by photogeneration of electron-hole pairs and subsequent hole-scavenging. The charged ZnO nanocrystals show broad spectra in the near IR; the shape and total absorption intensity being determined only by the average electron number. The spectra can be explained by taking into account the allowed electric dipole transitions between the atom-like orbitals of the ZnO nanocrystals and the size distribution of the nanocrystals in the sample.

### 4.2 Introduction

Colloidal insulating nanocrystals should form ideal hosts for strongly-confined artificial atoms, i.e. configurations of one to a few electrons occupying the conduction energy levels of the nanocrystal. Such nanocrystals can be obtained in molar quantities by wet chemical synthesis with increasing control of the size, shape and surface electronic properties [1]-[3]. The dimensions below 10 nm ensure strong quantum-confinement of the electrons corresponding to confinement energies in the 0.1 to 1 eV range. For comparison, artificial atoms defined by lithography in bulk semiconductor crystals have dimensions of a few tens to hundreds of nanometers and, accordingly, show much weaker confinement effects in the 1 meV range [4]. The interest in studying artificial atoms in the strong confinement regime is that quantum confinement, and Coulomb and exchange interactions all depend in a different way on the dimensions of the nanocrystal host

[5]. Thus, in strongly confined systems, as yet unobserved electrical and optical properties should emerge.

A major problem in studying strongly-confined artificial atoms is the fabrication of devices in which the *electron occupation number*  $N$ , i.e. number of electrons per quantum dot, can be controlled. For example, a transistor consisting of a single CdSe quantum dot, mounted between two electrodes, with a gate to control the electron or hole number has been reported [6], [4]. The technological sophistication required for the fabrication of such a device, however, prevents experimental studies by a wide research community. We have fabricated *assemblies* consisting of ZnO nanocrystals of diameter between 3 and 6 nm in which the electron number can be controlled by the electrochemical potential. It has been shown that the electrons occupy the atom-like S and P envelope wavefunctions. In long-range electron transport, two quantum regimes have been observed corresponding to tunneling between the S-orbitals for an electron occupation number lower than two, and tunneling between the P-orbitals for an electron occupation number between two and eight [7].

Here, we report a study of the optical properties of artificial atoms created in such an assembly. We detect the optical transitions between the conduction levels in artificial atoms consisting of one to ten electrons by absorption spectroscopy in the near infra-red. The importance of this work for the physics of strongly-confined systems is two-fold. First, we demonstrate that, by gradually increasing the electron number in the ZnO nanocrystals, the contribution of each individual electronic transition to the absorption spectrum can be identified, despite the size dispersion in the assembly. Until now, only the optical transition between the lowest (S) and second lowest (P) conduction level in CdSe and ZnO quantum dots has been reported. Second, the present method of spectroscopy directly provides the single-particle energy separations between the electron levels. This is due to the fact that electrons are transferred from one conduction level to another (keeping the electron number constant), the repulsion energy between two electrons being nearly independent of the orbitals that they occupy[8]. This is in firm contrast to conventional absorption and luminescence spectroscopies that probe transitions between valence and conduction levels. In the latter case the polarization and the Coulomb-interaction energies of the electron and hole play an important role in the energy of the transition[8] making the extraction of single-particle energies more complex and subject to uncertainties.

In this chapter, we first discuss the single-electron conduction levels in ZnO quantum dots and the optical transitions between these levels. The electron energy levels in ZnO quantum dots are calculated with the most simple effective mass approximation and the elaborate tight-binding method. These orbitals are then used



to calculate the oscillator strengths of the electric dipole transitions between the energy levels. Next we show the IR absorption spectra obtained with an assembly of ZnO quantum dots with an increasing average occupation number. We present a model that calculates the distribution of the electrons over the quantum dots in the assembly for a given electrochemical potential, and their corresponding IR absorption. By fitting this model to the absorption spectra we obtain the relative oscillator strengths of S-P, P-D, P-S' and D-F transitions and single-particle separations between these levels. The oscillator strengths and single-particle energy separations are compared with the predictions from the tight-binding model and the effective mass method.

### 4.3 Single-electron conduction levels in ZnO quantum dots

An electron added to an otherwise neutral ZnO nanocrystal will occupy the conduction state of lowest energy, the Lowest Unoccupied Molecular Orbital (LUMO). This orbital is strongly delocalised. As a consequence, this electron is confined in the limited space of the nanocrystal. The kinetic confinement energy, i.e. the difference in kinetic energy between an electron in a nanocrystal and a bulk crystal, due to confinement of its wave function, can be calculated with a number of methods. In order of increasing sophistication, we have the particle-in-a-box approximation, the quasi-particle-in-a-box (effective mass) approximation [9]-[11] and various tight-binding [12]-[14] and pseudo-potential methods [13], [5]. We use here the quasi-particle-in-a-box approximation to calculate the single-particle kinetic confinement energy levels in a spherical ZnO quantum dot, and compare the results with the outcome of more sophisticated tight-binding calculations. The polarization (i.e. dielectric) confinement energy of an electron in a quantum dot is considered in section 4.6.

In the effective mass approximation, the interaction of a (conduction) electron with a periodic lattice potential (i.e. the scattering with core atoms) is described by replacing the (bare) mass  $m$  of the electron, by an effective mass  $m^*$  (called the mass of the quasi-electron). This approximation holds for a weak periodic potential and small values of the wave vector  $\mathbf{k}$ . To describe the confinement of the electron to the nanocrystal, we assume, as a first approximation, that the quasi-electron potential is constant inside the quantum dot and infinitely high outside the particle. The eigenfunctions of the electron (in spherical coordinates) are a product of the spherical harmonics  $Y_l^m(\theta, \varphi)$ [15], which only depend on the spherical coordinates  $\theta$  and  $\varphi$ , and the spherical Bessel functions  $j_l(k_{l,n}r)$ [15], which only depend on the radial distance  $r$ . With  $l$  we denote the quantum number for the angular momentum,  $m$  is the quantum number for the projection of the angular

momentum and the quantum number  $n$  distinguishes different energy levels with equal angular momentum. The atom-like electron orbitals S, P, D, F, ... have  $l = 0, 1, 2, 3, \dots$ . The orbital with quantum numbers  $l = 0, n = 2$  is denoted with S'. The wavevector  $k_{l,n}$  is determined from the condition that the wavefunction vanishes at the surface, i.e.  $j_l(k_{l,n}R) = 0$  where  $R$  is the radius of the particle. Due to this condition, the energy levels no longer form a continuum; instead we obtain quantized energy levels with discrete wave vectors  $\mathbf{k}$ . Figure 4.1 shows the square of the modulus of the S and P eigenfunctions, which corresponds to the probability of finding an electron as a function of its position.

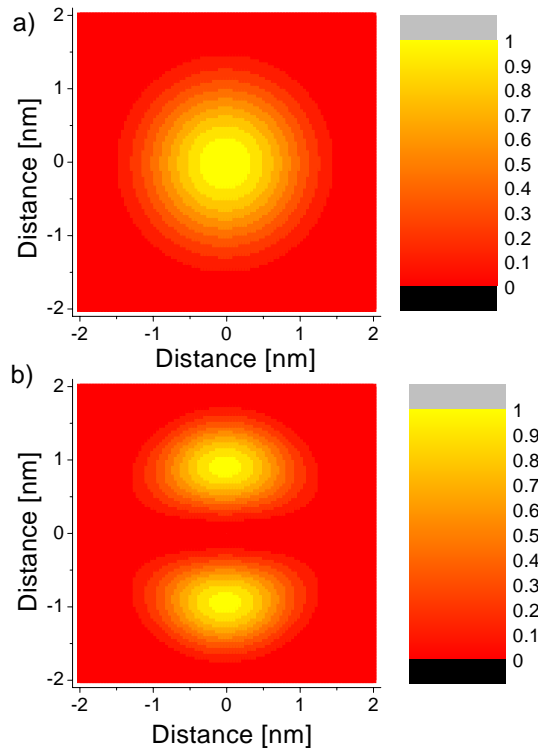


**Figure 4.1:** The square of the wavefunctions with quantum numbers a)  $n = 1, l = 0$  (S, LUMO) and b)  $n = 1, l = 1$  (P), calculated with the effective mass approximation for a spherical ZnO quantum dot (4 nm in diameter) as a function of the position in the quantum dot.

The energy levels of the eigenfunctions are given by [15]

$$\varepsilon_{l,n} = \frac{\hbar^2 k_{l,n}^2}{2m^*} \quad (4.1)$$

for an electron with an effective mass  $m^*$ . From this expression and the boundary condition  $j_l(k_{l,n}R) = 0$ , we obtain that the kinetic confinement energy of the electron depends on the radius  $R$  of the quantum dot as  $1/R^2$ , and is inversely proportional to the effective mass. Figure 4.2 shows the kinetic confinement

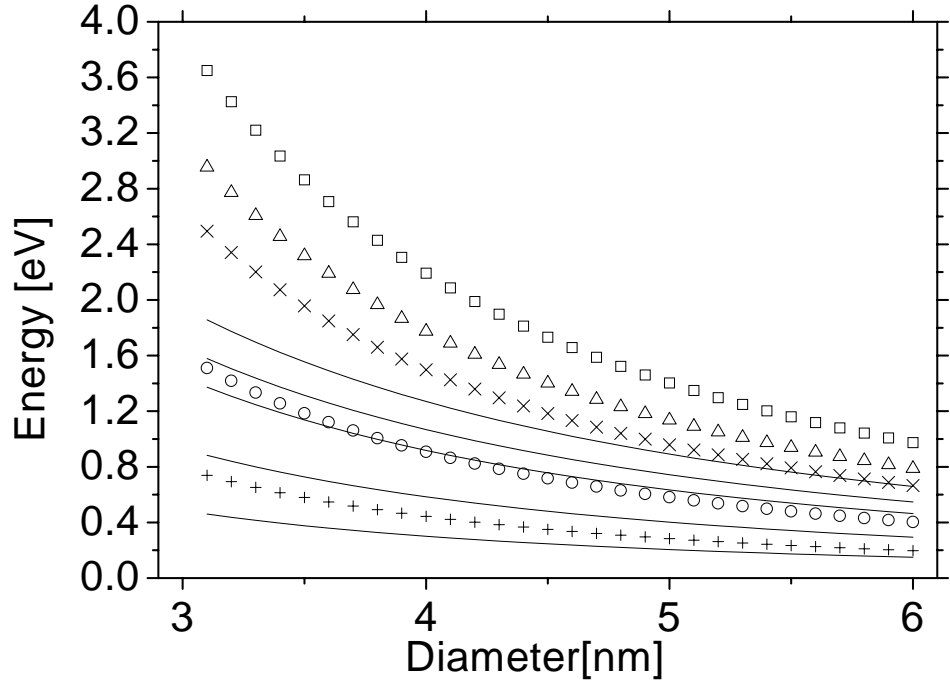


**Figure 4.2:** The kinetic confinement energy of the lowest conduction levels of a ZnO quantum dot, as a function of the diameter of the quantum dot. The solid lines are calculated with the tight-binding model (from bottom to top; S, P, D, S', F), the symbols are the predictions from the effective mass approximation; S (+), P (o), D (x), S' (Δ) and F (□).

energy of the lowest conduction levels, obtained with the effective mass approximation, as a function of the diameter of the ZnO quantum dot. With an electron

effective mass equal to the bulk electron effective mass ( $m^* = 0.2m$  [16]), the kinetic confinement energy of the lowest energy level is of the order of 400 meV for a quantum dot with a diameter of 4 nm. In order of increasing energy we find a S, P, D, S' and F levels. The degeneracy (including spin states) of an energy level  $l$  is given by  $2(2l + 1)$ .

A more accurate description of the confinement of the electron to a quantum dot is based on the assumption that the potential barrier is finite. The tunneling decay length  $r_t$  is given by [15]

$$r_t = \frac{\hbar}{\sqrt{2m(E_{vac} - E)}}, \quad (4.2)$$

in which  $E_{vac}$  is the energy of the electron at rest in vacuum and  $E$  is the energy of the electron in a given conduction energy level. With a typical value  $E_{vac} - E$  of 4 eV [16], the decay length is 1 nm. Because the kinetic confinement energy strongly depends on the volume in which the electron is confined, carrier penetration outside the crystallite reduces the energy of the electron considerably.

Because the effective mass approximation holds only for small kinetic energy values (such that the kinetic energy is quadratic in the wave vector  $k$ ), smaller quantum dots are described less accurately by the effective mass approximation. Advances in computational physics have enabled the direct solution of the single electron Schrodinger equation for larger quantum dots [14]. The Hamiltonian of the electron in this system accounts for the interaction of the electron with the atoms of the nanocrystal and the surroundings of the quantum dot. However, to find solutions of the Schrodinger equation, approximations are necessary and the success of a method depends on the choice of the approximations. Two methods frequently used are the pseudopotential method and the tight-binding theory. The use of the pseudopotential method to calculate the energy levels in insulating nanocrystals has been advocated by Zunger and coworkers [17]-[20]. Here, we will consider the elaborate tight-binding model to calculate the conduction levels in ZnO quantum dots, results obtained from a collaboration with the group of Dr. Allan and Dr. Delerue (IEMN, Lille).

In the tight-binding model, one assumes that the dot-wavefunctions are built up from a relatively small number of localized atomic wavefunctions. In this approximation we exclude the delocalized (=ionized) atomic wavefunctions. Here we describe a tight-binding approximation [21] built up from the Zn and O atomic wave functions s, p, d and  $s^*$  (including spin-orbit coupling). One assumes that the electron can be described by a single-particle Hamiltonian and that this single-particle Hamiltonian inside the quantum dot equals the bulk single-particle Hamiltonian. This means that the scattering of the electrons by the lattice is assumed

to be the same as in a bulk crystal. The tight-binding parameters are fitted to the bulk ab-initio pseudopotential energy dispersion curve and the experimental electron and hole effective masses. Advantage of this semi-empirical approach is that only a relevant selection of wavefunctions needs to be calculated; this enables one to perform calculations for a large quantum dot (up to 15 nm). Dangling bonds at the surface are saturated by pseudo-hydrogen atoms. Fig. 4.2 shows the kinetic confinement energy of the lowest conduction levels of a ZnO quantum dot. The lowest conduction level of a ZnO quantum dot has S-symmetry and is doubly degenerate. In order of increasing energy we further have a P-level (six-fold degenerate), a D-level (ten-fold degenerate), a S' level (doubly degenerate), and a F-level (fourteen-fold degenerate). From Fig. 4.2 it is clear that the size-dependence of the kinetic confinement energy calculated with tight-binding theory is less strong than that calculated with the effective mass approximation ( $1/R^2$ ). Furthermore, the relative difference between tight-binding theory and effective mass approximation is larger for higher values of energy. For quantum dots with a diameter of 6 nm for instance, the difference between tight-binding and effective mass is only 30 % for the S level and already 50 % for the F level. The different results here are mainly due to the infinite energy barrier used in the effective mass approximation.

Fig. 4.3 shows the square of the S and P wavefunctions in a ZnO quantum dot as a function of the position, obtained with the tight-binding model. The wavefunctions obtained with the tight-binding method show the periodicity of the lattice. A detailed comparison between Fig. 4.1 and Fig. 4.3, shows that the tight-binding orbitals decay more slowly from the center towards the crystal surface than the orbitals obtained with the effective mass approximation with infinite walls.

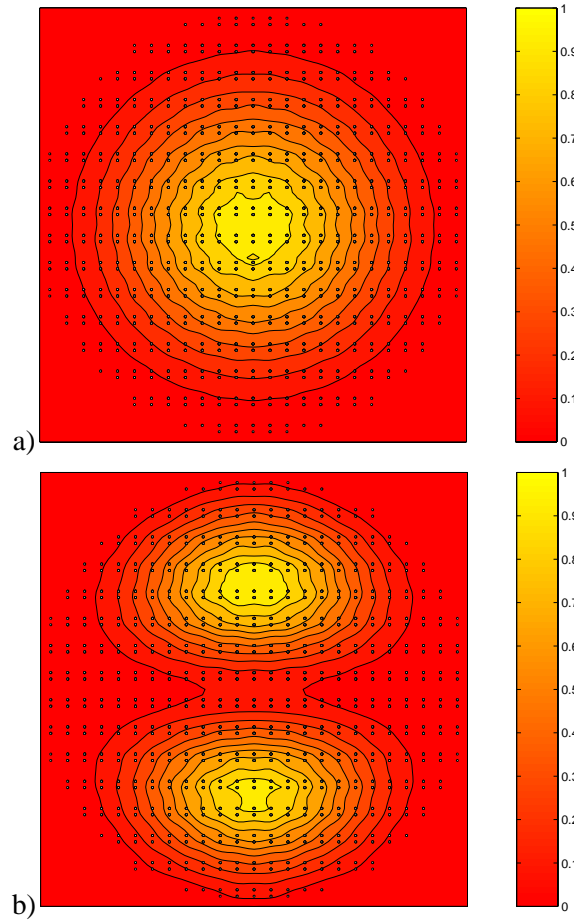


**Figure 4.3:** The square of the S wavefunction ( $n = 1, l = 0$ ) a) and P wavefunction ( $n = 1, l = 1$ ) b), of a nearly spherical ZnO quantum dot (4.2 nm in diameter) calculated with the tight-binding model as a function of the position. The atoms of the ZnO nanocrystal are indicated with points; note the crystal facets.

## 4.4 Optical transitions between the conduction levels in ZnO quantum dots

### 4.4.1 Electric dipole transitions in a one-electron dot and oscillator strengths

We investigate the electric dipole absorption rate (i.e. the amount of energy absorbed per unit time which equals the transition probability per unit time multiplied by the photon energy)  $A_{it}$ , by one quantum dot that contains one electron, due to a transition between the electron states  $i$  and  $t$ . This rate is proportional to the incident energy intensity per unit frequency  $j(E_t - E_i)$  (i.e. the photon flux per unit frequency times the photon energy). With  $E_i(E_t)$ , we denote the energy of the electron in the initial (final) state. This absorption rate (with the dimension of energy per unit time) is given by<sup>1</sup> (Fermi's golden rule) [15]:

$$A_{it} = \frac{\pi e^2}{2mc\epsilon_0} f_{it} j(E_t - E_i), \quad (4.3)$$

where  $m$  is the mass of the electron,  $c$  the speed of light and  $\epsilon_0$  the permittivity of vacuum. In this expression  $f_{it}$  denotes the dimensionless oscillator strength between the electron states  $i$  and  $t$ , defined as

$$f_{it} = \frac{2m}{\hbar^2} (E_t - E_i) |\langle i|z|t \rangle|^2. \quad (4.4)$$

The matrix element of the  $z$  coordinate of the dipole operator is represented by  $e\langle i|z|t \rangle$ . In order to compare the oscillator strength calculated with the tight-binding model and the effective mass approximation, we use the bare mass of the electron in Eq. 4.3 and 4.4. An interesting feature of the oscillator strength is that its sum over a complete set of (normalized) basis states  $t$  (without spin states) equals one<sup>2</sup>, i.e.

$$\sum_t f_{it} = 1. \quad (4.6)$$

<sup>1</sup>The absorption rate  $A_{it}$  is averaged over the polarization directions of incident radiation.

<sup>2</sup>This sum rule holds for a Hamiltonian that contains the momentum operator only in the kinetic energy operator. A complete set of electron basis states is a collection of states  $t$  such that every possible electron state can be written as a unique linear combination of these basis states. For example, the collection of states with the set of quantum numbers  $(n, l, m_l)$  (see section 4.3) is a complete set of electron basis states in the effective mass model. We remark that all these states have an energy larger than the S level. In the calculation of  $f_{it}$  with the effective mass model, we took the bare mass of the electron  $m$  in the definition of the oscillator strength (Eq. 4.4) but the effective mass  $m^*$  in the Hamiltonian to calculate the eigenfunctions, and the sum rule therefore

This property can be used to check if all allowed transitions have been accounted for.

From IR absorption measurements we obtain the transition rate between two *energy levels*, not between two *electron states*. We therefore must calculate the *average* absorption rate  $\bar{A}_{ll'}$  for one quantum dot that contains one electron, due to transitions between the *energy levels*  $E_l$  and  $E_{l'}$ . We assume that every energy level  $E_l$  contains  $2(2l + 1)$  electron states (including spin states). Under this assumption

$$\bar{A}_{ll'} = \frac{1}{2(2l + 1)} \sum_i \sum_t A_{it}. \quad (4.7)$$

where the sum runs over all states  $i$  with energy  $E_l$  and all states  $t$  with energy  $E_{l'}$ ;  $A_{it}$  is given by Eq. 4.3.

For an electron with a spherically symmetric Hamiltonian, the electric dipole transition rules are  $\Delta l = \pm 1, \Delta j = 0, \pm 1$  and  $\Delta m_j = 0, \pm 1$  [22]. With  $j$  we denote the quantum number for the total angular momentum (spin + orbit) and  $m_j$ , the quantum number for its projection. In other words, the matrix element  $\langle i|z|f \rangle$  is non zero only for the transitions between states with  $\Delta l = \pm 1, \Delta j = 0, \pm 1$  and  $\Delta m_j = 0, \pm 1$ . If spin-dependent interactions are negligible, the spin is conserved and the transition rules become  $\Delta l = \pm 1, \Delta j = \pm 1$  and  $\Delta m_l = 0, \pm 1$ . Figure 4.4 shows the allowed transitions between the orbitals corresponding to the S, P and D levels. In the effective mass approximation, which possesses full rotational symmetry, the oscillator strengths of forbidden transitions are zero. Although the tight-binding model has no full rotational symmetry, the oscillator strengths of forbidden transitions are orders of magnitude smaller than the allowed transitions. The selection rules for transitions in our quantum dots are thus determined by the symmetry of the envelope wave functions.

Analogous to the absorption rate, the average oscillator strength due to transitions between the energy level  $E_l$  and  $E_{l'}$  is given by

$$\bar{f}_{ll'} = \frac{1}{2(2l + 1)} \sum_i \sum_t f_{it}, \quad (4.8)$$

becomes

$$\sum_t f_{it} = \frac{m}{m^*} = 5.0. \quad (4.5)$$

In the tight-binding model, a set of basis states not only contains conduction states and free states but also valence states, with an energy smaller than the S conduction level. Because spin-orbit coupling is only a slight perturbation (meV) the sum rule holds to a good approximation for our tight-binding model.



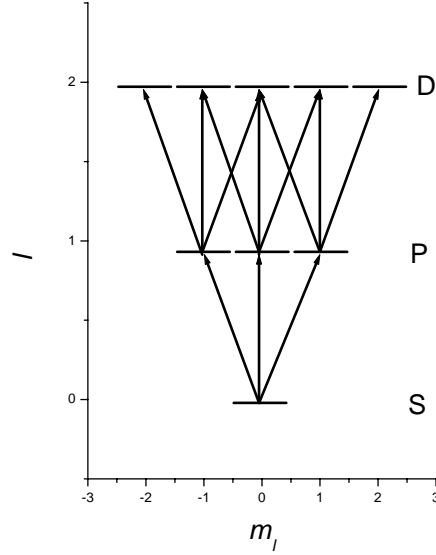


**Figure 4.4:** The allowed transitions between the S, P and D conduction levels in a spherical quantum dot between electron states with orbit angular momentum quantum number  $l$  and projection of the angular momentum quantum number  $m_l$ .

where the sum runs over all states  $i$  ( $t$ ) with energy  $E_i$  ( $E_t$ ). Figure 4.5 shows the summed oscillator strength  $2(2l + 1)\bar{f}_{ll'}$  for the allowed transitions between the lowest energy levels in a spherical ZnO quantum dot<sup>3</sup>. We take the S-P transition as an example. From the sum rule we obtain that in the effective mass approximation (see Eq. 4.5)  $\sum_i \sum_t f_{it} = 10.0$ , where the sum on  $i$  runs over the spin states  $m_s = \pm 1/2$  and the sum on  $t$  runs over a complete set of basis states in the effective mass model. From Fig. 4.5 it is clear that  $2\bar{f}_{SP}$  is slightly less than 10. Since in the effective mass model all electron states have an energy larger than the energy of the S level, this shows that the transition probability for S to P', P'', etc. is much smaller than for S to P. For the tight-binding model,  $\sum_i \sum_t f_{it} \simeq 2$ ,

<sup>3</sup>A polarisation term (see section 4.6.1) is not taken into account. Because the polarisation energy  $\Sigma_l$  of an electron in our dots, depends only slightly (of the order of meV) on  $l$  ( $=$  S,P) [19], we assume that a polarisation term will only slightly disturb the oscillator strengths we obtain here.

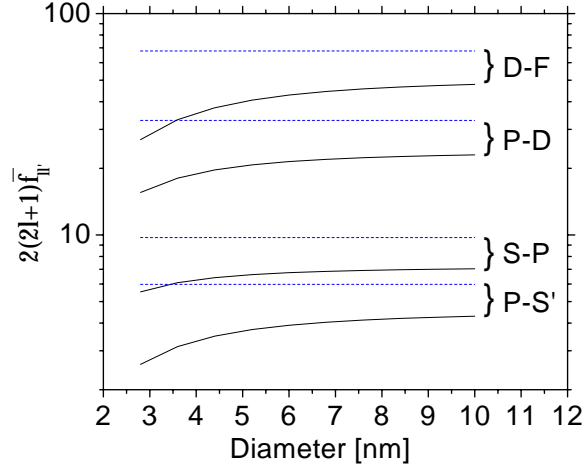


**Figure 4.5:** The summed oscillator strength  $2(2l + 1) \bar{f}_{W'}$  for different allowed transitions is shown as a function of the diameter of the ZnO quantum dot. The values obtained by tight-binding theory (including spin-orbit coupling) are represented as solid lines, the values obtained by the effective mass approximation (no spin interaction accounted for) are represented by a dotted line. To compare values obtained by both methods, the bare mass of the electron is used in the definition of the oscillator strength. The matrix element  $\langle i|z|t \rangle$  in Eq. 4.4 is calculated numerically.

where the sum on  $i$  runs over the spin states  $m_s = \pm 1/2$ , and the sum on  $t$  runs over a complete set of basis states in the tight-binding model (including valence states). Here we find that in the tight-binding model  $2\bar{f}_{SP} \simeq 7$ . This value should be compared with the value slightly smaller than 10 obtained with the effective mass model. Summation of the oscillator strength over a complete set of basis states (including valence states with an energy smaller than the S level), would reduce the sum to a value of about 2. We remark that the average oscillator strength  $\bar{f}_{W'}$  is of the order of 4 for the S-P transition, as well as the P-D and D-F transition. The difference in the oscillator strengths for the tight-binding theory and effective mass approximation is essentially due to the difference in the energy separation ( $E_t - E_i$ ) of the two models; the difference in the matrix element  $\langle i|z|t \rangle$  between both models is less than 10 %. The value of the matrix element of the electric dipole operator is merely determined by the envelope wavefunctions and not by the atomic details (for instance the surface termination). It will become

clear in the following sections that the selection rules and the calculated oscillator strengths are of importance to understand the absorption spectra of few electron artificial atoms.

#### 4.4.2 Transitions in a dot containing more than one electron

We now consider the absorption rate by one quantum dot with more than one electron, due to transitions between the energy levels  $E_l$  and  $E_{l'}$ . We assume that the energy level  $E_l(E_{l'})$  contains  $N_l(N_{l'})$  electrons ( $N = N_l + N_{l'}$ ). Because the transition probability per quantum dot per photon is much smaller than one ( $\simeq 10^{-15}$  see section 4.5.2), and in the approximation that the absorption rate is independent of spectator electrons<sup>4</sup>, the absorption rate of a quantum dot with two electrons, due to a transition from electron state  $i$  to  $f$  or a transition from state  $\bar{i}$  to  $\bar{f}$  equals  $A_{if} + A_{i'f'}$ . Under these assumptions the average absorption rate by one quantum dot due to transitions between the energy levels  $E_l$  and  $E_{l'}$ ,  $\bar{A}_{ll'}^N$  is given by:

$$\begin{aligned}\bar{A}_{ll'}^N &= N_l \bar{A}_{ll'} \text{ if } N_l \leq 2(2l + 1), \\ &= 2(2l + 1) \bar{A}_{ll'} \left(1 - \frac{N_{l'}}{2(2l' + 1)}\right) \text{ if } N_{l'} > 0.\end{aligned}$$

For example, the average absorption by a quantum dot with three electrons (configuration  $S^2P^1$ ), due to a transition between the S and P level equals  $2\bar{A}_{SP}(1 - 1/6)$ .

### 4.5 IR absorption spectra obtained with an assembly of ZnO quantum dots

#### 4.5.1 Experimental method

In the IR absorption measurements we use nearly monodisperse ZnO quantum dots without capping, with diameters in the 3-6 nm range [23]. ZnO nanoparticles are prepared by addition of LiOH to an ethanolic zinc acetate solution [23]. Ag- ing of particles is governed by temperature, the water content, and the presence

<sup>4</sup>Spectator electrons with an energy  $E_{l'}$  occupy states that cannot be occupied by an electron that makes a transition to this energy level. Obviously, we take this into account. Here we mean the influence of spectator electrons on the absorption rate beside this Pauli-effect. Because the Coulomb interaction  $J_{l,l'}$  between electrons depends only by a few meV on the quantum number  $l, l'$  (=S, P) [19], we assume that spectator electrons only slightly disturb the absorption rate. Exchange interaction is about an order of magnitude smaller than the Coulomb interaction [19] and we neglect it in the rest of this chapter.

of reaction products. Water and acetate induce considerably accelerated particle growth. Growth can almost be stopped by removal of these species ('washing'). The average diameter of the nanocrystals is determined with XRD. The IR absorption measurements on an assembly of ZnO quantum dots are performed with a two-electrode electrochemical cell schematically shown in Figure 4.6. A film of

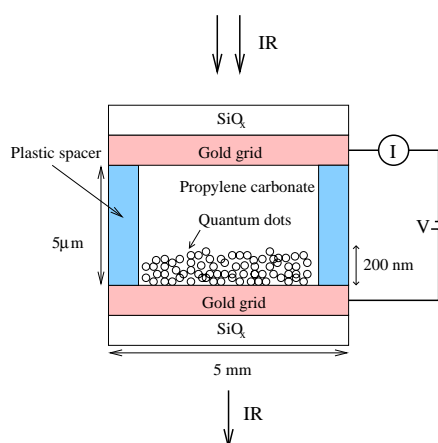


**Figure 4.6:** Schematic drawing of the two-electrode electrochemical cell used in IR absorption measurements on an assembly of ZnO quantum dots.

ZnO quantum dots, about 200 nm thick, is deposited by spin-coating a 'washed' colloidal suspension on a gold/glass substrate. Annealing of the layer by heating it to 90° C for 15 minutes removes residual alcohol from the layer. IR transparent contacts consist of a gold grid (with a distance of 10 μm between the gold lines). A negative voltage  $V$  between the work electrode (with the ZnO layer) and a counter electrode, leads to an increase in the electrochemical potential  $\mu$  of the ZnO quantum dot assembly, which becomes populated with electrons. Because of the presence of positive ions in the electrolyte solution (propylene carbonate with 0.2M LiClO<sub>4</sub>) in the pores of the film, the electric field due to electrons in the quantum dots is screened. As a result, the electron number in the quantum dots

can be quite high (up to 10 electrons) and the electrons are distributed uniformly over all ZnO nanocrystals in the film. By measuring the current  $I$  between work and counter electrodes, during the discharge of the electrode, no contribution from reduction (e.g. of water) is observed; all charge that flows from the work electrode was stored in the ZnO layer. The number of electrons stored in the ZnO layer is measured by integrating the current  $I$  that flows between work and counter electrode. The average electron occupation number  $\langle N \rangle$  of a quantum dot is obtained from the total number of electrons in combination with the number of quantum dots in the layer. The latter is calculated from the amount of zinc, determined with the elemental analysis technique ICP-OES, and the size of the nanocrystals. At a voltage of -3V between the electrode with the quantum dots and the counter electrode reduction of the ZnO film starts. This limits the charging to a maximum of 15 electrons per quantum dot, 5.2 nm in diameter and to only 3 electrons if the diameter is 3.7 nm. Because of IR absorption by the electrolyte, the width of the electrolyte layer should be as small as possible. We have used cells where the optical path through the electrolyte solution is only 5  $\mu\text{m}$ . We therefore have no place for a reference electrode, which means that we cannot measure the electrochemical potential  $\mu$  of the ZnO layer. All IR absorption measurements are performed with a Bio-rad FTIR<sup>5</sup> spectrometer FTS-40, at room temperature in a nitrogen purged environment.

---

<sup>5</sup>In a FTIR spectrometer, the IR path is modulated by an oscillating mirror such that every IR frequency appears in the probing IR beam with a given time period. By a Fourier transform of the time-dependent detector signal, the intensity of the detected IR beam is obtained as a function of the IR frequency. The IR absorption spectrum of a sample is obtained from the IR spectrum measured with the sample in the IR beam and the IR spectrum measured before or after the sample is in the beam. The advantage of this FTIR method is that a whole frequency range is obtained in about one second, the disadvantage is a time resolution larger than one second.

### 4.5.2 Results

Figure 4.7 shows the increase in the absorption (i.e. the fraction of the incident intensity which is absorbed) of an assembly of ZnO quantum dots (the average diameter is 4.2 nm in a) and 3.7 nm in b)) due to charging with on average  $\langle N \rangle$  electrons per quantum dot. The corresponding voltage  $V$  between the electrode with the quantum dots and the counter electrode is also indicated. The charging of the electrode takes a few seconds. The change in the IR absorption is instantaneous with the charging of the electrode. The dips in the absorption spectrum at 3000, 1800, 1300, and 1100  $\text{cm}^{-1}$  are also found in the absorption spectrum of the propylene carbonate electrolyte. We therefore conclude that these dips are due to a decrease in the absorption of propylene carbonate, induced by charged quantum dots. The precise mechanism behind these sharp features is not understood. The assembly can reversibly store up to seven electrons per quantum dot without chemical degradation [24]. The energy of the absorbed photons is in the range of a few 100 meV, which corresponds to the energy difference between the conduction levels in ZnO quantum dots in the 3 to 6 nm range (see section 4.3). The width of the absorption peak ( $\simeq 50\%$  of peak position), is essentially due to the size distribution. Indeed, the spectra obtained at cryogenic temperatures show the same width. From Fig. 4.7 it is clear that for increasing occupation number  $\langle N \rangle$ , the absorption and the width of the absorption peak increase while the position of the absorption peak shifts to higher energies. This strongly suggests that several different optical transitions become possible when  $\langle N \rangle$  increases. From a comparison between the spectra shown in Fig. 4.7 a) and b), it is clear that the absorption peak is at larger energy for the smaller quantum dots. This is a clear manifestation of the size confinement of the energy levels. Fig. 4.7b) shows that the absorption spectra obtained at two different samples are nearly identical; the reproducibility is of the order of a few percent. The reproducibility in the measurement of the charge for two different samples is better than 10% for voltages  $V$  smaller than -3 V.

The IR absorption due to charging of the S-level of a ZnO assembly (average diameter 5 nm) is about 10 % of the incident flux. The IR intensity throughout the sample is thus about constant. From the absorption due to charging, in combination with the incident IR photon flux of  $10^{18}$  photons per second per centimeter square (over a photon energy range of 400 meV)[25] and the total number of quantum dots ( $10^{14}$ ), we obtain an S-P average absorption cross section<sup>6</sup>  $\sigma = 0.1 \pm 0.05 \text{ nm}^2$ . From Eq. 4.3 we obtain, with an average S-P oscillator strength

<sup>6</sup>The absorption cross section  $\sigma$  is defined as the ratio of the absorption rate per quantum dot [energy per time unit] and the incident energy intensity [energy per time and per surface unit].

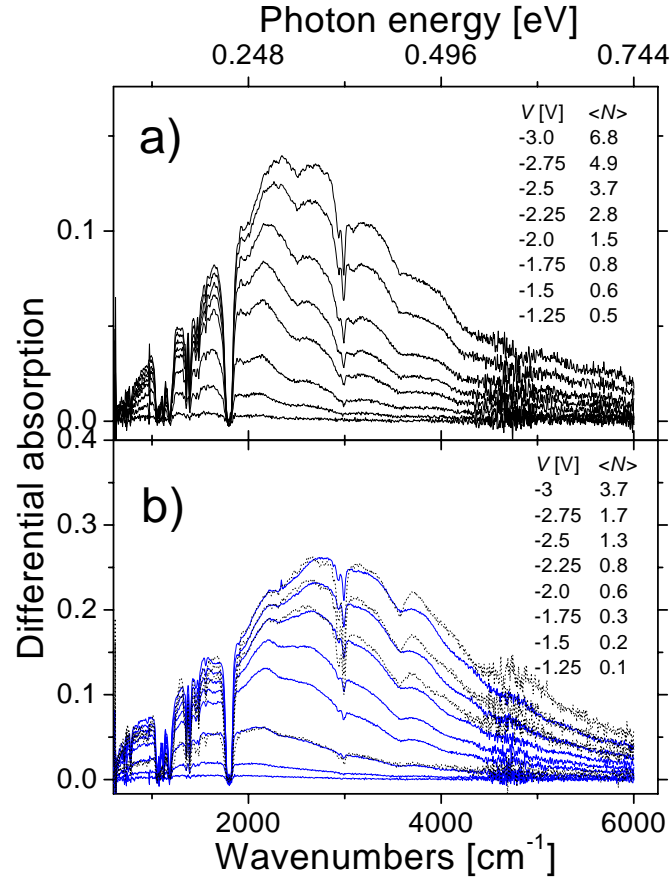


**Figure 4.7:** The increase in the IR absorption by an assembly of ZnO quantum dots due to injection of an increasing number of electrons. The applied potential between the ZnO layer and counter electrode, and the corresponding average occupation number are indicated. For quantum dots with an average diameter of 4.2 nm (a), the average occupation number  $\langle N \rangle$  can be as high as 7, where for quantum dots with an average diameter of 3.7 nm (b),  $\langle N \rangle$  reaches only 4 maximally. The excellent reproducibility is shown by the results obtained with another sample (dotted line) in b).

$\bar{f}_{S-P} = 3.5$  ( $\bar{f}_{S-P} = 5.0$  in effective mass approximation) (see Fig. 4.5), for a quantum dot with a diameter of 5 nm,  $\sigma = 0.09 \pm 0.03 \text{ nm}^2$  ( $\sigma = 0.12 \pm 0.03 \text{ nm}^2$  with effective mass approximation), in excellent agreement with the experimental value.

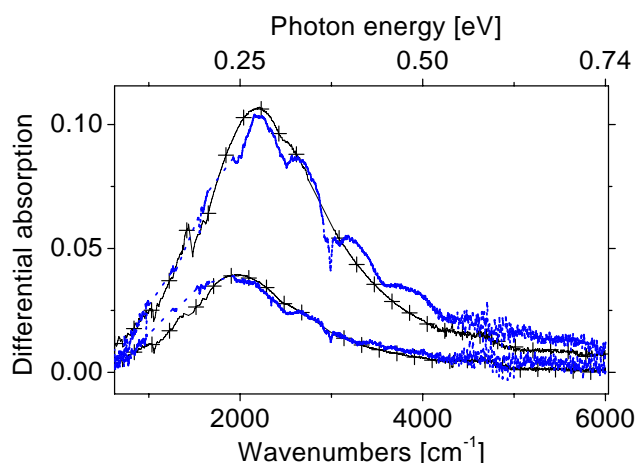


**Figure 4.8:** The increase in the IR absorption of an assembly of ZnO quantum dots (average diameter is 4.2 nm) due to charging with on average 0.8 and 3.7 electrons per quantum dot. The symbols (+) show the increase in the absorption of a colloidal solution of the same ZnO quantum dots, due to excitation with UV light ( $\lambda=300$  nm). The latter spectra are very similar to these obtained with ZnO quantum dot assemblies. The sharp features, below  $2000\text{ cm}^{-1}$ , due to the electrolyte solution have been deleted for clarity.

Figure 4.8 shows the increase in the IR absorption of an assembly of ZnO quantum dots (average diameter is 4.2 nm) due to charging with on average 0.8 and 3.7 electrons per quantum dot. The symbols (+) show the increase in the absorption of a *colloidal solution* of the same ZnO quantum dots, due to photochemical charging with UV light (see section 4.7.2). The spectra are multiplied by a constant factor in order to account for the different number of quantum dots in the IR-optical path in the case of an assembly and a dispersion. It can be seen that the spectra obtained with solutions have a very similar shape to those obtained with the assembly. This suggests that the electronic coupling between the ZnO quantum dots in an assembly is weak. In addition, the redshift of the exciton absorption of an assembly of ZnO quantum dots, compared to a colloidal solution of ZnO quantum dots is very small [7]. This further supports the idea that the coupling between neighbouring quantum dots is weak. Finally, the magnitude of the mobility of electrons in an assembly of ZnO quantum dots, due to tunneling between conduction band levels, also indicates a weak overlap of the conduction band orbitals of neighbouring quantum dots. Therefore, we will assume that or-



bital overlap in an assembly of ZnO quantum dots is not important in the electric dipole transitions; thus uncoupled quantum dots will be considered (sections 1.6 and 1.7).

## 4.6 Quantitative analysis of the spectra

### 4.6.1 A statistical model

Tunneling of an electron between two conduction orbitals of adjacent ZnO quantum dots occurs on a time scale of nanoseconds [7]. On the other hand, the relaxation of electrons from a higher to a lower conduction level is extremely fast (of the order of a ps [26]). We therefore can assume that the electrons injected in a ZnO assembly are in electrochemical equilibrium. In this section we present a model for the absorption of a collection of quantum dots with a given size distribution and an electrochemical potential  $\mu$ . We calculate the electron occupation  $N$  of a quantum dot of diameter  $D$  for a given electrochemical potential  $\mu$  and temperature  $T$ . In combination with the expression for the absorption of a quantum dot with  $N$  electrons given in section 4.4.2, we are able to calculate the total absorption in a ZnO assembly as a function of the average occupation number  $\langle N \rangle$ .

The occupation number  $N$  of a quantum dot with radius  $R$  (present in a quantum dot assembly with electrochemical potential  $\mu$ ) is most easily obtained by considering the electron addition energy  $\mu_N$ . The electron addition energy  $\mu_N(R)$  is defined as the energy required to add one electron to a quantum dot (with radius  $R$ ) containing  $N - 1$  electrons in the conduction band, i.e.

$$\mu_N = E_N - E_{N-1}, \quad (4.9)$$

where  $E_N$  is the internal energy of a quantum dot with  $N$  excess electrons. The occupation number is obtained by counting all electron additions for which  $\mu_N(R)$  is smaller than the electrochemical potential  $\mu$ .

If an electron is added to a quantum dot with  $N - 1$  electrons, it occupies a conduction state with a kinetic confinement energy  $\varepsilon_N$  (see section 4.3). The charge of this electron, with wave function  $\psi$ , will polarize the quantum dot and its environment; as a result there is a polarization energy

$$\Sigma_N = \frac{1}{2} \int -e|\psi(\mathbf{r})|^2 V(\mathbf{r}) d\mathbf{r}, \quad (4.10)$$

where  $V$  is the electrostatic potential due to the charge distribution  $-e|\psi(\mathbf{r})|^2$ . Furthermore, there is the repulsion energy  $J_N$  due to the Coulomb interaction with the  $N - 1$  conduction electrons already present in the dot;

$$J_N = \int -e|\psi(\mathbf{r})|^2 V_{N-1}(\mathbf{r}) d\mathbf{r}, \quad (4.11)$$

where  $V_{N-1}(\mathbf{r})$  is the potential due to the  $N - 1$  other electrons in the dot. For our quantum dots, the exchange energy is about an order of magnitude smaller than the Coulomb interaction [19], and we neglect it here. The electron addition energy  $\mu_N$  can then be written as

$$\mu_N(R) \simeq \varepsilon_N(R) + \Sigma_N(R) + J_N(R). \quad (4.12)$$

In appendix C we calculate the polarization energy  $\Sigma_1$  for a spherically symmetric electron charge distribution with respect to the polarisation energy in a bulk crystal, and find in first order perturbation for the S-level (effective mass model)

$$\Sigma_1 = \frac{e^2}{4\pi\epsilon_o R} \left( \frac{1.01}{\epsilon_{in}} + \frac{1}{\epsilon_{out}} \right), \quad (4.13)$$

in the approximation that the microscopic static dielectric function  $\epsilon(\mathbf{r}, \mathbf{r}')$  equals the macroscopic static dielectric constant  $\epsilon_{in}(\epsilon_{out})$  inside (outside) the quantum dot. For a ZnO quantum dot ( $\epsilon_{in} = 7.8$  [27]) in propylene carbonate ( $\epsilon_{out} = 55$  [28]) we obtain a polarization energy

$$\Sigma_1 = \frac{0.211 \text{ [eVnm]}}{R \text{ [nm]}}. \quad (4.14)$$

Tunneling of the electron outside the quantum dot delocalizes the charge distribution and hence reduces the polarisation energy with respect to the value we obtained here. On the other hand, the microscopic dielectric function  $\epsilon(\mathbf{r}, \mathbf{r}')$  tends to 1 when  $\mathbf{r} \rightarrow \mathbf{r}'$  and this significantly enhances the polarisation energy relative to the value obtained with the macroscopic dielectric constant [19]. Because the polarisation energy  $\Sigma_l$  and the Coulomb interaction between two electrons  $J_{ll'}$  depends on  $l, l' (=S, P)$  only by a few meV [19] and because correlation effects between electrons are of the order of a few meV [19], [9], [10], [12] we make the approximation<sup>7</sup>

$$\Sigma_N \simeq \Sigma_1 \quad (4.15)$$

and

$$J_N \simeq 2(N - 1)\Sigma_1. \quad (4.16)$$

In this way we obtain an *electric* addition energy  $\mu_N^{el} (= \mu_N - \varepsilon_N)$

$$\mu_N^{el}(R) = (2N - 1)\Sigma_1. \quad (4.17)$$

---

<sup>7</sup>The accuracy of our method in the separation of the energy levels is about 100 meV (see Fig. 4.13).

Eq. 4.17 corresponds to the constant capacitance of electron addition better known as the 'standard model' which has been used frequently for metallic nanocrystals and larger (10 to 100 nm) semiconductor quantum dots defined by lithography [4], [29]. In our fitting procedure, we use an electron addition energy  $\mu_N(R) = \varepsilon_N(R) + (2N - 1)\frac{1}{2R}C$  in accordance with Eq. 4.17, where  $C$  is a constant parameter that can be adjusted to fit the experimental absorption spectra. The Coulomb interaction between two neighbouring charged quantum dots in our electrolyte (with a Debye screening length  $L$  of 1.2 nm) is of the order of  $10^{-1}$  meV and is neglected.

At a temperature of 0 K, all single-particle energy levels in a quantum dot with radius  $R$  that have an addition energy  $\mu_N(R)$  smaller than the electrochemical potential  $\mu$  will be filled. With  $R_N$  we denote the radius of the smallest quantum dot with  $N$  electrons. This radius is the solution of the equation

$$\mu = \mu_N(R_N). \quad (4.18)$$

The addition energy  $\mu_N(R)$  is calculated with tight-binding values for the kinetic confinement energy  $\varepsilon_N(R)$ , and an electric addition energy  $\mu_N^e = (2N - 1)\frac{1}{2R}C$ . Equation 4.18 is third order in  $R_N$  and is solved numerically with an accuracy up to a few percent. Because  $\mu_N$  increases with  $N$  and decreases with  $R$ ,  $R_{N+1} > R_N$ . Quantum dots with a radius  $R$  between  $R_N < R < R_{N+1}$  have  $N$  electrons. By calculating the radii  $R_N$  for  $N = 1$  to  $N = 32$  (F-like shell filled), we obtain the occupation number for all quantum dots in our assembly. As an example we show in Fig. 4.9 the electron occupation in a collection of ZnO quantum dots with a relevant size-distribution around the average diameter of 4.2nm. The radii  $R_N$  are indicated for an average occupation number  $\langle N \rangle = 1.3$  (a) and  $\langle N \rangle = 2.8$  (b). At a temperature  $T$ , the occupation of a single-particle level  $\varepsilon_N$  in a quantum dot with radius  $R$  is given by the Fermi-Dirac distribution  $f = \frac{1}{1 + e^{\frac{\mu_N(R) - \mu}{kT}}}$ .

Since we now have the occupation number as a function of the diameter of the quantum dot, we can calculate the IR absorption by each class of quantum dots with a given occupation number. The absorption of the sample due to charging of the quantum dots is of the order of  $10^{-1}$ . This means that the IR intensity throughout the sample is nearly constant. In combination with the incident IR photon rate ( $10^{18}$  photons per second [25]) and the number of quantum dots in the sample ( $10^{14}$ ), we obtain a S-P absorption rate of the order of  $10^3$  photons per quantum dot per second. It has been shown that an electron excited to a P level decays to the S level on a picosecond time scale [26]. Thus, all IR photons are absorbed by the quantum dots with ground state electronic configuration. Furthermore, since the absorption probability per quantum dot per photon is much smaller than one ( $\simeq 10^{-15}$ ), the cross section for a quantum dot with  $N$  electrons is the sum of the

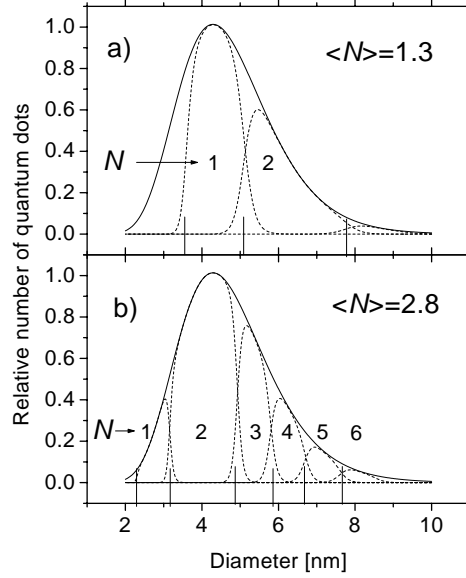


**Figure 4.9:** The solid line shows the size distribution of a collection of quantum dots with an average diameter of 4.2nm. The smallest diameters of a quantum dot with  $N$  electrons at a temperature of 0 K,  $2R_N$ , are indicated for an average occupation number  $N=1.3$  (a) and  $N=2.8$  (b)). The dashed lines show the distribution of quantum dots with one up to six electrons at room temperature. Addition energies  $\mu_N(R)$  are taken from the best fit to experimental results.

cross sections of a quantum dot with one single electron, under the assumption that the cross section for a transition is independent of spectator electrons.

#### 4.6.2 Discussion of the results

We now have a model for the absorption of a collection of ZnO quantum dots with a given size distribution, electrochemical potential  $\mu$  and temperature  $T$ . From the occupation number as a function of the diameter of the quantum dot, we also calculate the average occupation number  $\langle N \rangle$  as a function of the electrochemical potential. Experimentally we have measured the change in the IR absorption due to charging of the quantum dots with on average  $\langle N \rangle$  electrons per dot. We now compare the experimental absorption spectra with those obtained from our model.

The fitting parameters in our model are i) the values for the single-particle energy levels  $\varepsilon_N$ , ii) the averaged oscillator strengths  $\bar{f}_{ll'}$  of the allowed transitions and iii) the electric charging energy  $\mu_N^{el} = \frac{2N-1}{2R}C$  and iv) the size distribution of the quantum dots.

Figure 4.10 presents the IR absorption spectra for a quantum dot assembly (diameter of ZnO nanocrystals is 4.2 nm) for  $\langle N \rangle$  equal to 0.8 and 4.9. With increasing  $\langle N \rangle$ , the maximum of the absorption spectrum shifts to higher energy, and the integrated intensity of IR absorption increases markedly. The latter observation indicates that the number of optical transitions increases when, besides the S-, the P-orbitals also become occupied with electrons. We have fitted the absorption curves, with the energy separations between the S,P,D,S' and F electron orbitals and the relative oscillator strengths for the allowed transitions as adjustable parameters. Figure 4.10 a) shows the results for a low average occupation number;  $\langle N \rangle = 0.8$ . The absorption curve can be accounted for by the allowed S-P transition ( $\Delta l = +1$ ). For  $\langle N \rangle = 0.8$ , the sample consists of nanocrystals with 0, 1 and 2 electrons (see Fig. 4.9). The contribution of the nanocrystals with one electron corresponds to the right shoulder in the fit. (Note that the dip at 3000  $\text{cm}^{-1}$  is due to absorption by the electrolyte.) The contribution of the nanocrystals with two electrons provides the left part. The energy separation between the S and P electron levels is obtained from the position of the absorption peak. There is also a very small contribution from a P-D transition. This is due to the fact that a small fraction of the (largest) quantum dots in the assembly have an electron in a P-orbital. We remark that the absorption at the high energy side cannot be explained by a P-S' transition. The width of the S-P transition is about 200 meV. This width is due solely to the size distribution of the quantum dots. This is supported by measurements at 10 K, which provide absorption spectra that are nearly identical to those at room temperature. A similar width has been observed for the S-P transition in a sample of CdSe quantum dots[30].

For  $\langle N \rangle = 4.9$ , transitions from the P-orbitals to higher lying orbitals are expected. Figure 4.10b shows the contributions of the distinct transitions to the overall absorption spectrum. The main contribution comes from the P-D optical transition ( $\Delta l = +1$ ). The steps on the high energy side are due to the contributions of sub-ensembles of nanocrystals, each with a distinct number of P-electrons. Each sub-ensemble has a different average diameter, and gives thus a contribution at slightly different energy due to the effect of quantum confinement. The energy separation between the P and D levels is obtained from the position of the peak in the absorption spectrum. The average oscillator strength of the P-D transition  $\bar{f}_{PD}$  (relative to that of the S-P transition) is obtained from the intensity of the absorption curve. The remaining S-P contribution is merely due to

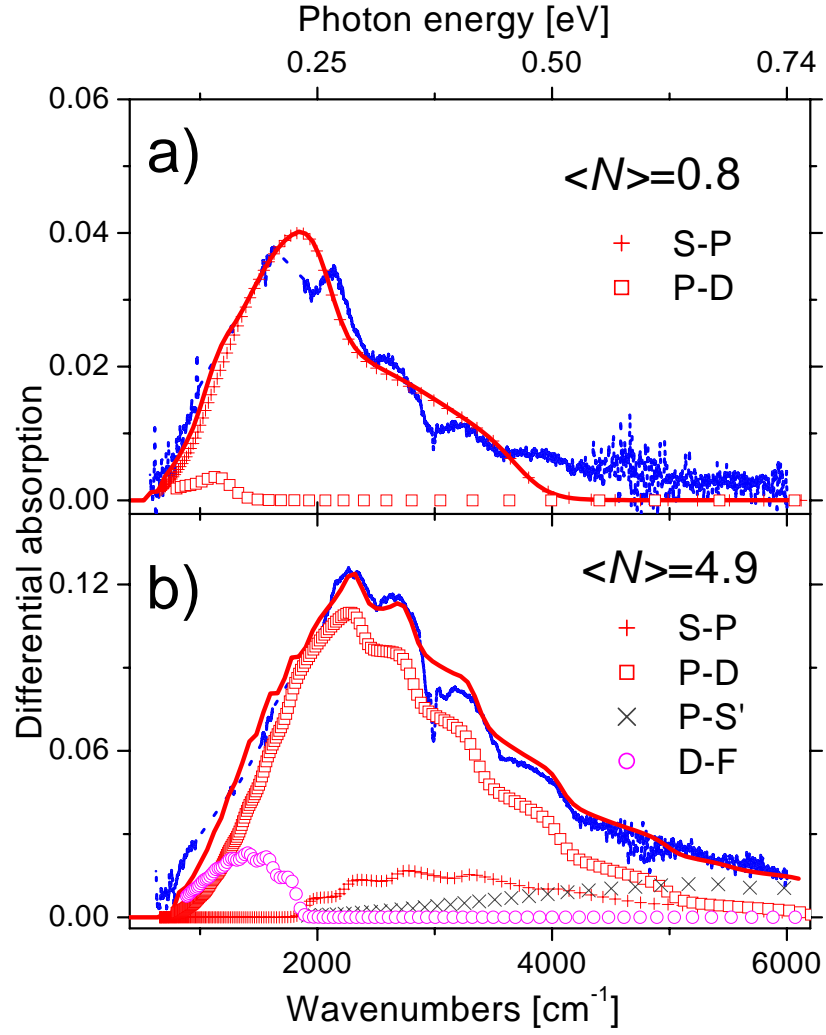


**Figure 4.10:** Absorption spectra (black lines) and corresponding fits (grey solid lines) for a ZnO quantum dot assembly (average diameter is 4.2 nm) at low and higher occupation  $\langle N \rangle$ . The spectrum for  $\langle N \rangle = 0.8$  can be fitted with an S-P (+) and a forbidden S-D (x) transition. The spectrum for  $\langle N \rangle = 4.9$  can be fitted with the S-P (+) and S-D (x) transition and the P-D ( $\square$ ) and P-S' ( $\circ$ ) transition.

the subset of the smallest quantum dots in the sample. Note that the maximum of the S-P contribution is therefore at higher energy than that of the S-P contribution for  $\langle N \rangle = 0.8$ . Moreover, despite the fact that there are two electrons in the S orbitals, the total S-P intensity has decreased markedly compared to that for  $\langle N \rangle = 0.8$ . At  $\langle N \rangle = 4.9$  most particles have already three electrons in a P-level, which strongly reduces the S-P intensity (see section 4.4.2). The subset of largest particles have occupied D-orbitals. This leads to a D-F contribution ( $\Delta l = +1$ ) at the low energy side of the spectrum. The tail at the high energy side of the spectrum is merely accounted for by the allowed P-S\* ( $\Delta l = -1$ ) transitions.

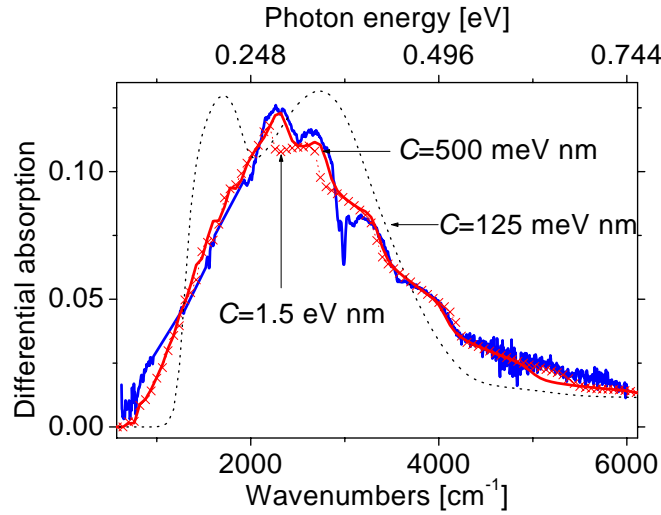


**Figure 4.11:** The increase in absorption of a quantum dot assembly (average diameter is 4.2nm) due to charging with on average 4.9 electrons, is shown with the predictions from our model for different values of the parameter  $C$  ( $\mu_N^{el} = \frac{2N-1}{2R}C$ ). The first peak in the curve with  $C = 125$  meV is due to D-F transitions, the second peak mainly due to P-D transitions.

Figure 4.11 shows the increase in absorption of a quantum dot assembly due to charging with on average 4.9 electrons, and the predictions from our model for different values of the electric addition energy  $\mu_N^{el} = \frac{2N-1}{2R}C$ . From section 4.6, we know that the electric addition energy determines the electron occupation of the quantum dots (with radius  $R$ ) in the assembly. From a fitting of the experimental spectra we obtain  $C = 500 \pm 200$  [eV nm]. For a quantum dot with two electrons ( $N = 2$ ) and radius of 2 nm, this corresponds to an electric addition energy of 375 meV. In section 4.6, we find from a rough approximation (see Eq.



4.14) that  $C = 422 \text{ meV nm}$ . From the differential capacitance function obtained in a three-electrode system, it is found that the electric charging energy is about  $C = 420 \text{ meV nm}$ , which is very close to the value obtained from our experiment.

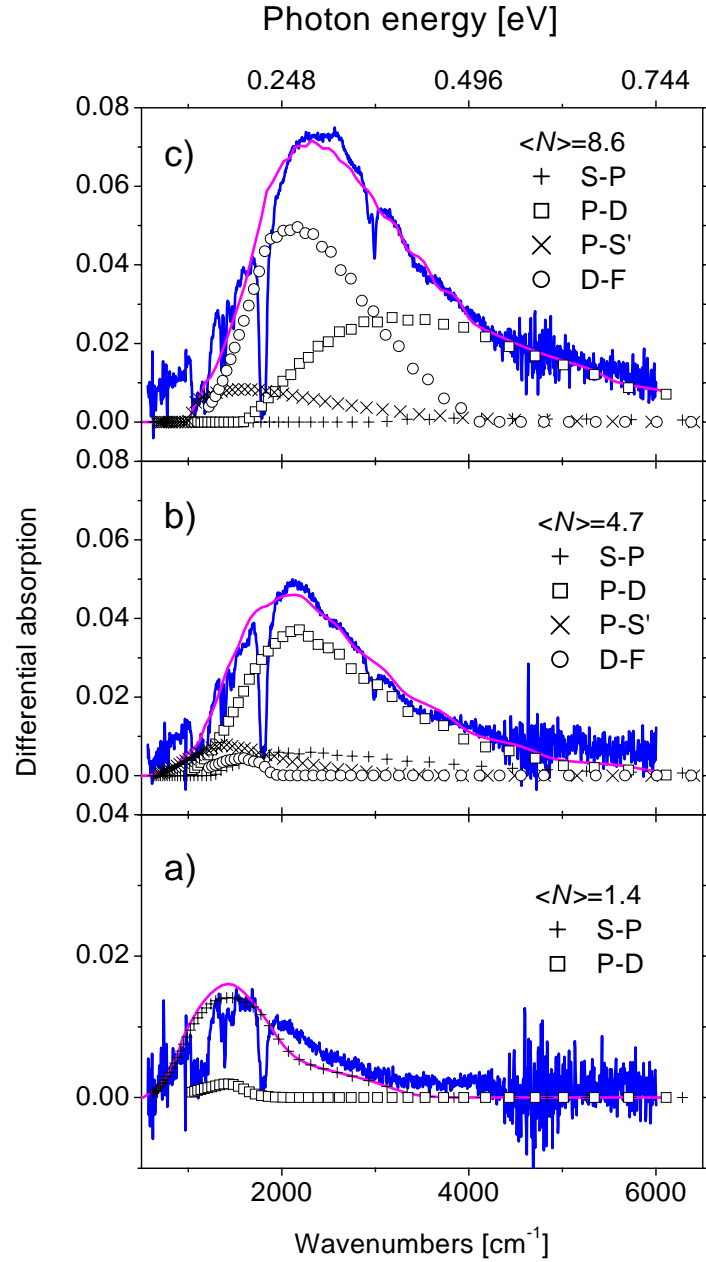


**Figure 4.12:** Absorption spectra (black lines) and corresponding fits (grey solid lines) for a ZnO quantum dot assembly (average diameter is 5.2 nm) at different occupation numbers  $\langle N \rangle$ . The spectrum for  $\langle N \rangle = 1.4$  can be fitted with an S-P (+) and a P-D (□) transition. The spectra for  $\langle N \rangle = 4.7$  and  $\langle N \rangle = 8.6$  can be fitted with the S-P (+), P-D (□), P-S' (×) and D-F (○) transition.

Figure 4.12 shows the absorption spectrum for a quantum dot assembly with an average diameter of 5.2 nm. The spectrum with  $\langle N \rangle = 1.4$  can essentially be fitted with a S-P transition. There is a small contribution from a P-D transition. From the fitting of this spectrum we obtain information on the energy separation between the S and P level. The spectrum with  $\langle N \rangle = 4.7$  is fitted with a S-P, P-D, P-S' and D-F transition. Because the main contribution comes from the P-D transition, we essentially obtain information on the energy separation between the P and D level, and the oscillator strength of the P-D transition, relative to the oscillator strength of the S-P transition. The spectrum with  $\langle N \rangle = 8.6$  provides information on the energy separation between the F and D level, and the oscillator strength of the D-F transition, relative to the S-P transition.

In summary, we have shown that, by fitting the IR absorption spectra for a gradually increasing occupation of the ZnO quantum dots, we obtain the relative oscillator strengths for the allowed transitions and the energy separations between the S, P, D and F levels. The contribution from P-S' is too broad and too weak to obtain reliable data for the P-S' energy separation.

We analyzed the absorption spectra for ZnO quantum dots of three different sizes: 3.7 nm ( $0 < \langle N \rangle < 1.7$ ), 4.2 nm ( $0 < \langle N \rangle < 4.9$ ), and 5.2 nm ( $0 < \langle N \rangle < 8.6$ ). In Figure 4.13 the single-particle energy separations that we obtain from analysis of the spectra are compared with the tight binding values and the values obtained by the effective mass approximation. The dependence of S-P and P-D energy separation on the nanocrystal diameter is in line with theory. Quantitatively, the experimental S-P, P-D and D-F separations are somewhat larger than the values calculated with the *spds*\* tight-binding model used here. The reason for this difference may be an inaccurate description of the surface of the quantum dot. Tight-binding calculations with different surface atoms passivating dangling bonds have shown that the energy levels sensitively depend on the surface termination [31], [32]. The presence of an internal electric field and deviations from the spherical shape are other possible reasons for the difference between the experimental and calculated results.

The oscillator strengths that we have obtained from a fit of the IR absorption spectra are compared with the tight-binding values in Table 1.1. We have taken the experimental oscillator strength of the S-P transition equal to the tight-binding value. The table presents therefore a comparison of the relative oscillator strengths for the different allowed transitions. For the quantum dots of 3.7 and 4.2 nm, we find a remarkable agreement between observed and calculated values. The oscillator strengths observed for the particles of 5.2 nm are higher than those predicted by tight-binding theory. The reason for this discrepancy is not yet clear.

Fig. 4.9 shows the size distribution used to fit the IR absorption spectra for

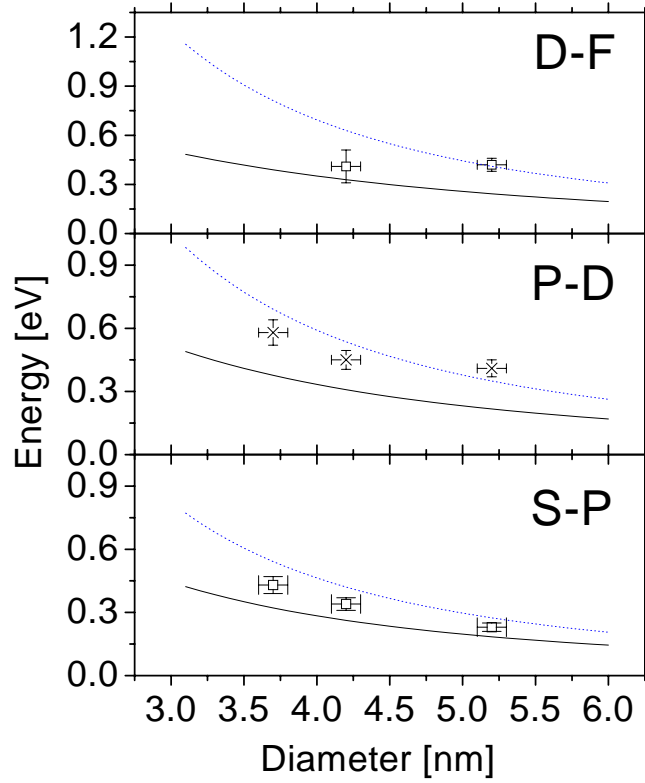


**Figure 4.13:** The separations between the single-electron energy levels obtained from the IR spectra (symbols) and calculated with tight binding theory (solid lines) and effective mass approximation (dotted lines), as a function of the diameter of the ZnO nanocrystals.

quantum dots with an average diameter of 4.2 nm. The asymmetrical log-normal distribution is obtained from TEM pictures of similar quantum dots [33], [34]. The width of the size distribution necessary to fit the IR absorption spectrum is however, much larger than the width obtained from TEM size histograms which is about 20 % of average diameter [23]. Below, we evaluate some phenomena which might be important in the broadening of the IR absorption spectra. The precise reason for the broadening of the spectra which is accounted for in our fit-

**Table 4.1:** The summed dipole oscillator strength  $2(2l + 1)\bar{f}_{ll'}$  are shown for different allowed transitions. Theoretical values are obtained with tight-binding model. The experimental S-P oscillator strength is set equal to the theoretical value. This allows us to compare the oscillator strengths of the P-D, D-F and P-S' transitions with the theoretical values.

Diameter [nm]		S-P	P-D	D-F	P-S'
3.7		6.1	$18 \pm 2$	—	—
	Theory	6.1	18.3	33.8	3.2
4.2		6.4	$21 \pm 2$	$36 \pm 14$	$4 \pm 2$
	Theory	6.4	19.2	36.2	3.4
5.2		6.6	$29 \pm 4$	$54 \pm 10$	$4 \pm 3$
	Theory	6.6	20.7	40.5	3.7

ting model by an anomalous broadening of the size-distribution is not yet clear. Spectra obtained at 10 K have a width almost identical to spectra obtained at room temperature (see Fig. 4.19). This excludes broadening due to the absorption of phonons in the electronic transition. Also a coupling of the electron levels with the (fluctuating) dipoles of the solvent can very probably be excluded. The linewidth of an IR transition between conduction levels in a quantum dot due to its lifetime ( $\simeq$  a picosecond [26]) is of the order of a meV and can thus also not explain the broad spectra. Band-edge exciton emission and absorption measurements on an identical assembly of ZnO quantum dots show a similar width as obtained from IR absorption measurements. Size-selective band-edge exciton absorption measurements have shown that phonon replicas can shift the optical absorption by 40 meV [35]. Capacitance measurements on a ZnO quantum dot assembly in the same electrolyte solution as we have used (propylene carbonate) show a size distribution identical to that needed to explain the IR absorption spectra. We conjecture that shape asymmetry [35], surface atoms [31] and changes in the local electric field (spectral diffusion) [36]-[37] are factors that might explain the dispersion in the kinetic confinement energy levels  $\varepsilon_N$  and perhaps the anomalous width of the spectra.

## 4.7 IR absorption spectroscopy of a colloidal solution of ZnO quantum dots

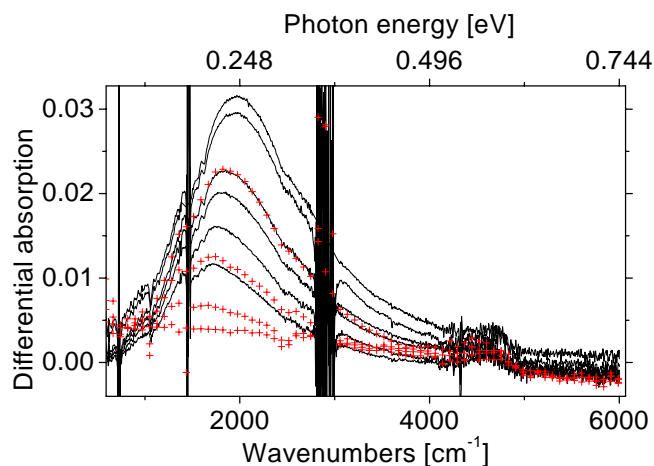
### 4.7.1 Experimental

The quantum dots that we used in IR absorption measurements with colloidal solutions are identical to those used to prepare the assemblies. Their synthesis and characterization has been discussed in section 4.5.1. From the amount of reagents, we know that the volume fraction of ZnO quantum dots to the total volume is  $3.8 \cdot 10^{-3}$ . IR absorption measurements are performed using a UV transparent plastic bag containing 40 mg of the quantum dot solution. Photochemical charging of the quantum dots is performed by illumination with a Xe-lamp. The wavelength of the excitation light is selected by a monochromator with a spectral width of 5 nm. The exciton absorption by 100  $\mu\text{m}$  of the colloidal solution is of the order of 0.1. All IR absorption measurements are performed with a Bio-rad FTIR spectrometer FTS-40, at room temperature in a nitrogen purged environment.

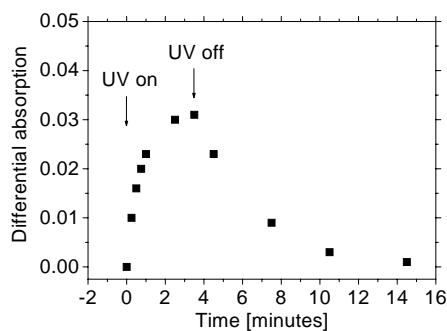
### 4.7.2 Results and discussion

Figure 4.14 shows the increase in the absorption of a colloidal solution of ZnO quantum dots, due to the illumination with UV light (4 eV). Upon UV illumination of a colloidal solution of ZnO quantum dots in ethanol, electron-hole pairs are created. The relaxation of an electron from a higher electron state to the lowest conduction state occurs on a time scale of 600 fs via a Auger-like electron-hole energy transfer [38]. Holes are selectively removed by electron transfer from an ethanol molecule, which is, in a second step oxidised to  $\text{CH}_3\text{-CHO}$  [39]. As a result negatively charged quantum dots with electrons in the lowest levels of the conduction band are formed. Charged quantum dots slowly discharge e.g. due to the presence of an electron scavenger like oxygen.

The absorption spectra are measured at different time delays after the illumination is switched on and off. Figure 4.15 shows the increase (decrease) in the absorption peak maximum as a function of the time after the illumination is switched on (off). The absorption increases with time and saturates typically  $3 \pm 1$  minutes after the start of the illumination. After switching off the illumination, the absorption returns to its value before the illumination started, on a time scale of  $10 \pm 2$  minutes. It can be seen from Fig. 4.14 that the spectra measured during the illumination are equal to those measured after the illumination is switched off. The width of the absorption peak increases with the illumination time, and the position of the absorption peak shifts to higher energy. The perturbations at 3000 and 1500  $\text{cm}^{-1}$  are due to changes in the (strong) absorption of the plastic sample



**Figure 4.14:** The increase in the absorption of a colloidal solution of ZnO quantum dots (average diameter is 4.2 nm) due to illumination with UV light (4eV). The spectra are measured at different time delays after the UV illumination is switched on (0.25, 0.5, 0.75, 1, 2.5, 3.5 minutes) (solid lines), and switched off (1, 4, 7, 11 minutes)(+). The perturbations observed at 1500 and 3000  $\text{cm}^{-1}$  are due to the absorption of the plastic bag.



**Figure 4.15:** The change in the maximum of the absorption peak of a colloidal solution of ZnO quantum dots at room temperature, as a function of the time after the UV illumination (4 eV) is switched on (rising part) and off.

holder. The spectrum measured 11 minutes after switching off the illumination

is slightly shifted from zero due to the instability of the FTIR spectrometer. The absorption of the sample without quantum dots, i.e. the absorption of the solvent and the plastic sample holder does not change upon illumination.

The absorption spectrum that we obtain here is very similar to the absorption spectra obtained with an assembly of quantum dots (see Fig. 4.8). The changes in the absorption spectra as a function of time are analogous to the changes in the spectra of an assembly for an increasing average occupation number  $\langle N \rangle$ .

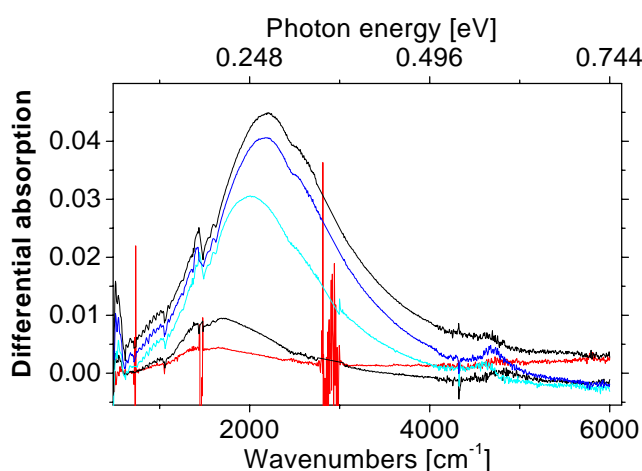


**Figure 4.16:** The change in the absorption of a colloidal solution of ZnO quantum dots (average diameter is 4.2 nm) due to illumination with different excitation wavelengths (from bottom to top:  $\lambda=400, 380, 360, 340$  and  $300$  nm). The spectra are normalized to incident photon flux.

Figure 4.16 shows the change in the absorption of a colloidal solution of ZnO quantum dots due to illumination with different excitation wavelengths. The absorption does not change if the solution is illuminated with light of a photon energy smaller than the bandgap of ZnO (3.2 eV for macrocrystalline ZnO). This indicates that the IR absorption requires the presence of conduction electrons in the quantum dots. For increasing photon energy, the total absorption and the width of the absorption peak increase. The position of the absorption peak shifts to higher energies for increasing photon energies. Because of the size-dependence of the conduction energy levels, increasing the photon energy enables smaller quantum dots to be photo-excited. Size-selective excitation could provide, in principle, information on the IR absorption of a smaller size distribution of dots. However, we have strong indications that electron transfer occurs between dots (see further).



By such a process electrons are redistributed over the dots in the sample.

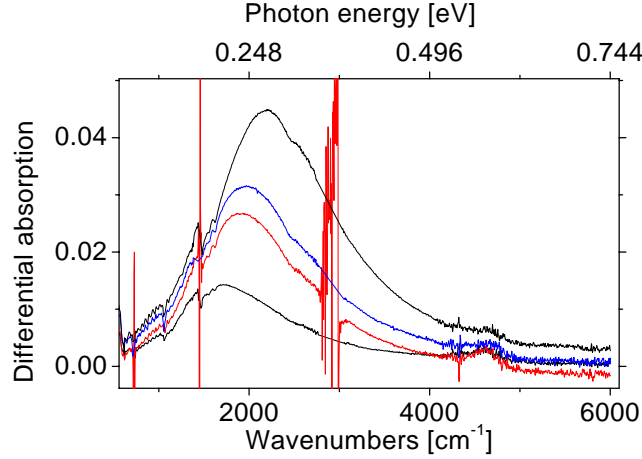


**Figure 4.17:** The change in the absorption of a colloidal solution of ZnO quantum dots (average diameter is 4.2 nm) due to illumination for different excitation intensities ( $\lambda=300$  nm). The spectra are obtained at (from bottom to top) 2.5%, 5%, 10% and 100% of the UV intensity ( $3.6 \cdot 10^{15}$  photons/s  $\text{cm}^2$ ).

Figure 4.17 shows the change in the absorption of a colloidal solution of ZnO quantum dots due to illumination ( $\lambda = 300\text{nm}$ ) with different excitation intensities. The absorption and the width of the absorption peak increase with increasing excitation intensity. The position of the absorption peak shifts to higher energies with increasing excitation intensity. The integrated absorption is linear in the illumination intensity up to about 5 % of the maximum intensity, and sublinear for higher intensities. Since the average oscillator strength  $\bar{f}_{ll'}$  is about identical for S-P and P-D transitions (see Fig. 4.5), this indicates that the efficiency of photochemical generation of an electron in a ZnO nanocrystal decreases if there is already one or more electrons present in the conduction levels. Identification of the colloidal spectra with those obtained with an assembly (see Fig. 4.8) indeed shows that  $\langle N \rangle \simeq 1$  for an illumination intensity of 5 % of the maximum.

The isomorphism between the IR absorption spectra obtained with assemblies and solutions (see Fig. 4.8) strongly suggests that the spectra are determined by the average electron occupation number  $\langle N \rangle$  only. This means that quantum dots with  $\langle N \rangle > 1$  can be obtained with photochemical charging (see Fig. 4.8). Furthermore, it strongly suggests that with quantum dot solutions, the distribution of the electrons over the quantum dots of different sizes is very similar to that

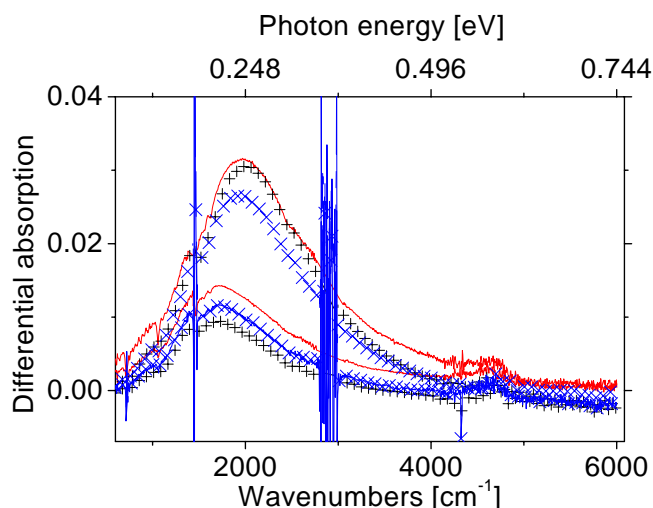


**Figure 4.18:** A comparison of the change in the IR absorption of a colloidal solution of ZnO quantum dots due to illumination in different ways. The solid lines are spectra obtained by photoexcitation at 300 nm with different light intensities; the (+) spectra are obtained with different photon excitation energies, and the (×) spectra are obtained after different waiting times of illumination with  $\lambda = 300$  nm.

in our assembly, where electrochemical equilibrium prevails. It is not clear how electrons in a quantum dot solution equilibrate; a possible mechanism is electron transfer between quantum dots. Furthermore, Fig. 4.18 strongly indicates that electrochemical equilibrium at varying  $\langle N \rangle$  can be achieved by using a variation of the excitation intensities or a variation of the photon energy.

Figure 4.19 shows the change in the absorption of a colloidal solution of ZnO quantum dots due to illumination ( $\lambda = 330$  nm), at a temperature of 300 K (solid line) and 10 K (+). The absorption spectrum at 10 K is almost identical to that measured at 300 K. The intensity is reduced by 30% compared to the spectrum at 300 K, the width is reduced only by a few percent. The rising (relaxation) time of the absorption upon illumination increased from 1 minute (8 minutes) at 300 K to 8 minutes (50 minutes) at 10 K. These results show that ZnO quantum dots can be photochemically charged with electrons even at very low temperatures (10 K). This is surprising since it means that thermally activated electron transfer from an ethanol molecule to the unoccupied valence state can occur with a certain rate also at low temperatures.

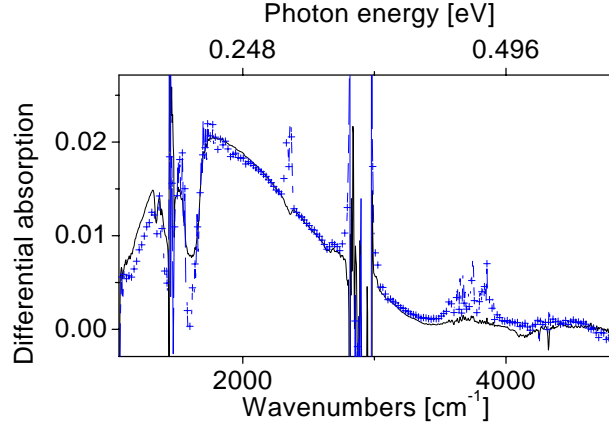


**Figure 4.19:** The change in the absorption of a colloidal solution of ZnO quantum dots due to illumination ( $\lambda=330\text{nm}$ ), measured at a temperature of 300 K (solid line) and 10 K (+). For a better comparison, the spectrum at 300 K is multiplied by a factor 0.68.

## 4.8 Conclusions

In this chapter we have shown that artificial atoms can be prepared by electrochemical injection of electrons in an assembly of weakly coupled ZnO quantum dots with a diameter between 3 and 6 nm. The injected electrons occupy the conduction electron orbitals of the ZnO nanocrystals. By measuring the injected charge and the number of nanocrystals in the assembly, the average electron number  $\langle N \rangle$  can be obtained. We have shown that up to ten electrons can be confined in the ZnO nanocrystals, thus that artificial atoms with  $S^1$ ,  $S^2$ ,  $S^2P^1$ , ... electron configurations can be studied. On the other hand, the same artificial atoms can also be prepared using a colloidal solution of ZnO nanocrystals in ethanol. Formation of an electron-hole pair by absorption of a photon with energy in the near UV and subsequent removal of the hole by electron transfer from an ethanol molecule leads to ZnO nanocrystals with one or more electrons in the conduction orbitals.

Using absorption spectroscopy in the near-IR we have studied the optical transitions in these artificial atoms. By gradually increasing the electron number, we could identify the contributions of the S-P, P-D, D-F and P-S' allowed electric dipole transitions to the total absorption spectrum could be identified. The absorp-

tion spectra can be understood by a comprehensive model. The model is based on the allowed electric dipole transitions between the atom-like conduction orbitals of the ZnO quantum dots. The distribution in the size of the ZnO nanocrystals in the sample is the most serious problem. It is accounted for by calculating the electron configuration as a function of the diameter of the quantum dots for a given average occupation number  $\langle N \rangle$  assuming electronic equilibrium between the dots. In this way the experimental absorption spectra could be fitted accurately and in a self-consistent way. There is, however, one remaining problem: the size distribution needed to explain the spectra is considerably broader than that found by analysis of TEM pictures. The relative oscillator strengths of the S-P, P-D, D-F and P-S\* transitions were found to be in excellent agreement with the values calculated with an effective mass approximation and with a more sophisticated tight-binding theory. This means that the optical transitions are completely determined by the symmetry of the envelope wave functions, expressed by the quantum number  $l$ . Here, we wish to remark that generally excitonic HOMO-LUMO transitions cannot be explained in such a simple way [40]. From the analysis, the single-particle energy separations between the S, P, D, and F can also be obtained. The increase of these separations with decreasing size of the dots due to quantum confinement are in line with effective mass and tight binding calculations.

## References

---

- [1] A.P. Alivisatos, J. Phys. Chem. **100**, 13226 (1996).
- [2] X.G. Peng, L. Manna, W.D. Yang, J. Wickham, E. Scher, A. Kadavanich, A.P. Alivisatos, Nature **404**, 59 (2000).
- [3] D.V. Talapin, A. L. Rogach, A. Kornowski, M. Haase, H. Weller, Nano Lett. **1**, 207 (2001).
- [4] L.P. Kouwenhoven, D. G. Austing, and S. Tarucha, Rep. Prog. Phys. **64**, 701 (2001).
- [5] A. Franceschetti and A. Zunger, Phys. Rev. Lett. **78**, 915 (1997).
- [6] D. L. Klein, R. Roth, A.K.L. Lim, A.P. Alivisatos, P.L. McEuen, Nature **389**, 699 (1997).
- [7] A. L. Roest, J. J. Kelly, D. Vanmaekelbergh, and E. A. Meulenkaamp, Phys. Rev. Lett. **89**, 36801 (2002).
- [8] A. Franceschetti, A. Zunger, Phys. Rev. B **62**, 2614 (2000).
- [9] G. Bryant, Phys. Rev. B **37**, 8763 (1988).
- [10] Y. Kayanuma, Phys. Rev. B **38**, 9797 (1988).
- [11] L. Brus, J. Chem. Phys. **79**, 5566 (1983).
- [12] P. Lippens and M. Lannoo, Phys. Rev. B **39**, 10935 (1989); J. Proot, C. Delerue, and G. Allan, Appl. Phys. Lett. **61**, 1948 (1992).
- [13] M. Rama Krishna and R. Friesner, Phys. Rev. Lett. **67**, 629 (1991).
- [14] L. Wang and A. Zunger, J. Chem. Phys. **100**, 2394 (1994); J. Phys. Chem. **98**, 2158 (1994).
- [15] E. Merzbacher, *Quantum mechanics*, John Wiley, 1970.
- [16] S. Fonash, *Solar Cell Device Physics*, Academic Press, 1981.
- [17] A. Franceschetti and A. Zunger, Phys. Rev. B **62**, R16287 (2000).
- [18] A. Zunger, Phys. Stat. Sol. (b) **224**, 727 (2001).
- [19] A. Franceschetti and A. Zunger, Phys. Rev. B **62**, 2614 (2000).
- [20] A. Franceschetti, A. Williamson, and A. Zunger, J. Phys. Chem. **104**, 3398 (2000).
- [21] Y. Niquet, Ph. D. thesis, Universite des Sciences et Technologies de Lille (2001).
- [22] J. Elliott and P. Dawber, *Symmetry in physics*, MacMillan Ltd (1985).
- [23] E. A. Meulenkaamp, J. Phys. Chem. B **102**, 5566 (1998).
- [24] E. Meulenkaamp, J. Phys. Chem. B **103**, 7831 (1999).
- [25] Technical specifications of Bio-rad FTIR-spectrometer FTS 40.

- [26] R.J. Warburton, C. Schaflein, D. Haft, F. Bickel, A. Lorke, K. Karrai, J.M. Garcia, W. Schoenfeld, and P.M. Petroff, *Nature* **405**, 926 (2000).
- [27] W. Harrison, *Elementary Electronic Structure*, World Scientific Pub Co (1999).
- [28] U. Schneider, P. Lunkenheimer, R. Brand, and A. Loidl, *Phys. Rev. E* **59**, 6924 (1999).
- [29] D. Averin, A. Korotkov, K. Likharev, *Phys. Rev. B* **44**, 6199 (1991).
- [30] M. Shim and P. Guyot-Sionnest, *Phys. Rev. B* **64**, 245342 (2001).
- [31] N. Hill, K. Whaley, *J. Chem. Phys.* **100**, 2831 (1994).
- [32] A. Alivisatos, *J. Phys. Chem.* **100**, 13226 (1996).
- [33] M. Dib, M. Chamarro, et al., *Phys. Stat. Sol. (b)* **212**, 293 (1999).
- [34] P. Hoyer, R. Eichberger, and H. Weller, *Ber. Bunsenges. Phys. Chem.* **97**, 630 (1993).
- [35] D. Norris, Al. L. Efros, M. Rosen, M. G. Bawendi, *Phys. Rev. B* **53**, 16347 (1996).
- [36] S. Empedocles, D. J. Norris, and M. G. Bawendi, *Phys. Rev. Lett.* **77**, 3873 (1996).
- [37] R. G. Neuhauser, K. T. Shimizu, W. K. Woo, S. A. Empedocles, and M. G. Bawendi, *Phys. Rev. Lett.* **85**, 3301 (2000).
- [38] V. Klimov, and D. McBranch, *Phys. Rev. Lett.* **80**, 4028 (1998).
- [39] A. van Dijken, Ph. D. Thesis, University Utrecht (1999).
- [40] D. Norris and M. Bawendi, *Phys. Rev. B* **53**, 16338 (1996).

## Appendix A: Transmission Line Theory for currents and voltages

---

In this appendix we describe the transport of electromagnetic energy in a waveguide (coax-cable) in terms of the corresponding currents and voltages in the walls of the waveguide. Advantage of this formalism is that a waveguide can be represented as an equivalent electric circuit. As an example we calculate the reflection at an impedance in a waveguide.

Fig. A.1 shows a schematic drawing of a coaxial cable. The voltage  $V(z)$  is defined as the difference in potential between the inner and the outer conductor at the position  $z$ . The current in the inner conductor in the direction of the  $z$  axis is denoted by  $I(z)$ . Currents and voltages in the coax-cable are obtained from the electrical equivalent circuit shown in Fig. A.2. The capacitance per unit length in the  $z$  direction between the inner and outer conductor is given by  $c = \frac{\epsilon\epsilon_0 2\pi}{\ln(a/b)}$ . The energy of the magnetic field perpendicular to the  $z$  axis induced by the current  $I(z)$  can be described by an inductance per unit length  $l = \frac{\mu\mu_0}{2\pi} \ln(a/b)$  where  $\mu$  is the relative permeability of the medium between both conductors. A resistance per unit length  $r$  describes ohmic loss in the conductors. Finally a conductance per unit length  $g$  between both conductors accounts for the (small) conductivity of a dielectric.

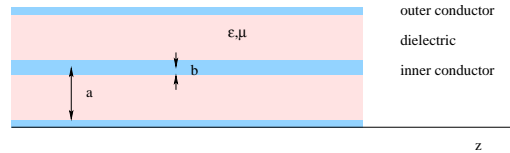


**Figure A.1:** Schematic drawing of a coaxial cable filled with a dielectric with dielectric constant  $\epsilon$  and magnetic permeability  $\mu$ .

The electrical circuit shown in Fig. A.2 can easily be solved in a complex representation of the currents and voltages. With a time dependence given by  $\exp(i\omega t)$  we obtain

$$V(z) - V(z + dz) = I(z)(r + i\omega l)dz \quad (\text{A.1})$$

and

$$I(z) - I(z + dz) = V(z)(g + i\omega c)dz. \quad (\text{A.2})$$

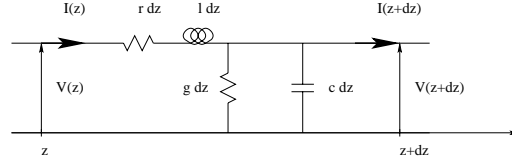


**Figure A.2:** Equivalent electrical circuit of a coaxial cable with length  $dz$ .

These equations can be written as differential equations

$$\frac{\partial V}{\partial z} = -I(r + i\omega l), \quad (\text{A.3})$$

$$\frac{\partial I}{\partial z} = -V(g + i\omega c) \quad (\text{A.4})$$

or equivalently

$$\frac{\partial^2 V}{\partial z^2} = V(r + i\omega l)(g + i\omega c), \quad (\text{A.5})$$

$$\frac{\partial^2 I}{\partial z^2} = I(r + i\omega l)(g + i\omega c). \quad (\text{A.6})$$

The solutions of (A.5) and (A.6) are given by right and left running waves

$$V^{\pm}(z) = V_o^{\pm} \exp(\mp i k_z z + i\omega t) \quad (\text{A.7})$$

and

$$I^{\pm}(z) = I_o^{\pm} \exp(\mp i k_z z + i\omega t) \quad (\text{A.8})$$

where the wave number  $k_z$  is given by

$$k_z = \sqrt{-(r + i\omega l)(g + i\omega c)}. \quad (\text{A.9})$$

From (A.3) follows that

$$V^{\pm} = \pm Z_o I^{\pm} \quad (\text{A.10})$$

where  $Z_o = \sqrt{\frac{r+i\omega l}{g+i\omega c}}$  is called the characteristic impedance of the transmission line. To conclude, for a given radial frequency  $\omega$ , the currents and voltages in a uniform waveguide are completely determined by the complex amplitudes of the right and left running waves e.g.  $V_o^{\rightarrow}$  and  $V_o^{\leftarrow}$  and the complex impedance  $Z_o$ .



As an example of the above formalism we describe the reflection of an incoming wave with amplitude  $V_o^{\rightarrow}$  for  $z = 0$  at a distance  $l$  from a load impedance  $Z_L$  (see Fig. A.3).

By definition

$$Z_L = \frac{V^{\rightarrow}(z=l) + V^{\leftarrow}(z=l)}{I^{\rightarrow}(z=l) + I^{\leftarrow}(z=l)}. \quad (\text{A.11})$$

Because of (A.10) this is equal to

$$Z_L = \frac{V^{\rightarrow}(z=l) + V^{\leftarrow}(z=l)}{V^{\rightarrow}/Z_o(z=l) - V^{\leftarrow}/Z_o(z=l)} \quad (\text{A.12})$$

which can be written as

$$\frac{V^{\leftarrow}(z=l)}{V^{\rightarrow}(z=l)} = \frac{Z_L - Z_o}{Z_L + Z_o}. \quad (\text{A.13})$$

Amplitudes for  $z = 0$  can easily be obtained from the amplitudes for  $z = l$  using (A.7). In this way we obtain for the reflection coefficient at  $z = 0$

$$R(z=0) = \frac{V_o^{\leftarrow}}{V_o^{\rightarrow}} = \exp(-2ik_z l) \frac{Z_L - Z_o}{Z_L + Z_o}. \quad (\text{A.14})$$

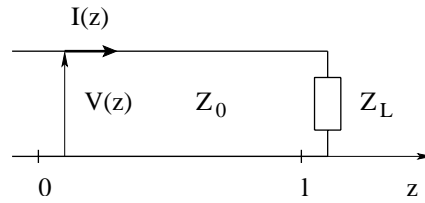


**Figure A.3:** Electrical equivalent circuit of a transmission line ended with a load impedance  $Z_L$ .



## Appendix B: Dielectric constant of a porous semiconductor

---

We discuss a model for the dielectric constant of porous GaP at microwave frequencies. During one microwave period  $2\pi/\omega \simeq 10^{-10}$  s, free electrons are transported over a distance which is at maximum given by  $\mu E 2\pi/\omega$  where  $E$  is the microwave-induced electric field inside the semiconducting part and  $\mu$  is the mobility inside the semiconducting part. Due to screening, the electric field strength in the semiconducting part is smaller than the amplitude of the applied microwave electric field which is of the order of 10 V/cm. With the mobility  $\mu$  for bulk GaP ( $\mu = 130 \text{ cm}^2/\text{Vs}$  [1, 2]) we obtain a transport distance of the order of 1 nm. This distance is much smaller than the size of the porous structure. The dielectric constant obtained from microwave conductivity measurements thus reflects short range motion of the free electrons in macroporous GaP. Fig. 3.1 shows that the porous structure is random and has a typical size of 150 nm. Therefore, in a description of the dielectric constant of porous GaP at microwave frequencies, we model the porous structure as a collection of isolated spheres with a typical radius  $R$  equal to 75 nm. Because of surface states with an energy level in the bandgap, a region at the surface of the semiconductor is depleted of free electrons and only the inner core of these spheres, with a radius  $R_c$  is semiconducting.

In the Clausius-Mossotti approximation, the dielectric constant  $\epsilon$  of a collection of particles is related to the polarizability of one particle  $\alpha$  via [3]

$$\frac{\epsilon(\omega) - 1}{\epsilon(\omega) + 2} = f\alpha(\omega). \quad (\text{B.1})$$

In this expression  $f$  is the fraction of the volume of the spheres to the total volume. In a complex representation of physical quantities, the time dependence is given by  $\exp(-i\omega t)$  and  $\alpha$  and  $\epsilon$  can become complex numbers. The modulus of  $\alpha$  is proportional to the size of the induced dipole moment while the phase factor of  $\alpha$  describes the delay of the induced dipole moment on the applied electric field. The polarizability  $\alpha$  of a mildly doped semiconducting sphere surrounded with a dielectric shell is calculated with the hydrodynamic model [4]. In this model the flow of the electrons is described by hydrodynamic equations which incorporate electrostatic interactions between the electrons in a self-consistent fashion and a diffusion term due to gradients in the free electron density. Applying a uniform electric field to a semiconducting sphere, the conduction electrons drift to the

surface where they screen the applied electric field. Diffusion due to the gradient in the electron density acts as a force opposite to the applied field and makes that the screening charge is spread out over a distance of the Debye screening length  $L$ . The electric field inside the semiconducting sphere vanishes on a distance of the order of the Debye screening length from the surface (see Fig. 3.2). This is in firm contrast with the well-known Mie model [5] where diffusion is not taken into account. In the Mie model the screening charge is singularly located at the surface and the electric field changes discontinuously at the surface of the semiconducting sphere. Fig. B.1 shows the frequency dependence of the polarizability  $\alpha'$  and

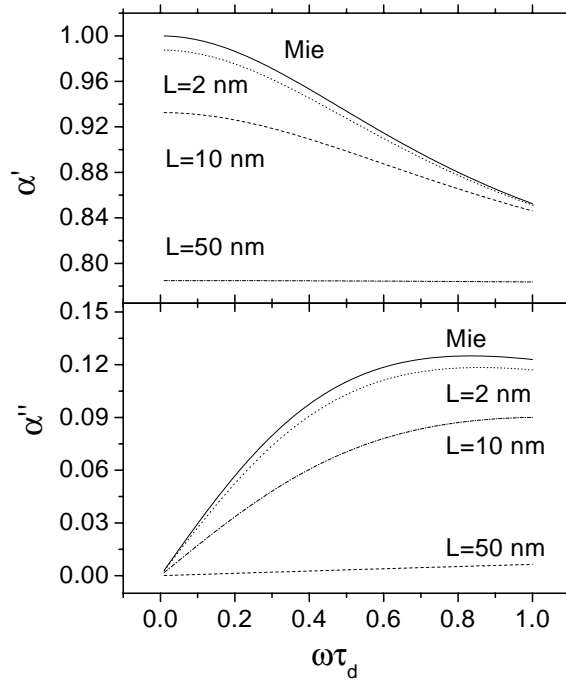


**Figure B.1:** The frequency dependence of the polarizability  $\alpha'$  and dielectric loss  $\alpha''$  of a semiconducting sphere calculated with the hydrodynamic model for several values of the Debye screening length  $L$ . The dielectric relaxation time  $\tau_d$  (see [4]) equals the time constant on which the screening occurs. The radius is 50 nm and the dielectric constant is 10. The solid line gives the prediction from Mie theory.

dielectric loss  $\alpha''$  of a semiconducting sphere calculated with the hydrodynamic model for several values of the Debye screening length  $L$ . For a Debye screening length  $L$  of the order of the radius  $R$ , the elaborate hydrodynamic model differs significantly from the Mie model.

At the end of this appendix we explicitly calculate the polarizability  $\alpha$  of a semiconducting sphere surrounded by a dielectric shell (see Eq. B.6). Parameters in the expression for this polarizability are the outer radius  $R$  and the dielectric constant  $\epsilon$  of the dielectric background in which the free electrons move. We estimate  $R$  to be 75 nm from SEM images (see Fig. 3.1) and from literature we take  $\epsilon$  to be 8.5 [6]. With an effective electron mass  $m_n = 0.35m_e$ , where  $m_e$  is the bare electron mass [6], and a free electron density  $n$  equal to the doping density ( $= 3 \times 10^{17} \text{cm}^{-3}$ ) the other parameters of  $\alpha$  become  $L = \sqrt{\epsilon\epsilon_0 kT/ne^2} = 6.4$  nm and the plasma frequency  $\Omega_p = \sqrt{ne^2/\epsilon\epsilon_0 m_n} = 1.8 \times 10^{13}$  Hz. The only parameters not determined yet by an independent measuring method are the radius of the semiconducting part in the dark  $R_c(\text{dark})$ , under illumination  $R_c(I)$  and the mobility of the free electrons inside the semiconducting core.

### Explicit calculation of the polarizability $\alpha$ of a weakly conducting sphere surrounded by a dielectric sphere

For wavelengths long compared to the size of a particle, the applied field  $\mathbf{E}$  can be considered uniform on the scale of the particle. We assume the electric field to be directed along the  $z$  axis. For this case the electrostatic potential outside of the sphere has the form (in spherical coordinates)

$$\Phi_o(r, \theta) = (-Er + \frac{1}{4\pi\epsilon_0} \frac{p}{r^2})P_1(\cos \theta), \quad (\text{B.2})$$

where the second term is the polarization field caused by the dipole moment  $p$  induced in the sphere. Note that the polarizability of the particle  $\alpha(\omega)$  is related to the dipole moment  $p(\omega)$  via

$$p(\omega) = 4\pi R^3 \epsilon_0 \alpha(\omega) E(\omega). \quad (\text{B.3})$$

Inside the conducting sphere the potential has the form

$$\Phi_c(r, \theta) = [aB(\frac{r}{\zeta}) + br]P_1(\cos \theta) \quad (\text{B.4})$$

where  $B$  is a spherical Bessel functions of the first kind and  $\zeta$  is the complex Helmholtz length (see [4]). Inside the depletion layer the potential obeys the

Laplace equation and has the form

$$\Phi_d = \left(\frac{c}{r^2} + dr\right)P_1(\cos \theta). \quad (\text{B.5})$$

The five unknowns  $a, b, c, d$  and  $p$  are determined from the boundary conditions at the conducting and depleted region interface and the depleted region and air interface.

At the conducting and depleted region interface we require

- (i)  $\Phi_c(R_c) = \Phi_d(R_c)$ ,
- (ii)  $\epsilon_c(\partial/\partial r)\Phi_c(R_c) = \epsilon_d(\partial/\partial r)\Phi_d(R_c)$  (continuity of the component of  $D$  perpendicular to the interface) and
- (iii)  $\partial/\partial r(\Phi_c - L^2 \triangle \Phi_d)|_{r=R_c} = 0$  (electron flow tangential to the interface), where  $\epsilon_c$  ( $\epsilon_d$ ) is the dielectric constant of the dielectric background in which the electrons move in the conducting (depleted) region. At the depleted region and air interface we require
- (iv)  $\Phi_d(R) = \Phi_o(R)$  and
- (v)  $\epsilon_d \partial/\partial r \Phi_d(R) = \partial/\partial r \Phi_o(R)$  (continuity of the component of  $D$  perpendicular to the interface).

By solving these five equations we obtain the expression for the polarizability

$$\alpha = 1 - \eta \chi R^3 - R_c^3 \chi. \quad (\text{B.6})$$

In this expression

$$\eta = \frac{R_c B'(1 - \delta) + 2 \frac{\epsilon_d}{\epsilon_c} (B\zeta - B'\delta R)}{\frac{\epsilon_d}{\epsilon_c} (B\zeta - B'\delta R) - R_c B'(1 - \delta)}, \quad (\text{B.7})$$

$$\delta = 1 - \frac{L^2}{\zeta^2} \quad (\text{B.8})$$

and

$$\chi = \frac{3}{2R_c^3(1 - \epsilon_d) + \eta R^3(\epsilon_d + 2)}. \quad (\text{B.9})$$

The validity of this expression is verified for two special cases:

- (i) For a semiconducting sphere without dielectric shell,

$$\lim_{R \rightarrow R_c} \alpha = \frac{[\epsilon_c - \delta(\epsilon_c - 1)] \frac{R}{\zeta} B' - B}{[\epsilon_c - \delta(\epsilon_c + 2)] \frac{R}{\zeta} B' + 2B} \quad (\text{B.10})$$

which is the expression derived in [4].

(ii) For a non-conducting sphere (with  $\epsilon_c = \epsilon_d$ ),

$$\lim_{L \rightarrow \infty} \alpha = \frac{\epsilon_c - 1}{\epsilon_c + 2} \quad (\text{B.11})$$

which is the well-known expression for the polarizability of a dielectric sphere.

## References

- [1] M. Sotoodeh, A. Khalid and A. Rezazadeh, J.Appl.Phys. **87**, 2890 (2000).
- [2] Y. Kao and O. Eknayan, J.Appl.Phys. **54**, 2468 (1983).
- [3] J. Jackson, *Classical Electrodynamics*, J. Wiley, 1998.
- [4] E. van Faassen, Phys. Rev. B **58**, 23 (1998).
- [5] M. Born and E. Wolf, *Principles of optics*, Pergamon Press, 1975.
- [6] S.J. Fonash, *Solar Cell Device Physics*, Academic Press, 1981.





## Appendix C: Polarisation energy of a spherical symmetric charge distribution

---

We calculate the polarization energy  $\Sigma_1(R)$  for a spherical symmetric charge distribution  $\rho(\mathbf{r}) = -e|\Psi(\mathbf{r})|^2$  in a sphere with radius  $R$ . We make the approximation that the microscopic static dielectric function  $\epsilon(\mathbf{r}, \mathbf{r}')$  equals the macroscopic static dielectric constant  $\epsilon_{in}(\epsilon_{out})$  inside (outside) the quantum dot. In terms of the electric field strength, the polarization energy is defined by [1]:

$$\Sigma_1 = \frac{\epsilon_0}{2} \int \epsilon(\mathbf{r}) E(\mathbf{r})^2 d\mathbf{r} \quad (\text{C.1})$$

where  $E$  equals the electric field strength due to the charge distribution  $\rho(\mathbf{r})$ . Outside the sphere the electric field strength equals

$$E_{out}(r) = \frac{e}{4\pi\epsilon_0\epsilon_{out}r^2}. \quad (\text{C.2})$$

The contribution to the polarization energy  $\Sigma_1 (= \Sigma_{1,in} + \Sigma_{1,out})$  from outside the sphere is given by

$$\Sigma_{1,out} = \int_R^\infty \epsilon_0\epsilon_{out} E_{out}^2(r) 4\pi r^2 dr = \frac{e^2}{4\pi\epsilon_0\epsilon_{out}R}. \quad (\text{C.3})$$

Inside the sphere, the electric field is given by

$$E_{in}(r) = \frac{c(r)}{4\pi\epsilon_0\epsilon_{in}r^2}, \quad (\text{C.4})$$

where  $c(r)$  represents the charge enclosed by a sphere with radius  $r$ . The contribution from inside the sphere is given by

$$\Sigma_{1,in} = \int_0^R \epsilon_0\epsilon_{in} E_{in}^2(r) 4\pi r^2 dr. \quad (\text{C.5})$$

Within the effective mass model with an infinite potential barrier at the surface, the normalized wavefunction for an electron in the S-level equals  $\psi(\mathbf{r}) = \frac{1}{\sqrt{2\pi R}} \sin(\frac{\pi}{R}r)$ , and we obtain

$$c(r) = \frac{2e}{R} \left( \frac{1}{2}r - \frac{R}{4\pi} \sin\left(\frac{2\pi}{R}r\right) \right). \quad (\text{C.6})$$

From a numerical computation of Eq. C.5 we obtain that

$$\Sigma_{in} = \frac{e^2 1.01}{4\pi\epsilon_0\epsilon_{in}R}. \quad (\text{C.7})$$

The (first order perturbation) polarisation energy for an S-electron with respect to the polarisation energy in a bulk crystal becomes

$$\Sigma_1 = \frac{e^2}{4\pi\epsilon_0R} \left( \frac{1.01}{\epsilon_{in}} + \frac{1}{\epsilon_{out}} \right). \quad (\text{C.8})$$

For comparison, the polarisation energy of a uniform charge distribution inside the sphere ( $c(r) = e\frac{r^3}{R^3}$ ) equals

$$\Sigma_1 = \frac{e^2}{4\pi\epsilon_0R} \left( \frac{0.2}{\epsilon_{in}} + \frac{1}{\epsilon_{out}} \right). \quad (\text{C.9})$$

## Reference

- [1] J. Jackson, *Classical Electrodynamics*, J. Wiley, 1998.

## Samenvatting

---

Halfgeleider nanostructuren vertonen elektrische en optische eigenschappen die erg verschillen van bulk halfgeleiders. Het bestuderen van deze verschillen is niet enkel interessant vanuit wetenschappelijk oogpunt, het is ook van belang voor toepassingen in de optische en elektronische industrie. We denken hier bijvoorbeeld aan halfgeleider componenten zoals transistoren die steeds kleiner worden, onder andere om ze sneller en efficiënter te maken.

De eigenschappen van halfgeleider nanostructuren zullen erg verschillen van de bulk eigenschappen zodra een afmeting van zo een structuur van de orde van grootte wordt van de lengteschaal van een fysische grootte (bijvoorbeeld de golflengte van licht of van een elektron of een elektrostatische afschermingslengte). Zo zal bijvoorbeeld zichtbaar licht sterk verstrooid worden in een poreuze halfgeleider met structuurafmetingen van enkele honderden nanometers. Dit verschijnsel is analoog aan de sterke verstrooiing van een elektron in een kristal indien de golflengte van het elektron gelijk wordt aan de roosterafstand van het kristal, wat aanleiding geeft tot energiebanden en verboden energiezones.

De elektrische eigenschappen van zo een poreuze halfgeleider zijn ook erg verschillend van de bulk eigenschappen. Vooreerst heb je de oppervlakte-toestanden aan het enorme inwendige oppervlak met een energie in de verboden zone, die geleidingselektronen en valentiegaten kunnen vangen. Op deze manier kan een laag aan de rand van een halfgeleider ontstaan worden van geleidingselektronen (depletielaag) met een sterk elektrisch veld tot gevolg. Daarnaast zal er, indien de diffusielengte van minderheidsladingdragers van de orde van de structuurafmetingen wordt, efficiënte scheiding van elektronen en gaten optreden. Dit is van belang in een toepassing zoals een zonnecel waar scheiding van fotoelektron-gat paren een externe stroom veroorzaakt.

Ook de transporteigenschappen van elektronen in zo een poreuze halfgeleider zijn erg verschillend van transport in de bulk. De mobiliteit van elektronen in poreus GalliumFosfide (GaP) over afstanden groot ten opzichte van de poreuze structuren zijn tot vijf ordes van grootte kleiner dan in bulk GaP. Deze enorme afname van de mobiliteit wordt toegeschreven aan het vangen van elektronen in oppervlaktetoestanden. In het eerste deel van dit proefschrift bestuderen we de mobiliteit van elektronen in poreus GaP over afstanden die *klein* zijn in verhouding tot de afmetingen van de poreuze structuur. Deze mobiliteit bekomen we aan de hand van reflectiemetingen aan een microgolf caviteit gevuld met poreus GaP.

In hoofdstuk 1 van dit proefschrift overlopen we de fysische concepten van energieniveaus in bulk halfgeleiders en halfgeleider nanostructuren. In hoofdstuk 2 bespreken we een experimentele methode voor het kontaktloos meten van de diëlektrische konstante bij frequenties van  $10^{10}$  Hz van een zwak geleidend monster. De diëlektrische konstante wordt bepaald aan de hand van het reflectiespektrum van een microgolf caviteit gevuld met het monster. Deze methode blijkt erg geschikt voor het meten van kleine veranderingen in de complexe diëlektrische konstante ( $\geq 10^{-6}$ ) en dit met een tijdsresolutie van 10 nanoseconden.

In hoofdstuk 3 wordt bovenstaande methode gebruikt om de diëlektrische konstante van poreus GaP te meten en de verandering ervan onder konstante belichting en onder belichting met een laser puls. De resultaten kunnen kwantitatief begrepen worden door het poreuze materiaal te beschrijven als een verzameling geleidende bollen omgeven door een depletielaag. De polariseerbaarheid van zo een geleidende bol omgeven door een depletielaag met een totale straal van ongeveer 75 nm, berekenen we met een hydrodynamisch model. In dit model wordt de elektrostatistische interactie tussen de elektronen op een zelf-consistente manier beschreven. Dit model beschrijft dat indien een uniform elektrisch veld wordt aangelegd over een geleidende bol, de geleidingselektronen zich naar de rand van de bol verplaatsen waar ze het aangelegde elektrische veld afschermen. Diffusie tengevolge van de gradiënt in de elektrondichtheid werkt als een kracht tegengesteld aan die van het elektrische veld en zorgt ervoor dat de afschermingslading zich verspreidt over een afstand van de orde van de Debye afschermingslengte. In ons geval is deze afschermingslengte van de orde van 10 nm. Dit staat in scherp contrast met het veel gebruikte Mie model waar geen diffusie in rekening wordt gebracht en de afschermingslading zich dus enkel op de rand van de geleidende bol bevindt.

De verandering in de diëlektrische konstante onder belichting kan met dit model beschreven worden als een verandering in de grootte van de depletielaag. Op deze manier bekomen we dat zonder belichting het geleidende deel van de bol een straal heeft van  $43 \pm 5$  nm en dat de mobiliteit van de elektronen in deze bol  $3 \pm 1$  cm<sup>2</sup>/Vs bedraagt. Deze waarde is ongeveer 40 maal kleiner dan de elektrondichtheid in bulk GaP. Een mogelijke verklaring voor dit verschil is dat de elektrondichtheid aan de rand van de geleidende bol onnauwkeurig is beschreven. Door afscherming van het aangelegde elektrische veld wordt de polariseerbaarheid immers voornamelijk bepaald door de eigenschappen van de halfgeleider tot een afstand van de Debye lengte van de rand. In ons model wordt de elektrondichtheid gelijk aan de doteringsdichtheid verondersteld in het geleidende gedeelte en gelijk aan nul in het gedepleteerde gedeelte. Een meer nauwkeurige beschrijving van de elektrondichtheid aan de rand van de geleidende bol kan de mobiliteit beïnvloeden

die uit de polarizeerbaarheid wordt bepaald. De mobiliteit die we hier bekomen is tot vijf ordes van grootte groter dan de mobiliteit in poreus GaP bepaald uit transportmetingen over afstanden groter dan de poreuze structuren. De verklaring voor dit enorme verschil ligt in het feit dat in het transport over lange afstanden elektronen veelvuldig gevangen worden in gelokaliseerde elektrontoestanden met een energie beneden de rand van de geleidingsband.

Het krimpen van de depletielaag onder belichting en het opnieuw uitzetten ervan na belichting kan kwantitatief begrepen worden met een model dat elektron-gat recombinatie veronderstelt in de bulk en aan het oppervlak. Het vangen van gaten in oppervlaktetoestanden gebeurt op een tijdsschaal sneller dan onze meetmethode ( $10^{-8}$  s) en is verantwoordelijk voor de reductie van de depletielaag. Recombinatie van elektronen in oppervlaktetoestanden, wat de depletielaag vergroot, gebeurt echter via het overkomen van de depletiebarriere. Dit verklaart waarom elektron-gat paren na belichting alsmat langzamer recombineren en waarom deze recombinatie zich uitstrekt in tijd over meer dan vijf ordes van grootte.

In het laatste hoofdstuk van dit proefschrift bestuderen we ZnO kristallen met een afmeting tussen drie en zes nanometer. Aangezien deze kristallen veel kleiner zijn dan de golflengte van geleidingselektronen in bulk kristallen, leidt opsluiting in deze kristallen tot staande golven met discrete golfvectoren. De afstand tussen de discrete energieniveaus is in onze kristallen van de orde van 100 meV en daarmee groter dan de thermische energie bij kamertemperatuur ( $kT \sim 25$  meV). Dergelijke kristallen worden ook wel quantum dots genoemd. Naast de kinetische energie zal ook de polarizatie-energie, en de exchange en Coulomb interactie tussen elektronen, sterk afhangen van de grootte van de quantum dot. Opsluiting dwingt de golfkunties immers elkaar te overlappen.

In hoofdstuk 4 bestuderen we optische overgangen tussen de discrete geleidingsniveaus in ZnO quantum dots met behulp van infrarood (IR) absorptiometingen. Het meest eenvoudige model voor een geleidingselektron in een quantum dot is het model van een vrij elektron in een potentiaalput met oneindig hoge wanden. Merk op dat dan geen interactie met het kristalrooster of oppervlakte atomen beschreven wordt. Voor elektronen met een energie net boven het minimum van de geleidingsband kan de interactie met het kristal benaderd worden door het elektron een effectieve massa toe te kennen (effectieve massa model). Voor een sferisch symmetrisch systeem kunnen de energie-eigentoestanden aangeduid worden met hun baanimpulsmoment kwantumgetal  $l$ . De laagste geleidingsenergieniveaus in het effectieve massa model kunnen in volgorde van toenemende energie aangeduid worden met S ( $n = 1, l = 0$ ), P ( $n = 1, l = 1$ ), D ( $n = 1, l = 2$ ), S' ( $n = 2, l = 0$ ) en F ( $n = 1, l = 3$ ) waarbij het kwantumgetal  $n$  energieniveaus met gelijke baanimpulsmoment kwantumgetallen  $l$  onderscheidt. Indien de twee

mogelijke spin-toestanden van een elektron worden inbegrepen bevat ieder energieniveau  $2(2l + 1)$  elektrontoestanden. Naast dit eenvoudige effectieve massa model gebruiken we in dit hoofdstuk een geavanceerd 'tight-binding' model. In dit model wordt de eigenwaarde-vergelijking van de één-deeltjes Hamiltoniaan van een elektron in een quantum dot (die interactie met rooster en oppervlakte-atomen en spin-baan koppeling bevat) numeriek opgelost, waarbij de eigenfuncties van het elektron opgebouwd worden uit een beperkt aantal atomaire golffuncties. Hoewel beide modellen analoge energieniveaus hebben verschilt voor de kleinste dots het effectieve massa model sterk van het nauwkeurige 'tight-binding' model. De voornaamste reden hiervoor is dat we in het effectieve massa model geen eindige potentiaalsprong aan de rand van de dot verondersteld hebben waardoor tunnelen van het elektron buiten de quantum dot uitgesloten wordt.

De ligging van de elektronniveaus is spectroscopisch te onderzoeken indien het aantal geleidingselektronen in de quantum dot bekend is. Voor het bezetten van de quantum dots met elektronen hebben we twee methodes gebruikt. In de eerste methode wordt een laag ZnO quantum dots gedeponeerd op de werkelektrode van een elektrochemische cel. Mobiliteitsmetingen aan deze lagen hebben aangetoond dat elektronen tunnelen tussen de energieniveaus van elkaar rakende quantum dots. Dit transport van elektronen tussen de dots zorgt ervoor dat de elektronen in de laag een evenwichtsbezetting innemen die volledig bepaald wordt door de elektrochemische potentiaal van de werkelektrode. De totale lading opgeslagen in de laag wordt bepaald door het integreren van de opladingsstroom. In combinatie met het aantal quantum dots in de laag, bepaald met een chemische analyse methode, bekomen we het gemiddeld aantal geleidingselektronen per quantum dot. Op deze manier kunnen tot tien elektronen opgeslagen worden in een quantum dot. In de tweede methode wordt een suspensie van ZnO quantum dots in ethanol gebruikt. Het opladen van de quantum dots met geleidingselektronen gebeurt hier door het maken van elektron-gat paren door belichting met ultraviolet licht. Door het wegvangen van het gat door het oplosmiddel (ethanol) bekomen we een geladen quantum dot met een levensduur van enkele minuten. Aangezien de afstand tussen de dots in oplossing tien maal de grootte van de dots bedraagt verwachten we dat de koppeling tussen de dots hier zwak is. IR absorptie spectra bekomen met beide methodes zijn erg gelijkend. Dit wijst er op dat koppeling tussen de dots ook in de eerste methode geen grote invloed heeft op de elektrontoestanden in een dot.

Door het aantal elektronen per dot stapsgewijs te vergroten kan de IR absorptie toegekend worden aan verschillende overgangen tussen de energieniveaus. Echter, door de spreiding in de deeltjesgrootte en de sterke afhankelijkheid van de energieniveaus van de grootte van de dots, wordt de spectrale breedte van een

overgang tussen twee energieniveaus sterk vergroot. Om de absorptie van de laag quantum dots toe te kennen aan overgangen tussen discrete energieniveaus is het daarom noodzakelijk om de elektronbezetting van een dot als functie van zijn grootte te kennen. Met een model dat de absorptie berekent van een verzameling dots met een elektron evenwichtsbezetting kunnen we de absorptie spectra kwantitatief beschrijven voor een gemiddelde elektron bezetting tot tien elektronen. De interpretatie van de absorptie spectra met dit model toont aan dat enkel overgangen toegestaan door rotatiesymmetrie optreden. Met andere woorden we meten enkel overgangen met  $\Delta l = \pm 1$ . Dit betekent dat de interactie met het kristalrooster en/of oppervlakteatomen, die geen volmaakte rotatiesymmetrie bezit, de optische overgangswaarschijnlijkheden niet ernstig stoort. De overgangswaarschijnlijkheden voor S-P, P-D, D-F en P-S' zijn in overeenstemming met de waarden berekend met het 'tight-binding' model en het effectieve massa model. Ook de afstanden tussen de S, P, D, en F energieniveaus en hun afhankelijkheid van de grootte van de dots zijn in overeenstemming met de waarden berekend met het 'tight-binding' model en het effectieve massa model. We besluiten dat IR absorptiemetingen met controle over het aantal elektronen per dot een krachtige methode is voor het bestuderen van de elektrontoestanden in quantum dots.





## List of publications

---

A. Germeau, E. van Faassen, and D. Vanmaekelbergh,  
*Contactless measurements of short-range electron motion in semiconducting macro-porous GaP*,  
Phys. Rev. B **65**, 165331 (2002).

A. Germeau, A. Roest, G. Allan, C. Delerue, E. Meulenkaamp and D. Vanmaekelbergh,  
*Optical transitions in few-electron artificial atoms strongly confined in ZnO nanocrystals*.  
Submitted to Phys. Rev. Lett.

A. Roest, A. Germeau, J. Kelly, D. Vanmaekelbergh, G. Allan and E. Meulenkaamp  
*Long-range electron transport in an assembly of ZnO quantum dots: the effects of quantum confinement, Coulomb repulsion and structural disorder*.  
Submitted to Chem. Phys. Chem.



## Dankwoord

---

Vier jaren van onderzoek zijn voorbij. In dit onderzoek is me veel vrijheid geboden. Deze zelfstandigheid was niet altijd makkelijk maar wel erg leerrijk. Dit is een ogenblik om mensen te bedanken die me deze vier jaren hebben gesteund. Op de eerste plaats wil ik hier mijn promotor Daniel Vanmaekelbergh en begeleider Ernst van Faassen bedanken. Het enthousiasme van Daniel en zijn pragmatisme om resultaten te formuleren waren een grote steun voor mij. De interesse van Ernst en zijn grondig inzicht in natuurkunde zijn voor mij steeds een lichtend voorbeeld geweest. Mijn promotor Werner van der Weg wil ik bedanken voor zijn steun op een ogenblik dat het onderzoek dreigde vast te lopen. John Kelly dank ik voor de zorg bij het tot stand komen van dit proefschrift.

Aarnoud Roest heeft me geleerd eigenhandig quantum dots te maken. Het was aangenaam en produktief om samen met hem gecombineerde infrarood absorptie- en capaciteitsmetingen aan quantum dots te doen. Met Zeger Hens heb ik vaak fysische problemen kunnen doorspreken. Je tiens à remercier Christophe Delerue et Guy Allan pour leurs calculs précis des états d'un électron dans une boîte quantique. En plus, ils étaient si gentils à répondre toutes mes questions sur leur modèle de liaisons fortes. I would like to thank Stephen Hickey and Celso de Mello-Donaga for making CdSe quantum dots. It is a pity I could neither measure their permanent nor their induced electric dipole moment. Andries Meijerink en Paul Peijzel waren steeds zo vriendelijk om mij hun apparaten te laten gebruiken. Zo heb ik hun IR detector en lock-in amplifier mogen gebruiken om tevergeefs naar IR emissie van quantum dots te speuren. Hun Excimer laser heb ik gebruikt om de elektrische polariseerbaarheid van quantum dots te bepalen. Later bleek deze polariseerbaarheid jammer genoeg niet te onderscheiden van artefacten. Via Tom Visser heb ik infrarood absorptiemetingen kunnen uitvoeren in de groep anorganische chemie.

Bij de technici wil ik in de eerste plaats Stephan Zevenhuizen bedanken voor het automatiseren van microgolfmetingen en radiofrequentie impedantie- en reflectiemetingen. Mari Hanegraaf dank ik voor het maken van heel wat technische constructies zoals een geschikte condensator en een afscherming voor de YaG laser. Glasblazer Wim wist steeds weer kleinere capillairtjes te maken tot hij ze nog nauwelijks kon zien of vasthouden. Ruurd Lof had vaak een originele insteek van fysische problemen en Carine van der Werf heeft een aantal halfgeleiderlaagjes gedeponeerd.

Ook wil ik iedereen van de groep Grenslaagfysica bedanken waar ik de twee eerste jaren van mijn promotie heb doorgebracht. Ik deelde er de kamer met Geoffrey Munyeme die net als ik het leven in Nederland leerde kennen. Het was er goed ontspannen met jongens als Jeroen, Harald, Riny, Aad, Bernd, Jochen, Raul, ... te veel om allemaal op te noemen. De laatste twee jaren heb ik aangenaam doorgebracht in de groep Gecondenseerde Materie. Tussen mijn kamergenoot François Reincke en mij klikte het dadelijk en met geregeld wat humor zorgden we voor een zorgeloze sfeer in onze kamer. Voor een vlotte babbel kon ik steeds terecht bij mensen als Zeger, Hans, Arnoud, Otto, Gijs, Harry, ... .

Naast het werk heb ik de voorbije vier jaren heel wat spannende weekends en vakanties beleefd met de Amsterdamse zweefvliegclub. Verder heb ik mooie herinneringen aan tochten in de Alpen met Steven, rotsklimweekends en vakanties met Pieter en Iwanka en fietsvakanties met de 'helden van de fredmobiel'. Dichter bij huis heb ik mijn passie voor klimmen beleefd met Rob, Chris en Irene. Het zwemmen kreeg een extra dimensie door Huib, René en Patricia. Aan het slot van dit dankwoord denk ik aan Jan-Pieter, mijn familie en Marieke.

## Curriculum vitae

---

Alexander Germeau werd op 21 september 1973 geboren te Leuven (België). In 1991 beëindigde hij het middelbaar onderwijs in de studierichting Latijn-wiskunde aan het Sint-Jorisinstituut te Brussel. Daarna begon hij aan de studie natuurkunde aan de universiteit te Leuven. In 1996 behaalde hij er zijn doctoraalexamen in de theoretische natuurkunde met een afstudeeronderzoek over operatorentheorie en kwantum statistische mechanica. In het daaropvolgende jaar heeft hij een post-graduaat bekomen in de hoge-energiefysica aan de universiteit te Mons. Het onderzoek dat hij hiertoe heeft gedaan heeft geleid tot kinetische parameters voor de detectie van elementaire deeltjes bij botsingen van atoomkernen uitgevoerd aan het CERN te Genève. In het jaar 1998 heeft de auteur als software engineer gewerkt bij het bedrijf Siemens A.G. te Mons. Daar heeft hij programmatuur ontwikkeld voor het upgraden van telefoonnetwerken. Vanaf januari 1999 was hij aangesteld als assistent in opleiding aan de Universiteit Utrecht. Daar heeft hij gedurende vier jaar onderzoek gedaan aan halfgeleider nanostructuren binnen de vakgroepen Grenslaagfysica en Gecondenseerde Materie. De resultaten van dit onderzoek staan beschreven in dit proefschrift. Tijdens deze periode heeft hij werkcollege elektromagnetisme gegeven aan derdejaars natuurkundestudenten.

